

GRAPHENE AS ATOMIC PAPER:
FROM BENDING STIFFNESS TO MECHANICAL METAMATERIALS

A Dissertation

Presented to the Faculty of the Graduate School

of Cornell University

In Partial Fulfillment of the Requirements for the Degree of

Doctor of Philosophy

by

Melina K. Bles

January 2015

© 2015 Melina K. Bles

GRAPHENE AS ATOMIC PAPER:
FROM BENDING STIFFNESS TO MECHANICAL METAMATERIALS

Melina K. Blee, Ph.D.

Cornell University 2015

In the last few years, scientists and engineers have begun to borrow design principles from the paper arts of origami and kirigami (ori=fold, kiru=cut). This multidisciplinary approach is already proving its potential in everything from medicine to satellite engineering. Graphene, an extraordinarily strong atom-thick sheet, is the ideal starting material for bringing these design ideas down to the nanoscale. We have developed a technique to lift graphene and manipulate it like a sheet of paper in aqueous solution. This allows us to measure the out-of-plane bending stiffness of graphene, a fundamental mechanical property that has never been conclusively measured at the micron scale. We see a stiffness orders of magnitude higher than the atomic-scale value, and show that this surprising result can be explained by theories of thermally induced fluctuations. We then apply designs from the paper art of kirigami to create three-dimensional structures and moving parts. We demonstrate robust stretchable electrodes and extraordinarily resilient hinges, and show that we can control graphene devices directly with micromanipulators or remotely with magnetic fields and lasers. Graphene kirigami's extraordinary mechanical and electrical properties make it promising for a variety of applications, from force sensors to biocompatible electrical readouts. This simple but powerful approach to creating graphene metamaterials promises diverse, resilient moving parts at the nanoscale.

BIOGRAPHICAL SKETCH

Melina Katherine Blees was born in California in 1984, and spent her early years on the Pacific north coast, in the French West Indies, and in the south of France. She was homeschooled until moving to Davis, California, where she graduated from high school in 2002. Melina then attended Carleton College in Northfield, Minnesota, where she took full advantage of the vibrant liberal arts environment to study everything from metalworking to Byzantine history. She learned a great deal of physics from her friends at late-night study sessions, and found that she loved experimental work during REU programs at the University of Minnesota and UC Davis.

Melina graduated from Carleton with honors in 2007, and headed to Cornell along with quite a few of her classmates and friends. There she joined Paul McEuen's group, where she began by learning to grow aligned carbon nanotubes, then studied the electrical contact between graphene and carbon nanotubes. One afternoon Paul—back from the anniversary celebration of Richard Feynman's famous talk on the future of nanoscience—said, "What I *really* want are tiny machines," and launched them into the new world of graphene kirigami.

In her time at Cornell, Melina was a fellow at the Cornell Nanoscale Science and Technology Facility (CNF), where she learned nanoimprint technology and developed the CNF's user wiki. She also continued her lifelong arts education, taking courses in (macroscale) lithography, woodblock printing, letterpress printing, painting, art history, and sculpture. After graduating, Melina will brave a few more winters to pursue her lifelong interests in art and science. She is heading to a postdoc with a new program at U. Chicago's Institute for Molecular Engineering that aims to blend art, science, and theater.

To my family

ACKNOWLEDGMENTS

The single greatest factor that has shaped my life has been my extraordinary good luck in people. I've received incredible support throughout this process from my friends, colleagues, teachers, and family, and they have my heartfelt thanks for making my time in Ithaca so educational and enjoyable.

Working for Paul McEuen has been the greatest intellectual honor. I've never met anyone with such a clear mind and such an instinct for the right questions. Paul has a fierce commitment to truth and clarity and will poke at a fuzzy sentence until it's 100% correct, but he's also endlessly generous and kind and has the rare ability to make constructive criticism feel *constructive*. I've learned an enormous amount from him about physics, as well as about creativity, storytelling, problem solving, public speaking, collaboration, and the joys of a good scientific mystery. It has been a rare privilege to go through graduate school with an advisor who always had my back, especially when I jumped into a weird little artsy project with no funding or guarantee of success. In a million different ways, this thesis could never have happened without him. He's given me a framework to continue working from for the rest of my life—to push harder, write a clearer sentence, tell a better story, and face down a frightening truth without blinking. I could never have asked for a better mentor.

I also owe a huge debt of gratitude to my colleagues in the McEuen group, who have been my support network, my teachers, and my friends over the years. It has been a pleasure to learn from them and alongside them. Arthur Barnard, who with extraordinary kindness, patience, and generosity always pushed me to do my best; Samantha Roberts, who has been a support and an inspiration; Arend van der Zande, who generously mentored me when I first joined, and who went rapidly from being that guy with the wasp story to a dear friend; Peter Rose, who I suckered into this

business and who instantly rose to the challenge with a big smile; Kathryn McGill and Jonathan Alden, who continually challenged me to be a better scientist and a more self-aware human being; Alex Ruyack, whose enthusiasm and fierce curiosity were a joy to work alongside for all those years; Isaac Storch and Alejandro Cortese, whose good cheer I will miss; and Xiaidong Xu, Nathan Gabor, Zhaohui Zhong, Shogo Hamada, Josh Kevek, Kin Fai Mak, Matt Graham, Luke Donev, all of the excellent undergraduates, and many more wonderful and brilliant folks who I've been lucky enough to work with, however briefly.

Pinshane Huang was not technically in the McEuen group, but she taught me a huge amount about how to navigate science, how to work effectively with others, and how to move through the world with poise. She also cleaned the floors more often than she should have had to, learned to communicate using the strange noises that I make before I've had tea in the morning, and was always an outstanding friend, roommate, and a true and ongoing inspiration. I don't know if I could have accomplished this without her, but it certainly wouldn't have been as much fun.

Thank you to my always-supportive committee, Professors Dan Ralph and Erich Mueller, whose enthusiasm and kindness made me feel like I had an extensive support structure to draw on. Thank you, too, to the staff of the CNF for their ongoing support and good cheer, particularly Noah Clay, Garry Bordonaro, and Mike Skvarla. I appreciate the friendship and assistance of the physics department/LASSP/CCMR staff, particularly Caroline Brockner, Brenda Irvin-Bryant, and Kacey Bray Acquilano. I want to thank the art department, too, who made me feel both welcome and continually challenged: Gregory Page, Michael Ashkin, Stephanie Owens, and Jim Tyler.

My friends have made my life both outside and inside the lab a wonderful one. This category includes a lot of the people who have already been named, but also

many more. My band, Kassie and Ross Martin-Wells, who my fortuitous choice of graduate schools turned into extra bonus family, and who were always there to explain me to myself when I most needed it. Ellie Hill, *doctor*. Craig Hogle and John McDonough: whole areas of physics knowledge are permanently recorded to my brain in their voices, so they were both basically here in spirit for the whole PhD. Cresten Mansfeldt, whose creativity and endless kindness made my time here so much richer. Eliot Kapit and Eliza Buhner, some of my first friends in Ithaca and still some of my closest. Susan Wiser, a source of limitless charm and warmth and dogs. Karen Zimmer and Cliff Martin, who welcomed me into their family with open arms. Chinmayee Subban, who I'm so glad I gave my number to. And Joni Longenecker, Ryan Henderson, Dave Tsang, Patrick Bennett, Marie Krysak, the posse, Cheyenne Munson, and all of my friends from the physics and chemistry departments who made Ithaca a home away from home or stayed in touch across the distance.

Ultimately, though, the very best people to impact my life are people I didn't get to choose at all. My amazing brother, Shanti, has a faith in me that I try to live up to every day. And I could write an endless list of the ways in which my parents guided and supported me in science—from demonstrating their own endless curiosity, to encouraging a five-year-old girl to putter around in the garage with her father so she wouldn't be afraid of power tools, to pouring endlessly over college guidebooks to find liberal arts schools with the best science programs—but all that would still pale in comparison to the fact that they taught me to be curious, to be honest, and to be kind. This thesis is dedicated to the three of them with all my love and gratitude.

TABLE OF CONTENTS

Chapter 1: Graphene as the ultimate atomic paper	
1.1 Introduction	1
1.2 Origami & kirigami in art and science	3
1.3 Key properties of graphene as an atomic paper	6
1.4 A short history of manipulating graphene	12
1.5 Outline of this thesis	15
Chapter 2: Fabrication and characterization of graphene kirigami devices	
2.1 Introduction	18
2.2 Growing graphene by chemical vapor deposition	18
2.3 Characterizing graphene grown by CVD	23
2.4 Device fabrication, graphene transfer, and the release process	27
2.5 Determining the amount of residue on completed devices	32
2.6 Controlling the adhesion to the substrate	36
2.7 Conclusions	37
Chapter 3: Directly manipulating graphene on and off of a surface	
3.1 Introduction	38
3.2 Experimental apparatus	38
3.3 Pushing on large sheets of graphene	41
3.4 Crumpling graphene with a laser	44
3.5 Moving and picking up graphene cantilevers	46
3.6 Spirals from graphene	48
3.7 Hinges from graphene	52
3.8 Conclusions	55
Chapter 4: The mechanics of two-dimensional crystalline membranes	
4.1 Introduction	56
4.2 Liquid and crystalline membranes	56
4.3 Formal theory of thermal fluctuations in crystalline membranes	60
4.4 Deviations from the harmonic model: the crossover length	62
4.5 An intuitive understanding of the stiffening effects	65
4.6 Applications to graphene	68
4.7 Conclusions	70
Chapter 5: Measuring the bending stiffness of graphene	
5.1 Introduction	71
5.2 Using gravity to measure spring constants	72
5.3 Analysis of the gravity data	74
5.4 Using thermal fluctuations to measure spring constants	77

5.5	Analysis of the thermal data	79
5.6	From spring constants to bending stiffness	84
5.7	An experimental value for the bending stiffness of graphene	85
5.8	The effect of surfactants and residues on the bending stiffness	87
5.9	Conclusions	87
Chapter 6: Kirigami patterns for stretchable graphene		
6.1	Introduction	90
6.2	Stretching in-plane graphene kirigami springs	92
6.3	How the springs stretch / 3D reconstructions	96
6.4	Tuning the spring constant by changing the cut pattern	100
6.5	Laser actuation and a force-distance curve	104
6.6	Electrical properties of graphene kirigami springs	106
6.7	Conclusions	111
Chapter 7: Applications of graphene kirigami and future directions		
7.1	Introduction	112
7.2	Studying adhesion and electrostatics with graphene kirigami	114
7.3	Cantilevers and kirigami in vacuum	116
7.4	Magnetic tweezer control of graphene devices	118
7.5	Superparamagnetic control of graphene devices	121
7.6	Applications of graphene kirigami to optics	124
7.7	Bimorphs and graphene origami	126
7.8	Conclusions	128
Chapter 8: Addendum		129
References		134

LIST OF FIGURES

1.1	The miniaturization of machines	2
1.2	Biology is a master of nanoscale moving parts	4
1.3	Building three-dimensional shapes from paper	5
1.4	Origami and kirigami in science at all size scales	7
1.5	Properties of graphene	9
1.6	Working with graphene	13
1.7	Crumpled and folded graphene	14
2.1	CVD growth of graphene	20
2.2	SEMs of CVD graphene	22
2.3	The Raman spectrum of graphene	24
2.4	TEM of CVD graphene	26
2.5	Fabrication and transfer process	29
2.6	Finished devices	33
2.7	Determining the residue on characterization chips	35
3.1	Experimental setup	39
3.2	Pushing a probe tip against a large sheet of unreleased graphene	42
3.3	Manipulating a large sheet of graphene after the sacrificial layer etch	43
3.4	Crumpling a large sheet of graphene with a laser	45
3.5	Manipulating devices by using the gold pads as handles	47
3.6	A graphene spiral	49
3.7	Extended graphene spirals	51
3.8	A monolayer graphene hinge actuated with a long graphene arm	53
3.9	Stills of the graphene hinge	54
4.1	Flat graphene at $T=0$ and fluctuations at $T>0$	57
4.2	Plot of the harmonic approximation vs. thermal fluctuation theory	64
4.3	Effective thickening of a membrane	66
4.4	Types of Gaussian curvature	67
5.1	Picking up a 50- μm -long device for gravitational measurements	73
5.2	Tracking the thermal motion	78
5.3	Analyzing the thermal fluctuations	81
5.4	Plot of spring constant versus length for thermal and gravity data	86
5.5	The effect of surfactants	88
6.1	Paper kirigami models	91
6.2	Patterns used for both the paper and graphene kirigami springs	93
6.3	Peeling a single-lobed graphene kirigami spring off of the surface	94
6.4	Stretching a double-lobed graphene kirigami spring	95
6.5	How the springs stretch	97
6.6	3-D reconstruction of the kirigami spring	99
6.7	Modeling the out-of-plane (pyramidal) spring	101
6.8	Actuating pyramidal springs with a laser	105
6.9	Cartoons of electrolyte gating	108
6.10	Graph of gate voltage versus conductance when stretched and unstretched	110

7.1	Other two-dimensional materials that might be used for kirigami	113
7.2	Electrostatic and adhesion experiments	115
7.3	Patterning suspended graphene in vacuum using a focused ion beam	117
7.4	Magnetic control of graphene devices	119
7.5	Magnetic orientations and starting patterns for building spheres	120
7.6	Actuating graphene with superparamagnetic pads	123
7.7	Optics applications	125
7.8	Bimorphs and graphene origami	127
8.1	Histogram of all data, including additional measurements	130
8.2	Interference microscopy image showing static structure	132

LIST OF TABLES

1.1	Relevant mechanical properties of graphene	11
5.1	Gravitational data for a sample device	75

There is no substitute for feeling the stone, the metal, the plaster, or the wood in the hand; to feel its weight; to feel its texture; to struggle with it in the world rather than in the mind alone.

—William M. Dupree

CHAPTER 1

GRAPHENE AS THE ULTIMATE ATOMIC PAPER

1.1 Introduction

Over fifty years ago, Richard Feynman gave a talk titled *There's Plenty of Room at the Bottom* that became a landmark in the history of nanotechnology. In his talk, Feynman challenged the scientific community to achieve the miniaturization of information, of electronics, and of machines.^{1,2}

In the years since, the miniaturizations of electronics and information have changed the world, and there has also been significant progress towards the miniaturization of machines (Fig. 1.1). Researchers have drawn on the tools of the semiconductor industry to build microscale cantilevers,³ gears and ratchets,⁴ hinges,⁵ actuators,⁶ grippers,⁷ and swimmers,⁸ and have developed novel ways of actuating micron-scale structures.^{9,10} However, there are still significant challenges to overcome, particularly as we start to scale down to smaller devices. Moving parts can be difficult to actuate, and in many cases they can only be used once. Material limitations become critical as we scale down, and mechanical properties change dramatically at the nanoscale.

As we struggle with these fabrication and actuation challenges, we can look to nature for inspiration. Biology is a master of nanomachines (Fig. 1.2). From hinges¹¹ to molecular walkers,¹² it provides a model for the kinds of resilience, versatility, and autonomy that we hope to one day achieve in nanotechnology. In many cases, nature

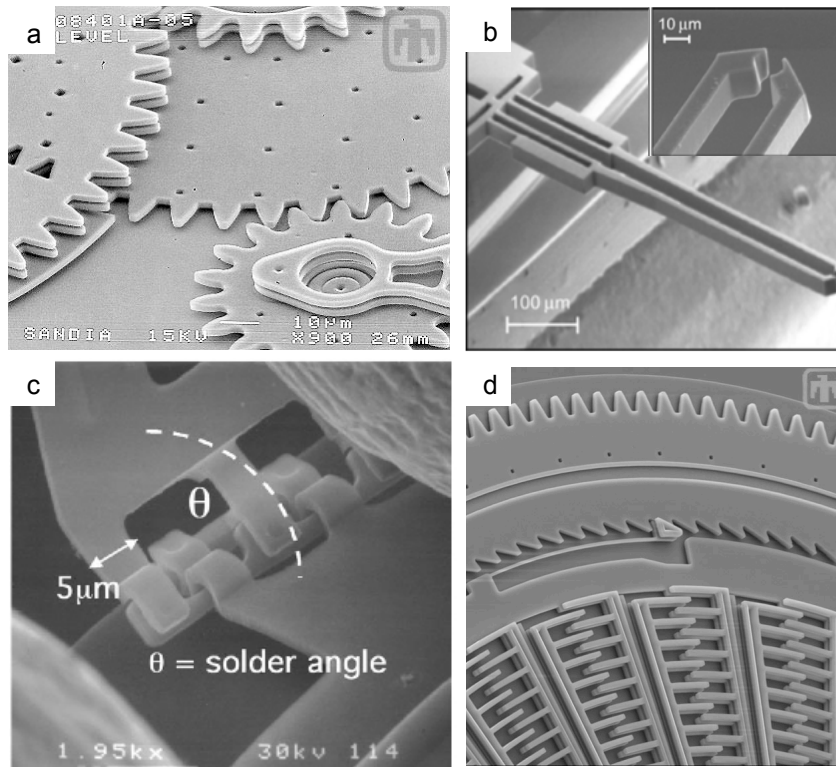


Fig. 1.1: The miniaturization of machines: Gears, grippers, hinges, and ratchets at the microscale. Images from Sandia National Labs; (c) is from Kladitis et al., MEMs 2001.

builds complex moving parts from simpler building blocks, which are folded into more complex shapes with different functionalities. In the case of a protein, a one-dimensional chain of amino acids folds itself into a structure whose three-dimensional shape is critically important.¹³ Two-dimensional membranes build up the three-dimensional folded membrane of the Golgi body. This simple but powerful idea is found at many size scales in nature,^{14,15} and we can draw on it to create new kinds of 3D structures and moving parts. The challenge becomes designing the folds, cuts, and order of assembly, and for that, scientists have begun to draw on the expertise of the paper arts.

1.2 Origami & kirigami in art and science

Origami and kirigami are two different forms of paper art that build complex structures from a flat sheet of paper (*ori*=fold, *kiru*=cut, and *kami*=paper). In origami, the paper is sequentially folded to sculpt a three-dimensional shape (Fig. 1.3). In kirigami, we add cuts to the paper to create additional freedom. While these techniques have been studied in the arts community for many years, they are now beginning to have a significant impact on the sciences. Mathematicians are fascinated by the topology of the paper arts, and there has increasingly been discussion and collaboration between scientists and origami artists.¹⁶

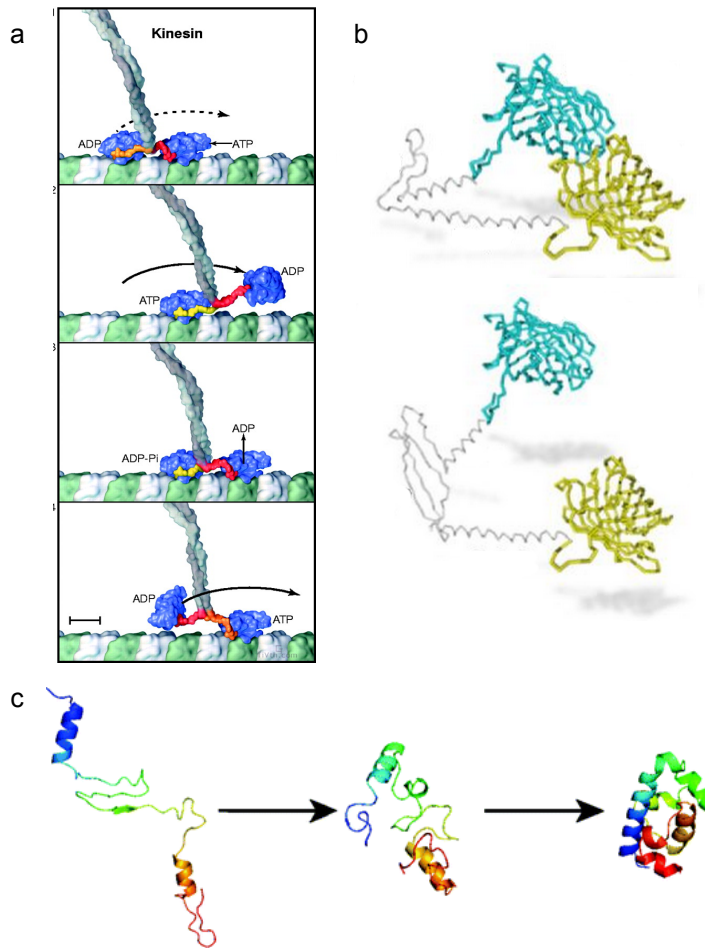


Fig. 1.2: Biology is a master of nanoscale moving parts. (a) Kinesin motor protein is a nanoscale walker. From Vale and Milligan, *Science* (2000) (b) Proteins form hinges that open and close in response to external stimuli. From Caron et al., *PNAS* (2013) (c) Proteins are one-dimensional chains of amino acids that fold into three-dimensional structures. From Bowman et al., *JACS* (2011).

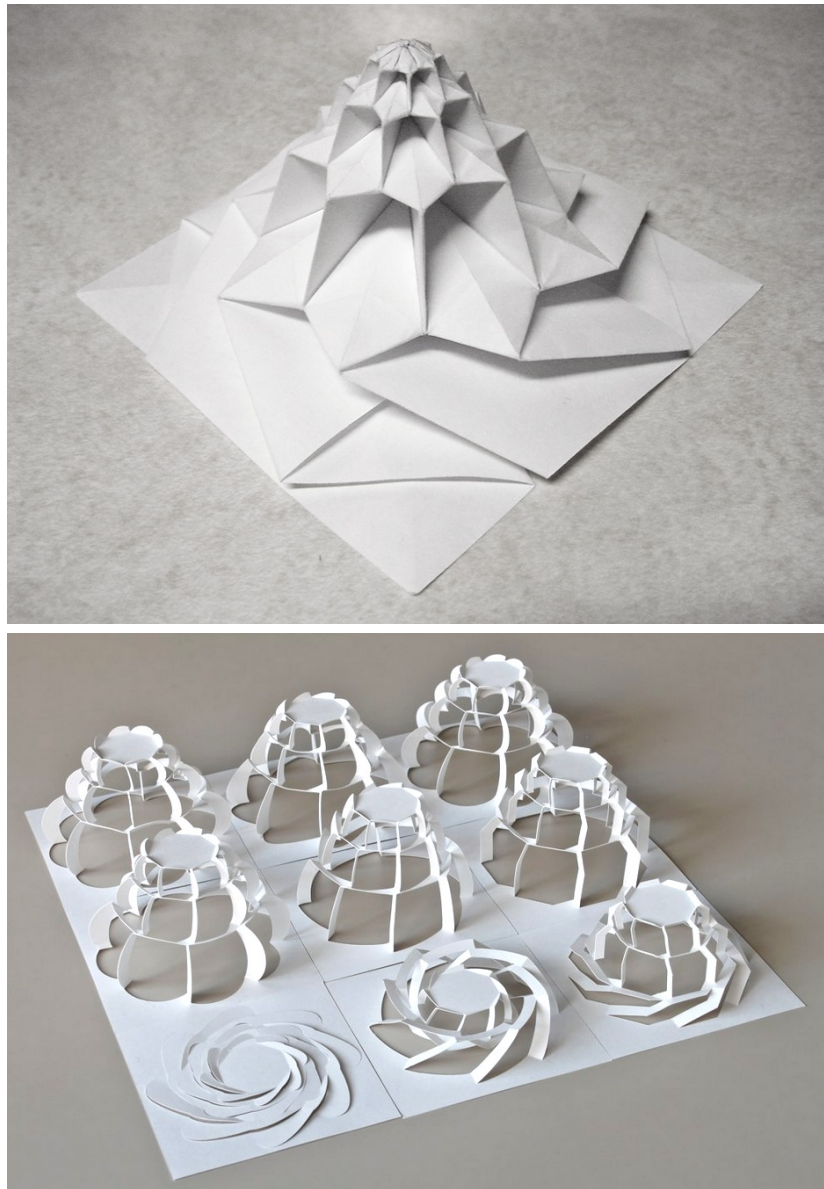


Fig. 1.3: Building similar three-dimensional structures from paper using the techniques of origami (top), which folds the paper, and kirigami (bottom), which cuts the paper. Origami by Chris Palmer and kirigami by Prof. YM.

Ideas from origami and kirigami have been applied to the sciences at all size scales (Fig. 1.4). DNA origami is a fabrication method that uses the one-dimensional nucleic acid chains as a mechanical building block to build two- and three-dimensional nanostructures.¹⁷ Cutting up and reconfiguring these self-assembled structures can result in complex topologies such as Mobius strips¹⁸ and moving parts that actuate in response to certain proteins.¹⁹ At the other end of the size scale, expanding origami patterns have been used in engineering to build structures like heart stents²⁰ and solar panels for satellites.²¹

Paper arts techniques provide a powerful and well-developed toolbox for building different kinds of two- and three-dimensional structures¹⁰ and a variety of moving parts. We can imagine bringing these design principles down to the nanoscale, but to do that, we first need a good “paper.” A nanoscale paper should be strong and flexible, and its ultimate realization would be just one atom thick: a true two-dimensional material. In fact, this material already exists.

1.3 Key properties of graphene as an atomic paper

Graphene is a one-atom-thick sheet of carbon, with atoms bonded together into a hexagonal lattice (Fig. 1.5). There has been a great renewed interest in graphene since 2004, when K. S. Novoselov and A. K. Geim used Scotch tape to mechanically exfoliate it from a flake of high-quality graphite.²² In the years since, researchers from around the world have extensively studied the physics of graphene and have refined techniques for working with it. Graphene is now commonly grown by chemical vapor

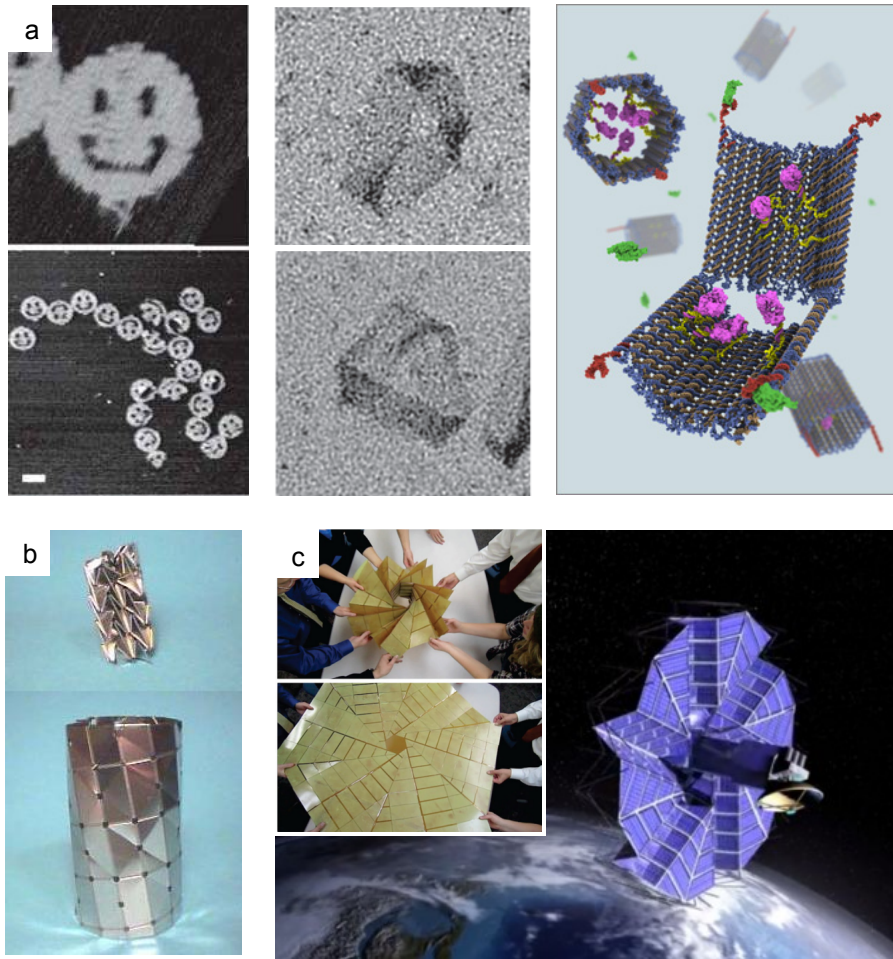


Fig. 1.4: Origami and kirigami in science at all size scales. (a) DNA origami folds a one-dimensional strand of DNA into a two-dimensional structure. Cutting the two-dimensional DNA origami sheets leads to new topologies such as Möbius strips, and folding them gives us hinges and actuable capsules. From Rothemund, *Nature* (2006); Han et al., *Nat. Nanotech.* (2010); and Douglas et al., *Science* (2012). (b) Origami principles applied to a heart stent, and (c) to the solar panels of a satellite. Images from *LA Weekly* and *Wired UK*.

deposition (CVD), resulting in large, continuous sheets of primarily monolayer graphene.²³ We can transfer it across substrates, suspend it over holes, and pattern it using standard photolithographic techniques. Graphene has extraordinary mechanical, optical, and electrical properties, and is beginning to find applications that range from transparent electronics²⁴ to sample mounts for X-ray diffraction²⁵ and electron microscopy,²⁶ and it is still revealing new physics in its role as a model system.

Graphene is a semimetal, with an unusual band structure where the dispersion relation is a linear cone at low energies (Fig. 1.5(c), insets). The electrons interact with the hexagonal lattice to create massless quasiparticles that have direct parallels to relativistic particles, and have led to great interest in graphene as a solid-state model system. This unusual band structure also creates a remarkable optical response: despite being only one atom thick, graphene absorbs $\pi\alpha = 2.3\%$ of incident light, where $\alpha = 1/137$ is the fine structure constant.²⁷ This high opacity means that under the right conditions, even a single layer of graphene is visible to the naked eye.

In addition to its remarkable electronic and optical properties, graphene is also a mechanical marvel. Carbon-carbon bonds are some of the strongest in chemistry, and graphene is the strongest material in the world. Graphene's two-dimensional Young's modulus (in-plane elastic constant) has been directly measured by AFM studies on suspended graphene membranes, giving $Y_{2D}=340$ N/m.²⁸ The breaking stress s_{2D} and strain ε of a material are related through its Young's modulus, where

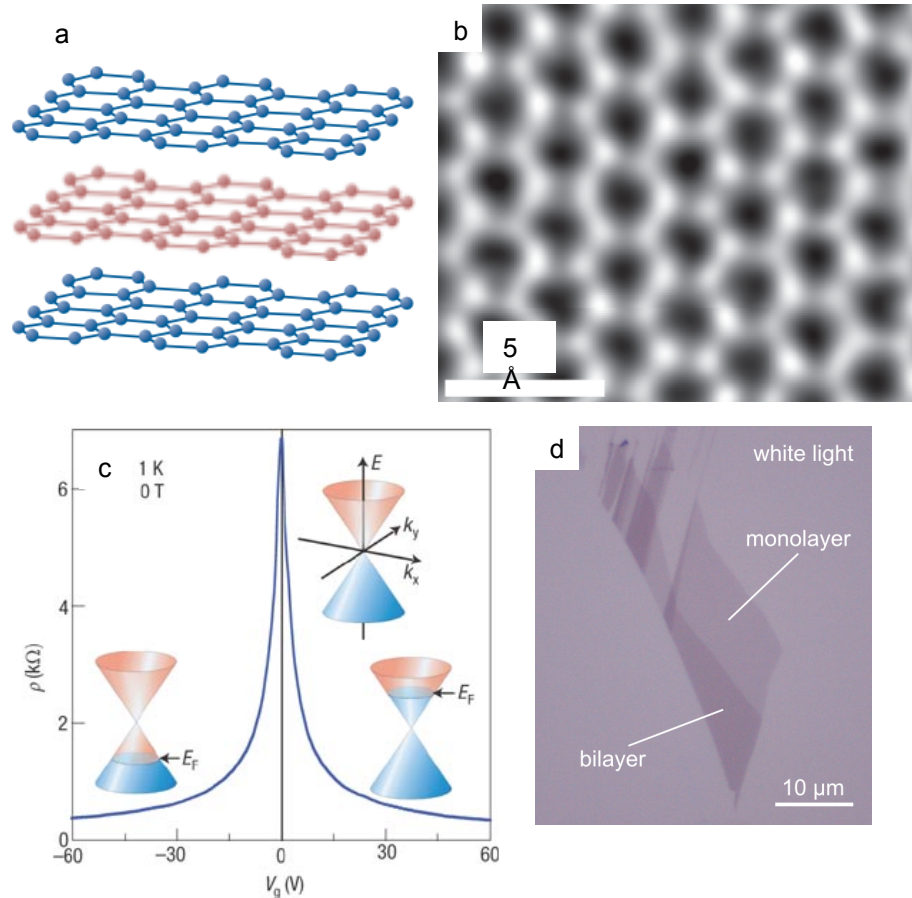


Fig. 1.5: Properties of graphene. (a) Graphite is a stack of two-dimensional atomic layers of carbon atoms; graphene is a single layer. (b) Atomic-resolution transmission electron microscope image of the graphene lattice. From P. Huang et al. (2011). (c) Graphene is a semimetal, with a linear dispersion relation at low energies. As we tune the gate voltage V_g , the Fermi level changes. At the Dirac peak ($V_g=0$ on this graph) the charge carriers switch from electrons to holes. From Geim and Novoselov, Nat. Materials (2007). (d) (Exfoliated graphene on an oxide substrate. We can clearly see monolayer and bilayer regions. The contrast has been increased for clarity, but it can be seen by eye in a white light microscope under the right conditions. From grapheneindustries.com.

$s_{2D} = Y_{2D}\varepsilon$. For suspended graphene membranes, the breaking stress is ~ 42 N/m, corresponding to a strain of $\sim 12\%$.²⁸ CVD graphene membranes typically fail earlier, at strains of $\sim 6\text{-}8\%$.^{29,30}

Large sheets of material are often described as thin three-dimensional plates with a thickness t , where we bend the plate by extending the top half and compressing the bottom half. This approach makes it easy to describe materials using familiar bulk elastic properties and the language of mechanical engineering, such as the three-dimensional Young's modulus Y_{3D} , where $Y_{2D} = Y_{3D}t$. The out-of-plane bending stiffness κ of such a plate is given by $\kappa = Y_{3D}t^3/12(1 - \sigma^2)$ and has units of energy, where σ is the Poisson ratio that describes how much the material contracts or expands in the orthogonal direction. For graphene, $\sigma = 0.17$.

However, at just one atom thick graphene is a truly two-dimensional material, so the out-of-plane stiffness is due to the interactions of the in-plane atomic bonds and not to bulk material properties. As a result, the bending stiffness cannot be reliably extracted from classical elastic theory.³¹ Instead, a value of $\kappa \sim 1.2$ eV was found through simulations³² and measurements of the phonon modes in graphite.^{33,34}

Although this very low value of the bending stiffness is certainly true at the atomic scale, it has never been conclusively measured at the micron scale. In fact, theory suggests that the effects of thermal fluctuations should *dramatically* stiffen larger membranes.³⁵ In Chapters 4 and 5, we will directly measure the bending

2D Young's modulus	Y_{2D}	340 N/m
Poisson ratio	σ	0.17
Breaking stress	s	42 N/m
Breaking strain	ε	6-12%
Intrinsic bending stiffness	κ	1.2 eV

Table 1.1: Relevant mechanical properties of monolayer graphene.

stiffness of micron-scale graphene membranes and compare the results to thermal fluctuation theory for the first time.

Next, we will take a look at how scientists have manipulated graphene in vacuum, air, and aqueous solutions in the past.

1.4 A short history of manipulating graphene

The traditional way to work with graphene is flat on an oxide surface, where it makes conformal contact and strongly sticks down to its substrate by van der Waals attraction (Fig. 1.6).³⁶ This is the most common geometry for optical and electronic experiments on graphene. In the past the graphene was exfoliated directly onto the final substrate, though today many researchers transfer both exfoliated and CVD-grown graphene using a wet process (Chapter 2). Graphene has also been exfoliated or transferred over holes or trenches in a substrate, where it forms beams or tensioned drumheads (Fig. 1.6(c-d)).^{37,38} These suspended devices have taught us a great deal about the in-plane mechanical properties of graphene and are also useful for applications such as resonators³⁹ and balloons⁴⁰ or as ultra-thin substrates for transmission electron microscopy.⁴¹

Graphene is extraordinarily sticky,⁴² so it is usually handled on a substrate or a tensioning frame. However, some tricks have been developed to crumple graphene on an elastic surface,⁴³ to control the tension in suspended devices,^{44,45} and in one lucky

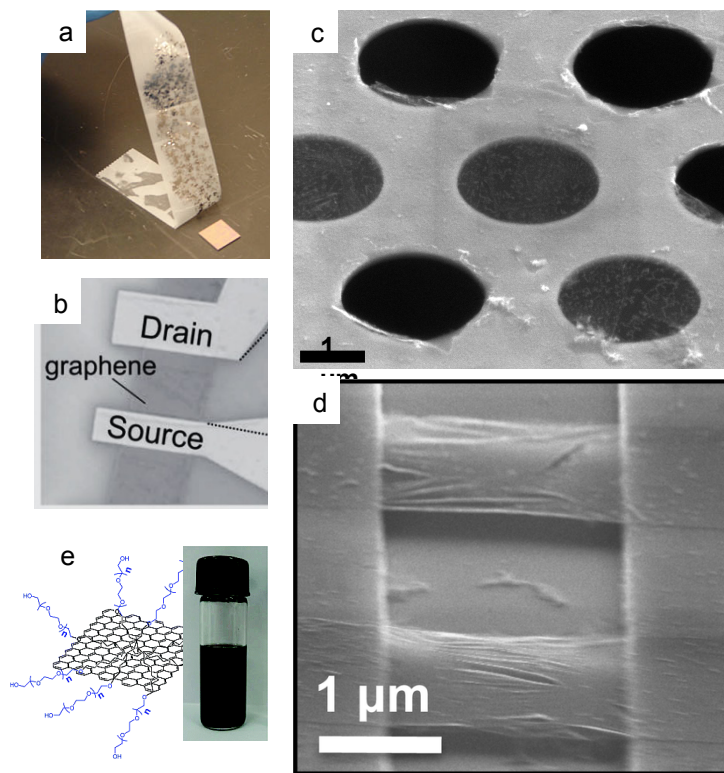


Fig. 1.6: Working with graphene. (a) The mechanical exfoliation process. (b) A graphene transistor on an Si/SiO₂ wafer. (c) An array of suspended graphene membranes on a TEM grid. The graphene looks gray, while uncovered holes in the grid look black. (d) An array of graphene beams suspended over a trench and clamped on both ends to the SiO₂ substrate. (e) Chemically-modified graphene flakes suspended in solution.

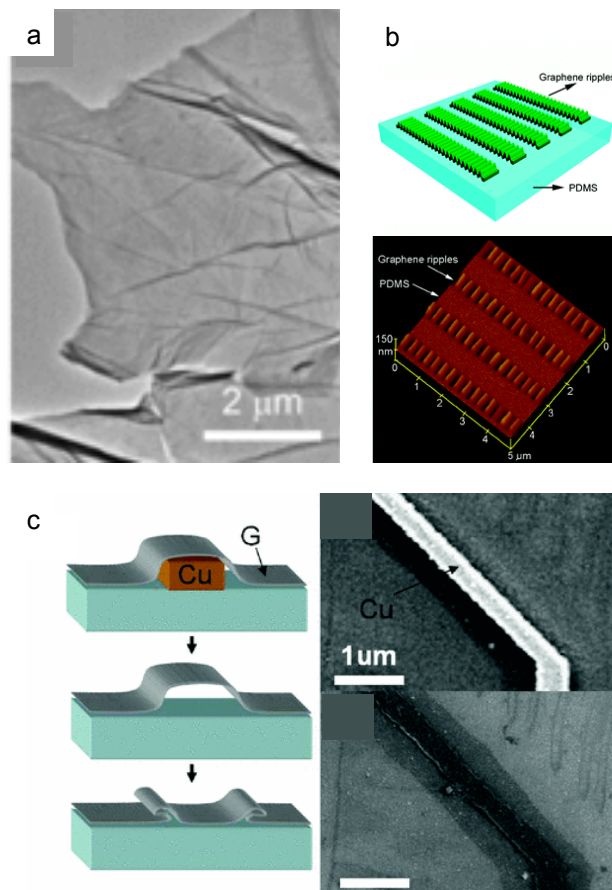


Fig. 1.7: Crumpled and folded graphene. (a) Solution-processed reduced graphene oxide membranes crumple like paper. (b) Graphene strips transferred to a prestrained polymer substrate creates ripples when the strain is removed. (c) Creating folds in graphene by transferring it over sacrificial structures.

accident, to create a free-standing singly-clamped flake.⁴⁶ Work has also been done on putting graphene flakes into liquid suspensions by sonicating graphite with surfactants^{47,48} and using bulk materials processing techniques.⁴⁹

In a few cases, researchers have used innovative methods to fold graphene into permanent structures^{50,51} (Fig. 1.7). Graphene, graphene oxide, and other kinds of nanoscale membranes have also been found in crumpled and folded states.^{52,53,54} However, manipulating graphene in 3D is generally extremely difficult, and has always relied on either random chance or a supporting structure. This significantly limits the structures and moving parts that we can build, and keeps us from using graphene as an atomic paper.

Though crumpled structures such as the one in Fig. 1.7(a) are uncontrollable and permanent, images of folded graphene give us an intuitive sense that graphene acts like a kind of strong (but sticky) sheet of paper. In this thesis, we will develop a way to controllably manipulate graphene free from a surface and control its adhesion, so that we can directly translate ideas from the paper art of kirigami down to the nanoscale. Many people have proposed ways that graphene could be cut and folded at the atomic scale using techniques from the paper arts,^{55,56,57,58,59} and we will experimentally apply these design principles for the first time.

1.5 Outline of this thesis

This thesis is based on a new technique for manipulating graphene on and off of a surface in an aqueous environment. In Chapter 2, we will begin by describing the

fabrication and manipulation methods, and in Chapter 3 we will demonstrate that we can directly and controllably pick up graphene and manipulate it like a sheet of paper.

We will spend Chapter 4 discussing the theory of thermally induced fluctuations in a crystalline membrane, which predicts that the bending stiffness at micron scales should be dramatically increased above this atomic-scale value. In Chapter 5, we will use graphene cantilevers to directly measure the bending stiffness for the first time, and show that the measured value matches the predictions of thermal fluctuation theory.

Next, in Chapter 6 we will import ideas from the paper art of kirigami to create remarkably stretchable in-plane and out-of-plane graphene springs. We will actuate them both directly and remotely, measure their mechanical properties, and predict the wide range of possible spring constants that can be made using this technique. We will electrically contact and gate these devices and show that their electrical properties do not change significantly when the spring is stretched—a highly desirable property for stretchable transistors.

Finally, in Chapter 7 we will discuss ongoing research in our group that aims to develop new actuation techniques and applications for graphene kirigami devices. We will close with proposals for other experiments that might lead to increasingly controllable nanoscale moving parts. We hope that graphene kirigami devices and techniques will inspire many kinds of nanoscale machines in the years to come.

This project has been a truly collaborative effort, and I'd like to take a moment to acknowledge particular contributions that others have made to the work in this thesis—especially significant efforts from Arthur on all chapters, from Arthur,

Samantha, Peter, and Kathryn on the material in Chapter 5, and from Peter, Kathryn, and Pinshane on the material in Chapter 6. This project was made possible by many years of financial support from the National Science Foundation through the Cornell Center for Materials Research, from the Office of Naval Research, and from the Kavli Institute at Cornell for Nanoscale Science.

CHAPTER 2

FABRICATION AND CHARACTERIZATION OF GRAPHENE KIRIGAMI DEVICES

2.1 Introduction

The broad scope of the graphene experiments described in Chapter 1 demonstrates just how widespread graphene growth and fabrication have become. Despite some quirks, this atom-thick material has been quickly integrated into traditional nanofabrication processing, and the fabrication method described in this chapter draws heavily on well-established techniques.^{23,29,24,60} The key difference is the addition of a sacrificial release layer between the graphene and the substrate, which allows us to lift the graphene up off of the surface in an aqueous environment.

This chapter begins with the graphene growth process, and explains how to characterize graphene. We describe the fabrication process for kirigami devices in detail, and explain the release technique. Fabrication is notoriously sensitive to minor changes, and details of the graphene growth and transfer process often vary between labs. With this in mind, this chapter aims to lay out the fabrication and characterization process in detail, so that a new researcher in the field could work from this material alone.

2.2 Growing graphene by chemical vapor deposition

The recent development of chemical vapor deposition (CVD) growth methods mean that graphene fabrication has gone from a serial exfoliation process to a parallel

process. CVD graphene is grown on metal (most commonly copper foil), and can be transferred to arbitrary substrates.^{23,29,24} Researchers can create hundreds or even thousands of devices on a single chip, and graphene is now being grown and transferred at the meter scale in industry.⁶¹ Here we will describe the basic idea behind CVD growth, then provide specific instructions and a recipe for growing graphene.

CVD growth consists of heating a catalytic substrate in a low-pressure environment and flowing carbon-containing gases such as methane over the surface. The gas disassociates, and the carbon self-assembles on the surface (Fig. 2.1(c)). When the pressure, temperature, and gas flow are optimized, monolayer graphene grows outwards from local impurities and these sheets of graphene stitch together where they meet.⁶² Additional layers of graphene can also grow outward from the nucleation sites, creating islands of bilayer and multilayer graphene on top.²³ By adjusting the growth parameters, we can tune the proportion of monolayer to bilayer graphene. For the purpose of this thesis, we will define “good” graphene as primarily monolayer graphene that is well stitched at the boundaries. All the graphene used in these experiments was predominantly single-layer, with small bilayer patches.

Graphene growth takes place in a commercially available furnace (Fig. 2.1(a)) with computer-controlled gas flow and temperature management. A turbo pump keeps the growth chamber at low pressures (when no gases are flowing, the pump should achieve pressures of $\sim 10^{-5}$ mBar or lower). The growth substrate is copper foil purchased from Alpha Aesar, stock #13382.

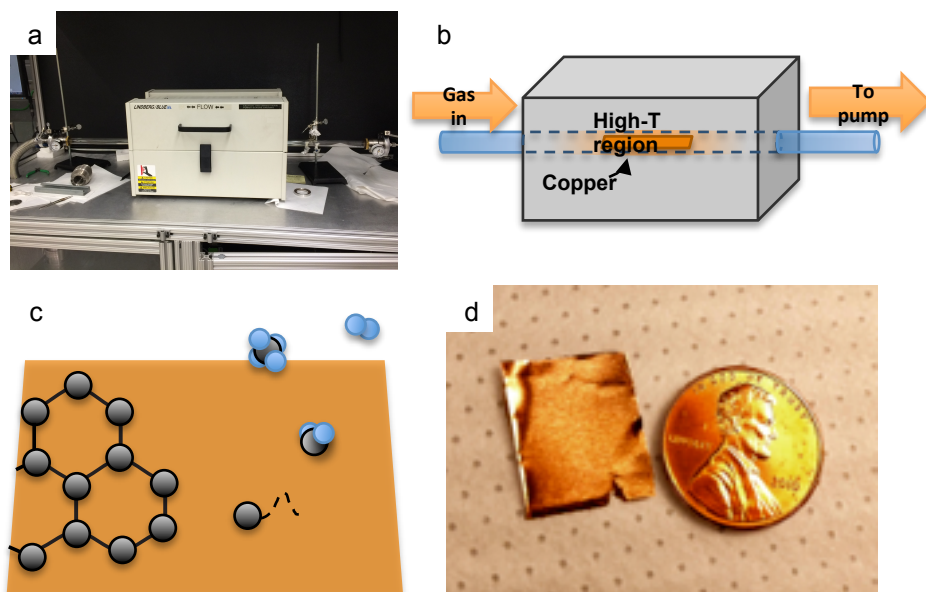


Fig. 2.1: CVD growth of graphene. (a) Commercially-available furnace built into a custom graphene growth system with gas flow controllers and a vacuum pump. The furnace is kept in a hood because the white high-T ceramic is an inhalation hazard. (b) Schematic of the furnace during growth. (c) A cartoon of the growth process. Methane disassociates; the hydrogen becomes H_2 , and the carbon atoms diffuse across the surface and self-assemble into a graphene lattice on the copper surface. (d) Copper foil after growth, with a penny for scale. The entire surface of the foil is covered with graphene.

The growth process is based on Li et al. (2009).²³ We begin by cutting a piece of copper foil to approximately 0.75”×4”, where the shorter dimension is limited by the 1” inner diameter of the quartz growth tube. We are particularly careful to keep the foil as flat as possible to avoid cracking the graphene. We place the copper in the growth area of the furnace (the center ~5” of the quartz tube shown in Fig. 2.1(a-b)) and pump until the pressure has reached $<10^{-5}$ mBar. We then anneal the copper for 36 minutes at 980 °C with a H₂ flow of 60 standard cubic centimeters per minute (s.c.c.m.) to drive oxygen off of the surface. We raise the temperature to 980 °C, and flow hydrogen gas at 60 s.c.c.m. and CH₄ at 36 s.c.c.m for 20 minutes. This is when the graphene grows, so the time can be adjusted to tune the monolayer and bilayer coverage. Finally, we cool the copper in a matching environment as quickly as possible. We then bring the growth chamber up to ambient pressure, remove the foil from the furnace, and cut it into ~0.75×0.75” pieces for transfer (Fig. 2.1(d)).

Despite its apparent simplicity, CVD growth is a finicky process, and the growth quality is inconsistent and can depend on the history of a furnace or the brand of copper film. We have found that graphene quality can even change from one day to the next, so growth-by-growth characterization has become a standard part of the process.

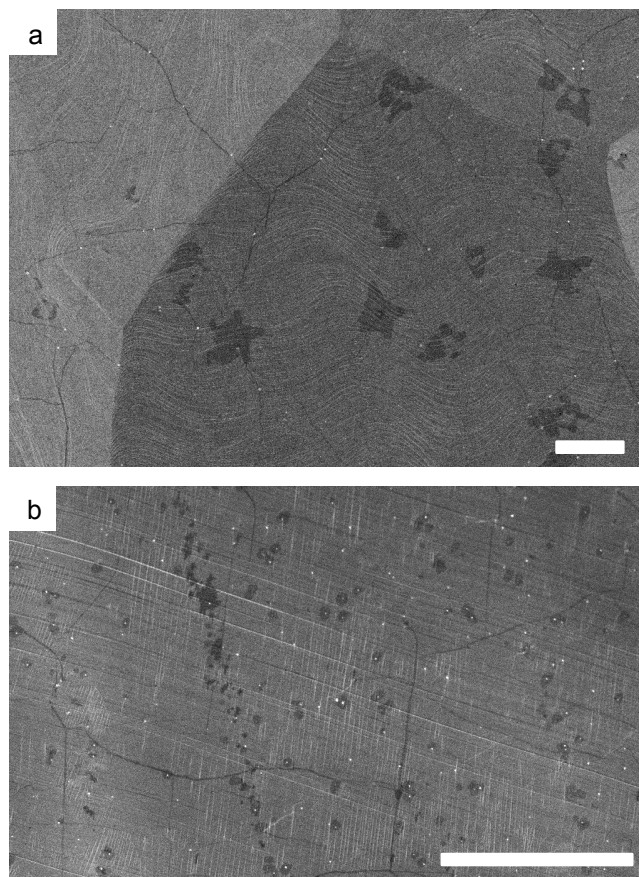


Fig. 2.2: SEMs of CVD graphene. (a) Results of growth recipe described in the text. The large-scale gray patches are copper grains, while the smaller star shapes are graphene bilayer and multilayer patches growing outward from nucleation sites (usually contaminants). (b) The results of a growth from a similar recipe and different furnace. The bilayer patches are much smaller and closer together. Scale bars 10 μm .

2.3 Characterizing graphene grown by CVD

We use a combination of three characterization techniques to determine the quality of a graphene growth: SEM, Raman spectroscopy, and TEM. Each technique provides different information about the graphene, and combining all three techniques builds up a picture of the graphene's coverage, quality, and grain structure.

The simplest and most instructive method for the preliminary characterization of graphene is scanning electron microscopy (SEM). SEM is particularly good at providing large-scale information about bilayer coverage. We show SEMs of a growth from the recipe described above (Fig. 2.2(a)) and a similar recipe in a different furnace (Fig. 2.2(b)). The large-scale flat gray areas show the underlying copper grain structure. The graphene ignores the copper grain boundaries and grows across them. Monolayer graphene covers the entire surface of the copper in these images, which is impossible to tell from the SEMs alone but can be conclusively determined with Raman spectroscopy. The small dots are particles of contaminants, and they can act as nucleation sites for graphene growth. The characteristic star shapes are graphene bilayer patches, and at their centers we often see additional layers of multilayer graphene. SEMs give us a simple visual indication of the cleanliness and multilayer coverage, and the small multilayer stars give us an indication of the nucleation density (it should be noted that a nucleation site usually *does not* represent a single grain, however, as described in the TEM section below).

Unlike SEMs, Raman spectroscopy can give us a direct measurement of the layer thickness (Fig. 2.3). Raman spectroscopy measures the change in frequency of

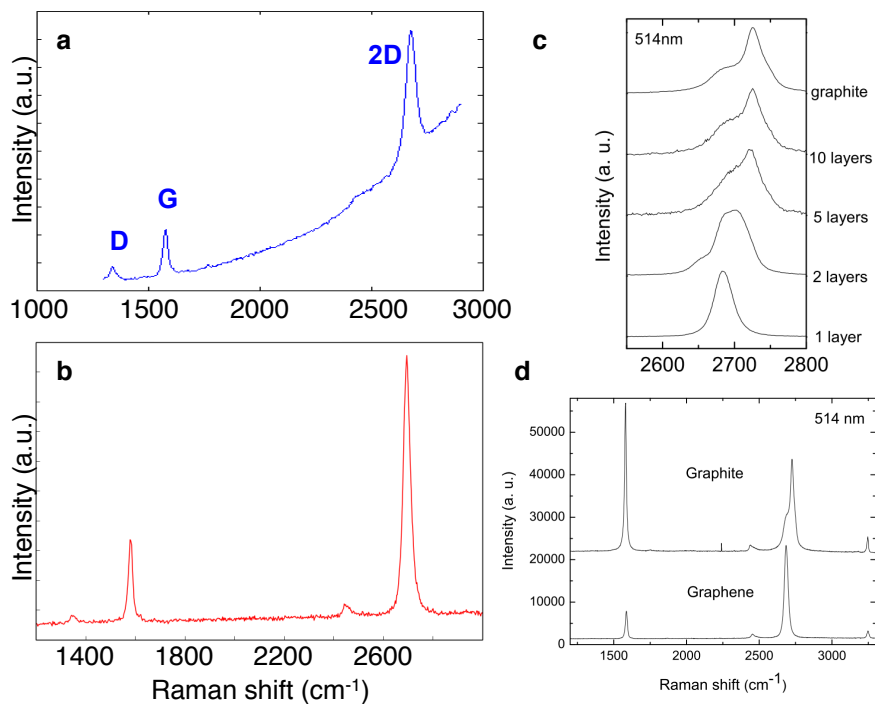


Fig. 2.3: The Raman spectrum of graphene. (a) Raman spectrum of CVD graphene on copper. The overall tilt is due to the copper foil. (b) Raman spectrum of a similar growth after transfer to an Si/SiO₂ substrate. In both cases, the spectrum shows graphene's characteristic G peak at 1580 cm⁻¹ and 2D peak at 2700 cm⁻¹; the ratio between the two indicates that the graphene is primarily monolayer. A small D peak at 1350 cm⁻¹ indicates low disorder. (c) How the 2D peak changes with additional layers, and (d) a comparison of the spectrum of monolayer graphene and graphite. Graphs (c) and (d) are from A. C. Ferrari et al., Phys. Rev. Lett. (2006).

monochromatic light when it inelastically scatters from phonons in the graphene's crystal lattice. Because this technique provides information about the characteristic phonon modes, it can be used to reliably identify monolayer and multilayer graphene, and to provide some limited information about disorder in the lattice.⁶³ The spectra of monolayer and bilayer graphene are well established. Fig. 2.3(a) shows a spectrum from a graphene growth on copper, and Fig. 2.3(b) shows a spectrum from a similar growth after it has been transferred to an Si/SiO₂ wafer. The spectrum shows graphene's characteristic *G* peaks at 1580 cm⁻¹ and *2D* peak at 2700 cm⁻¹. The shape of the *2D* peak (Fig. 2.3(c)) and the high ratio between the heights of the *2D* to *G* peak (Fig. 2.3(d)) indicate that the graphene is primarily monolayer.⁶³ A small *D* peak at 1350 cm⁻¹ indicates some low disorder. The *D* peak is absent in perfect graphene, and it usually increases after the transfer process.

Dark-field transmission electron microscopy (DF-TEM) is the most involved characterization technique, but it is a powerful tool that gives detailed information about the grain structure of the graphene (see Huang, Ruiz-Vargas, van der Zande⁶²). To image graphene in a TEM, we must transfer small pieces of graphene to 10-nm-thick Si₃N₄ TEM grids using the process described later in this chapter. In Fig. 2.4(a), high-contrast bright-field TEM shows that the graphene is monolayer in the transferred region and reasonably clean (we see very little particulate residue from the transfer process). If the TEM grid was covered by a single crystal of graphene, the dark-field diffraction pattern should show a sixfold-symmetric pattern, as in the

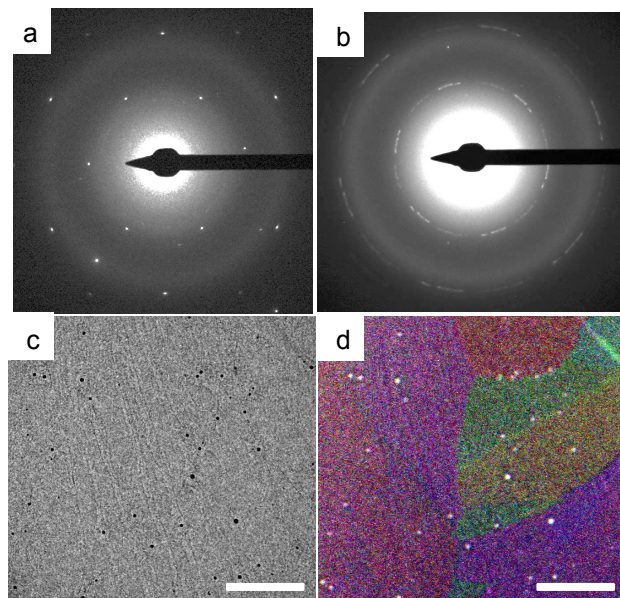


Fig. 2.4: TEM of CVD graphene. (a) TEM diffraction pattern for a single crystal of graphene. Note the characteristic six-fold symmetry. (b) TEM diffraction pattern for region shown in c and d. The many spots show that this region consists of many grains with varying orientations. (c) High-contrast bright-field TEM image of graphene transferred over 10-nm-thick Si_3N_4 windows shows continuous monolayer graphene with low particulate contamination. The grain structure is not visible. (d) False-color composite image of dark-field TEM images showing grain size and shape for the region in c. The graphene is polycrystalline, with grain sizes on the order of microns. Scale bars 1 μm .

sample shown Fig. 2.4(a). However, for this growth we see a large collection of spots, (Fig. 2.4(b)), indicating that the graphene is polycrystalline. Using an aperture to select for a single spot, regions of the graphene lattice with matching angular orientation are highlighted. By false-coloring each of these sets of diffraction spots, we can build a composite image that shows the sizes and shapes of the graphene grains (Fig. 2.4(d)).⁶² This graphene is polycrystalline, with grain sizes on the order of microns. The experiments in this thesis use graphene with grain sizes on the order of hundreds of nanometers to tens of microns. We have recently grown graphene with grains larger than 100 μm , but preliminary attempts to build kirigami devices from this graphene have failed because it has not adhered to the substrates after transfer. It is not yet clear whether these limited attempts were due to the grain structure or to other unknown problems with the fabrication run.

Once graphene is characterized, we are ready to use it in our fabrication process, which we will describe next.

2.4 Device fabrication, graphene transfer, and the release process

The fabrication of graphene kirigami devices is straightforward and requires only standard nanofabrication equipment. Starting with characterized graphene on copper, the whole fabrication process takes approximately three days (Fig. 2.5).

Substrate fabrication: The experiments will take place on an inverted white-light microscope, so we fabricate devices on 170- μm -thick, 500-mm, double-side-polished fused silica wafers (Mark Optics) that approximate glass cover slips. We

begin by rinsing a fused silica wafer with acetone and IPA, then spinning photoresist (prime with P-20 for 10 seconds and spin off; add SPR700 1.2 and spin for 45s at 1000/4000 RPM; bake on a 95°C hotplate for 60s). We expose alignment marks on the stepper (5x i-line Autostep, 0.25 seconds), then develop the wafer in water-based 726 MIF developer, rinse with DI water, and dry with nitrogen. The lithography details are the same for every step of the fabrication process, and will not be described in detail again.

To create the sacrificial layer, we evaporate 30-40 nm of aluminum in an e-beam evaporator. We spin photoresist again to create a protective layer, then cut the wafer into 1”-square chips on a dicing saw. Finally, we soak the chips in acetone for at least one hour, sonicate for 10 minutes to lift off the aluminum in the alignment marks, then rinse with IPA. The chips are now coated in an aluminum sacrificial layer with alignment marks, and are ready for graphene transfer.

Note that water developer slightly etches the aluminum, so the substrate will start to look “mottled” as the fabrication runs through the following two developer steps; this does not seem to significantly affect the release process, though it does make the chip difficult to characterize until the aluminum is removed in the final etch.

Graphene transfer: Transfer of CVD graphene from copper to other substrates is a well-established process, and many variations have been developed for specialized applications.^{29,24,60,64,10} We add a layer of Poly(methyl methacrylate) (PMMA) to the top of the graphene to give it additional mechanical stability. To create a uniform film of PMMA, we place the copper foil on a spinner, add three drops of

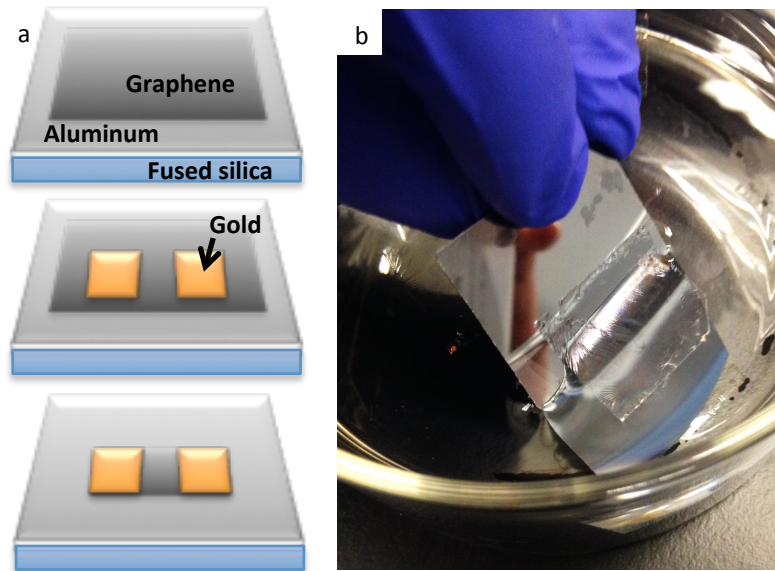


Fig. 2.5: Fabrication and transfer process. (a) We transfer graphene to a fused silica chip covered in a sacrificial aluminum layer. We then add gold pads, and pattern the graphene to create cantilevers and kirigami patterns. (b) Rinsing the graphene during transfer. After five DI water baths, we scoop the graphene/PMMA film onto the final, aluminum-coated substrate.

PMMA (2% or 4% in anisole solvent), and spin at 3000 RPM for 30 seconds. (If the foil is particularly crumpled, it can be taped to a glass slide that is mounted on the spinner.) We then bake the foil on a hotplate at 90°C for one minute to drive off remaining solvents. Finally, we gently scratch the back of the copper foil with steel wool to remove the graphene from the back side, since it can slow down the etch process or accumulate on the edges of the PMMA/graphene film.

We etch away the copper by floating it PMMA-side-up in ferric chloride (Transene, CE-200) until the copper has dissolved away, approximately one hour. Using a silicon wafer or glass slide, we scoop the graphene/PMMA film into a series of five water baths (Fig. 2.5(b)), soaking for five to ten minutes in each bath. We then transfer it onto the final substrate, where it dries. The graphene is directly adhered to the substrate, with PMMA on top. Finally, we remove the PMMA by soaking the chip overnight in acetone, sonicating for 10 seconds, then rinsing with isopropanol (IPA) and drying with nitrogen. (For the transfer to TEM grids mentioned above, we instead bake the PMMA off in a furnace at 300°C for three hours in air.)

Once the graphene is transferred to the aluminum-coated chip and the PMMA has been removed, we are ready to pattern the devices. The first step is patterning gold pads in a variety of sizes and shapes; these will act as handles to manipulate the graphene. We will see below that we can directly push on the graphene with a probe tip, but gold pads offer more control. Gold sticks to graphene, and is soft enough that we can drive a probe tip into the pads to “grab” a graphene device. We pattern these pads using the photolithographic process described earlier, then evaporate 50 nm of gold on the e-beam evaporator. We perform the lift-off in acetone and briefly sonicate

for 10 seconds. Note that the evaporation rate should be high (>5 angstroms/sec), and that the rate must be kept constant to avoid building strain into the evaporated film.

Patterning devices: Next, we repeat the lithography process to pattern the graphene into shapes. We again spin photoresist and pattern it to create areas where the graphene is protected by photoresist. We etch away the rest of the graphene in a short oxygen plasma (Oxford 81: 50 s.c.c.m. of O_2 at 60 mTorr, 150 W for 25 s). Finally, we drop the chip in acetone that is already sonicating, and let it sonicate for 10-20 seconds. The plasma etch process can “bake” the top layer of photoresist into a hard shell, and dropping the chips into sonicating acetone helps remove this shell before it can stick down. Finally, we let the chips soak overnight in acetone, and rinse and dry them.

Release layer etch: The last step in the fabrication process is the aluminum etch. We simply soak the chip in a $\sim 10/1$ DI water/HCl solution until the aluminum is completely gone. The acidic solution dissolves it away, leaving the graphene devices loosely adhered to the surface. The etch rate of the aluminum depends on the acidity of the solution and the amount of aluminum oxide on the chips; in most cases a few hours is enough, but the chips can be left overnight in etchant. After etching, we move the chip to a DI water bath, and from this point on the chip be never dried. We keep the chip in a refrigerator when not in use to prevent bacteria growth; when stored for long periods (months or more), the chips are stored refrigerated in 70%/30% ethanol/DI water to further reduce bacterial growth.

The graphene devices are now loosely adhered to the substrate, and are ready for experiments. A good fabrication run should result in four to six chips covered in

hundreds or thousands of graphene devices. By placing the wet, etched chip on a transmission white-light optical microscope and turning up the contrast (Fig. 2.6), we can clearly see the gold pads (black in the transmission image) and the patterned graphene (gray). In a successful fabrication the graphene should be well patterned and continuous, and most of the devices should remain on the surface.

The aluminum sacrificial layer makes these chips particularly hard to characterize during the fabrication process, and it can be difficult to tell by eye whether the resulting devices are clean of residues. Graphene is a particularly “sticky” material, and organic residues from the lithography and transfer process cannot be etched away in an oxygen plasma without destroying the graphene. In many cases the cleanliness of the graphene may not be critical, but a thick layer of organic residue could affect the mechanical behavior of the graphene and we will need to know how much residue remains when we measure the graphene’s bending stiffness in Chapter 5.

2.5 Determining the amount of residue on completed devices

Atomic force microscopy (AFM) gives a quantitative measurement of the step height from the substrate to the graphene, and we can use it to determine how much residue is left at the end of the fabrication process. However, the pockmarked aluminum release layer becomes a problem when we try to image the pre-etch chips. To avoid this issue, we created a second, inverted aluminum-layer mask where the alignment marks are aluminum, and the rest of the chip is a bare fused silica substrate. By running this characterization chip entirely in parallel with the working devices—

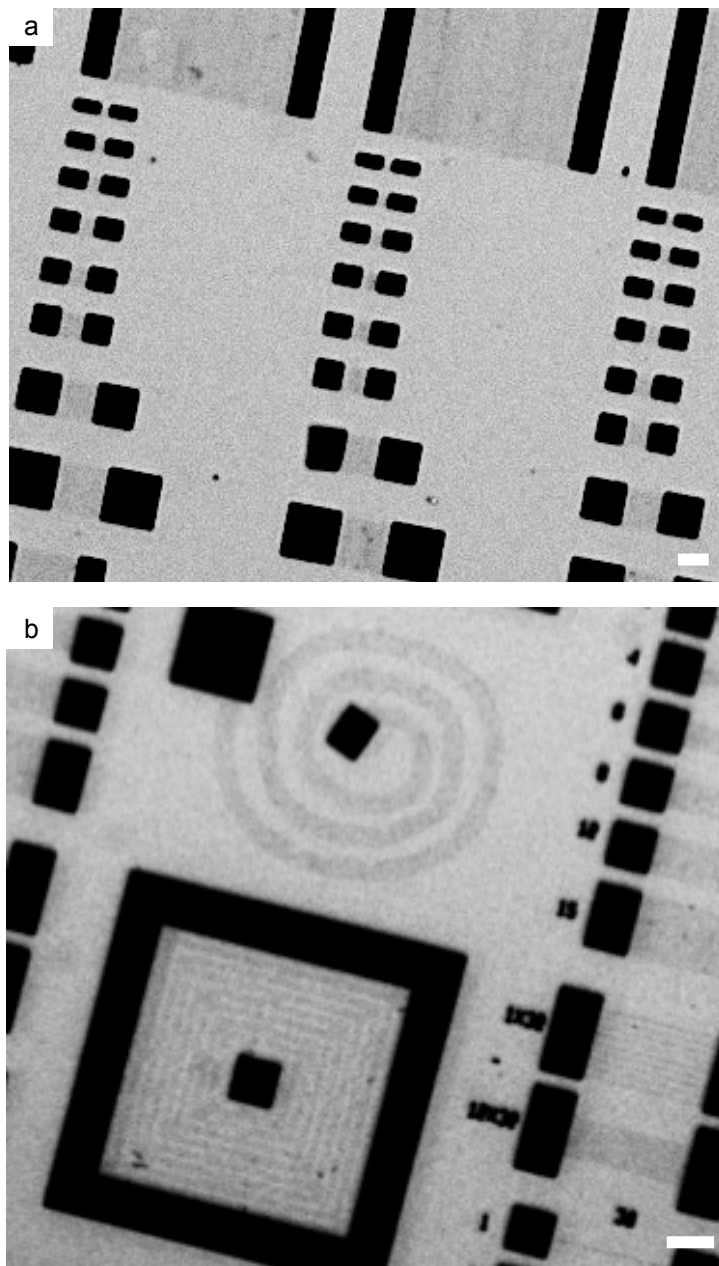


Fig. 2.6: Finished devices. (a) A variety of different patterned graphene cantilevers. (b) Other cantilever shapes and kirigami devices. The gold pads look black, and the graphene is gray. The contrast has been increased linearly so that the graphene is visible. Scale bars are 10 μm .

transferring graphene from the same growth with the same transfer process, placing it in the oxygen plasma at the same time, etc.—we can be reasonably confident that this characterization chip should give us information about the cleanliness of the working devices. Fig. 2.7 shows AFM data for representative characterization chips, as well as for a sample piece of exfoliated graphene on Si/SiO₂ that has never been exposed to polymers. All data is taken on the same AFM with the same scan parameters.

Pristine exfoliated graphene commonly gives a step height of ~1 nm. (This may seem counterintuitive, given that the interlayer spacing of graphite is 0.34 nm, but larger step heights can be the result of changing tip-substrate interactions as the scan moves onto the graphene, and can also depend on the scan parameters.⁶⁵)

These finished (post-fabrication) CVD graphene chips typically have step heights of 2-3 nm. In general, polymer-based transfer is known to leave ~1-3 nm of residue on the surface of graphene.⁶⁶ While it is impossible to completely avoid residue, this amount of residue should not be significant enough to significantly affect the graphene's mechanical properties (see Chapter 5).

A shorter transfer time seems to help in reducing the residue. This means minimizing the time the PMMA is in contact with the graphene, ideally to ~3 hours. The plasma etch step is another point where significant residue can appear, so care should be taken to pre-clean the empty chamber with an O₂ plasma for ten minutes before the etch. As mentioned earlier, dropping the chips directly into sonicating acetone also helps kick off any photoresist “shell” baked on by the etch process.

In some cases, problems with the fabrication process have resulted in thick

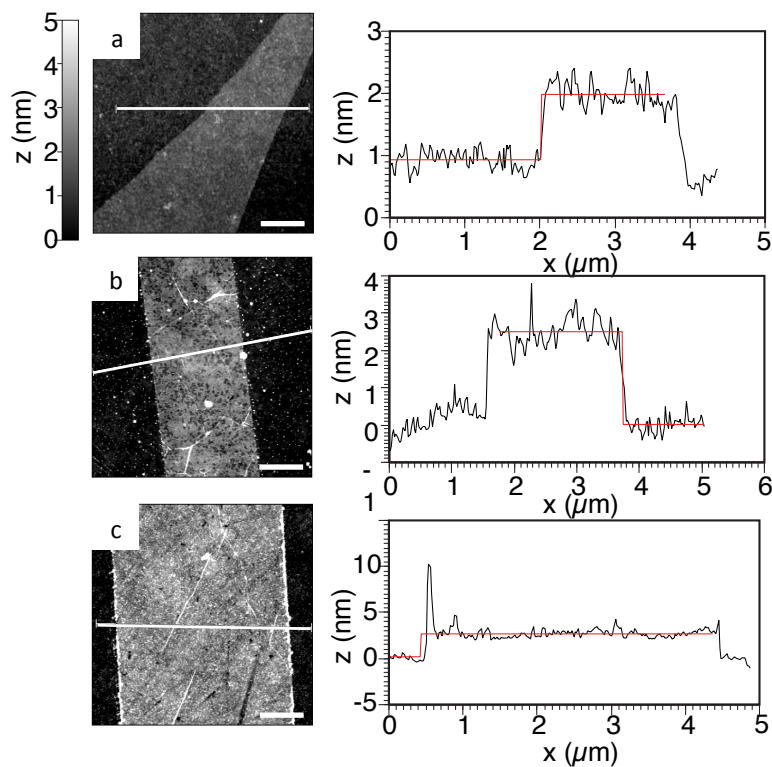


Fig. 2.7: Determining the residue on characterization chips. (a) Exfoliated, unprocessed monolayer graphene. Step height along the line shown on the height map measures 1.0 ± 0.3 nm. (b) and (c) Representative data from aluminum-free chips run in parallel with the devices used in bending stiffness measurements. Step heights are 2.5 ± 0.4 nm and 2.4 ± 0.5 nm. Chips that look clean under the optical microscope typically measure 2-3 nm total step heights. We occasionally see higher residue lines at the edges of the graphene, as in c. Scale bars are $1 \mu\text{m}$.

layers of residue, up to tens or even hundreds of nanometers. This much residue is usually visible by eye on the optical microscope as we change the focus, and such a significant, continuous layer of polymer can of course have dramatic effects on the mechanical behavior of the graphene devices. In some cases, we have seen thick layers of residue with built-in strain, so that released devices curl up when released (see Chapter 7), and in one dramatic case we created a film so robust that it held together even when the graphene was torn, and visibly stretched like a sheet of plastic. This behavior is rare, and a well-optimized fabrication process should be reasonably reliable, but parallel-processed characterization chips should still be treated as a standard part of the fabrication process.

2.6 Controlling the adhesion to the substrate

The manipulation technique described in Ch. 3 will rely on the controllable “stickiness” of the graphene/fused silica interface. The graphene devices must stick to the surface well enough to survive the etch process, but not so strongly that the graphene tears when we pick them up. Luckily, this adhesion can be controlled by a number of different variables. A longer etch will generally release the devices more completely. Different etchants can also have a dramatic effect on the adhesion of the devices. KOH slowly etches the fused silica itself, so that the devices are entirely removed from the surface after even a short etch. We have also found that a multi-layer Al/Al₂O₃ stack (made by evaporating half of the aluminum, letting the wafer sit overnight in air, and evaporating the rest) is much more effective at releasing the

devices. Depending on the experimental goal, these parameters can be tuned to achieve a particular relative stickiness.

2.7 Conclusions

The straightforward fabrication techniques described in this chapter will allow us to pick graphene up off of a surface and manipulate it directly, treating it like a sheet of paper. This represents an entirely new way of interacting with graphene, and provides us with a remarkable intuitive understanding of this nanoscale material, but it relies on well-understood fabrication techniques and standard tools. In the next chapter, we will describe the experimental apparatus, and show that the release of graphene from a surface lets us crumple, fold, and pick it up.

CHAPTER 3

DIRECTLY MANIPULATING GRAPHENE ON AND OFF OF A SURFACE

3.1 Introduction

At the end of Chapter 2, we etched away a sacrificial layer to release graphene from the substrate. In this chapter we will examine how the released graphene behaves when we push and pull on it, and lift it up into the water. We begin by describing the experimental apparatus. We then use a micromanipulator to push on large sheets of graphene that have been released from the surface, and find that they crumple and uncrumple like sheets of paper. We also strike these large sheets with a laser, which causes permanent and uncontrolled crumpling.

We next describe moving and lifting simple rectangular cantilever devices, then pick up spirals of graphene to create a three-dimensional shape. Finally, we use graphene's freedom from the surface to create a remarkably resilient monolayer graphene hinge. These techniques represent an entirely new way of working with graphene, and provide us with a vivid physical intuition for this atom-thick material.

3.2 Experimental apparatus

These experiments take place on a transmission white-light microscope (Fig. 3.1). A z-piezo on the objective gives us control over the height of the focal plane (Piezosystem Jena, controller #NV 40/1 CL E; objective mount #83565). For most of the images shown in this thesis, the objective is a 40x, 0.9 NA air objective, though we

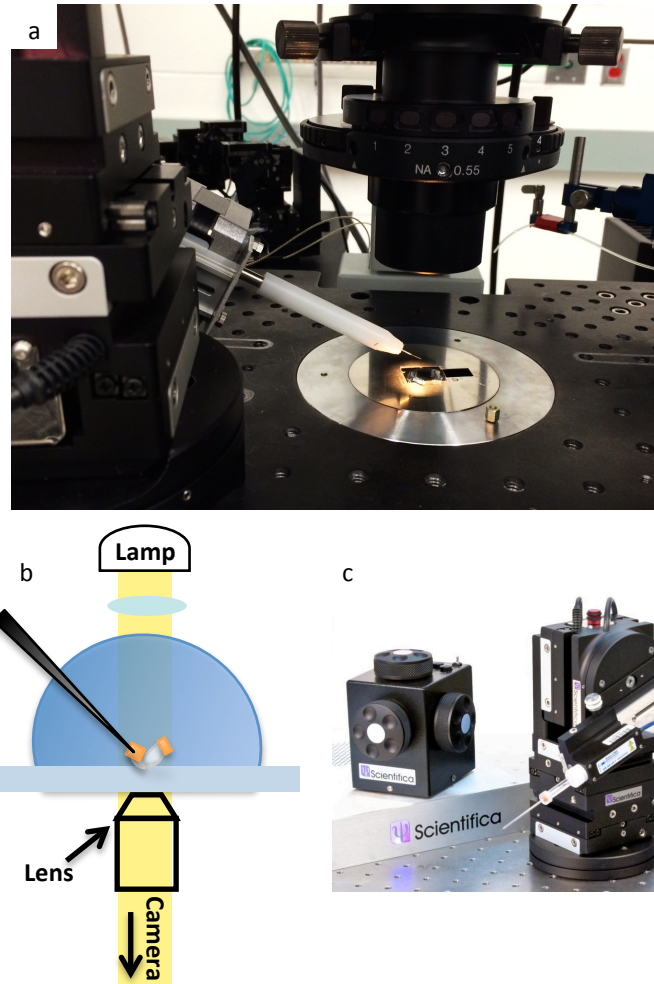


Fig. 3.1: Experimental setup. (a) The optical microscope, with the PatchStar mounted on the stage. (b) Schematic of a graphene kirigami chip sitting on an inverted microscope and covered in a droplet of water (figure courtesy of Samatha Roberts). (c) Computer-controlled PatchStar micromanipulator and control cube.

also occasionally use a 20x, 0.45 NA objective for imaging larger areas. Video is imaged on a CCD, and fed into a custom LabVIEW program (*SonyCamera6.vi*) that records video with customizable contrast and frame rates, and can record additional information about the location of the PatchStar and the height of the z -piezo. The apparatus includes a number of lasers as well as custom-built magnetic manipulators (see Chapters 6 and 7 for details).

The setup includes three computer-controlled micromanipulators that we can use to controllably push a probe tip against the graphene or into the attached gold pads. We primarily use a PatchStar from Scientifica, which is designed for patch-clamp and can be controlled by hand using a control cube. Software is available for making repeated motions. The PatchStar is based on a stepper motor and offers up to 20 nm resolution. We also occasionally use a set of two piezo-controlled manipulators from Sensapex, especially for electrical measurements where we need more than one probe at a time. For mechanical manipulation, we use tungsten probes from Signatone (#SM-35, 0.7- μm tip diameter).

To load a finished chip onto the microscope after the aluminum etch, we pull it out of its water bath, dry the back by setting it on a paper wipe, and place it on the microscope stage. We pipette a few drops of DI water or surfactants onto the top of the chip, and add more water every 15-30 minutes as it evaporates. Surfactant further reduces the graphene's adhesion to the surface and prevents the graphene from permanently sticking to itself. We used sodium dodecylbenzenesulfonate (SDBS) from Sigma-Aldrich (product #289957), dissolved in DI water to a concentration of ~ 3

mM. This is a common surfactant used in solution studies of graphene flakes and carbon nanotubes.^{67,47} Surfactant was used in all of our experiments except for a bending stiffness control experiment in Chapter 5, where we confirm that it has no measurable effect on the bending stiffness.

3.3 Pushing on large sheets of graphene

Monolayer graphene is very soft out of plane and conforms closely to the surface, so the van der Waals attraction is particularly strong for graphene on a flat surface.³⁶ When graphene is stuck down to its substrate after the traditional fabrication procedure, we cannot peel it up without tearing it. If we drive a probe against the surface, we simply scratch off the graphene, as in Fig. 3.2.

After a sacrificial layer etch, however, the graphene is adhered much less strongly to the surface. This can be dramatically illustrated by pushing the probe tip against the edge of a large sheet of graphene (Fig. 3.3). Rather than scratching and tearing, the graphene sheet holds together and releases from the surface. By continuing to push, we can crumple it dramatically. If the sample is in water the graphene remains mostly crumpled, but with surfactant the graphene does not permanently stick to itself, and we can uncrumple it by pulling back with the probe. The sheet returns almost exactly to its original shape, demonstrating graphene's remarkable resilience (Fig. 3.3(c)). By pushing and pulling at large sheets of graphene, we can begin to build up an intuition for the mechanics of this truly nanoscale material.

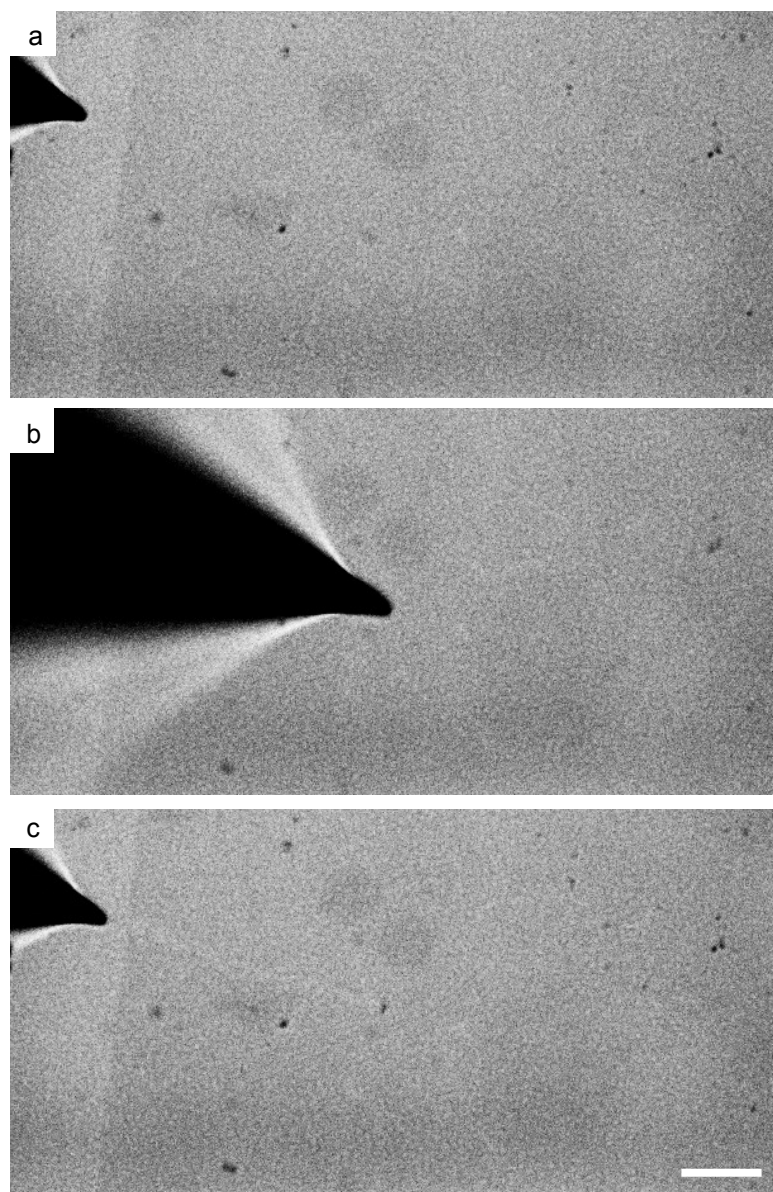


Fig. 3.2: Pushing a probe tip against a large sheet of unreleased graphene. (a) Graphene transferred directly to fused silica without a release layer. Note the visible bilayer patches. (b) We push the probe against the surface, (c) then retract the probe. The graphene is stuck to the surface and scratches under the probe tip (the faint line left behind in the bottom image). As in the rest of the experiments, this chip is in water and surfactant. Scale bar is $\sim 10\ \mu\text{m}$.

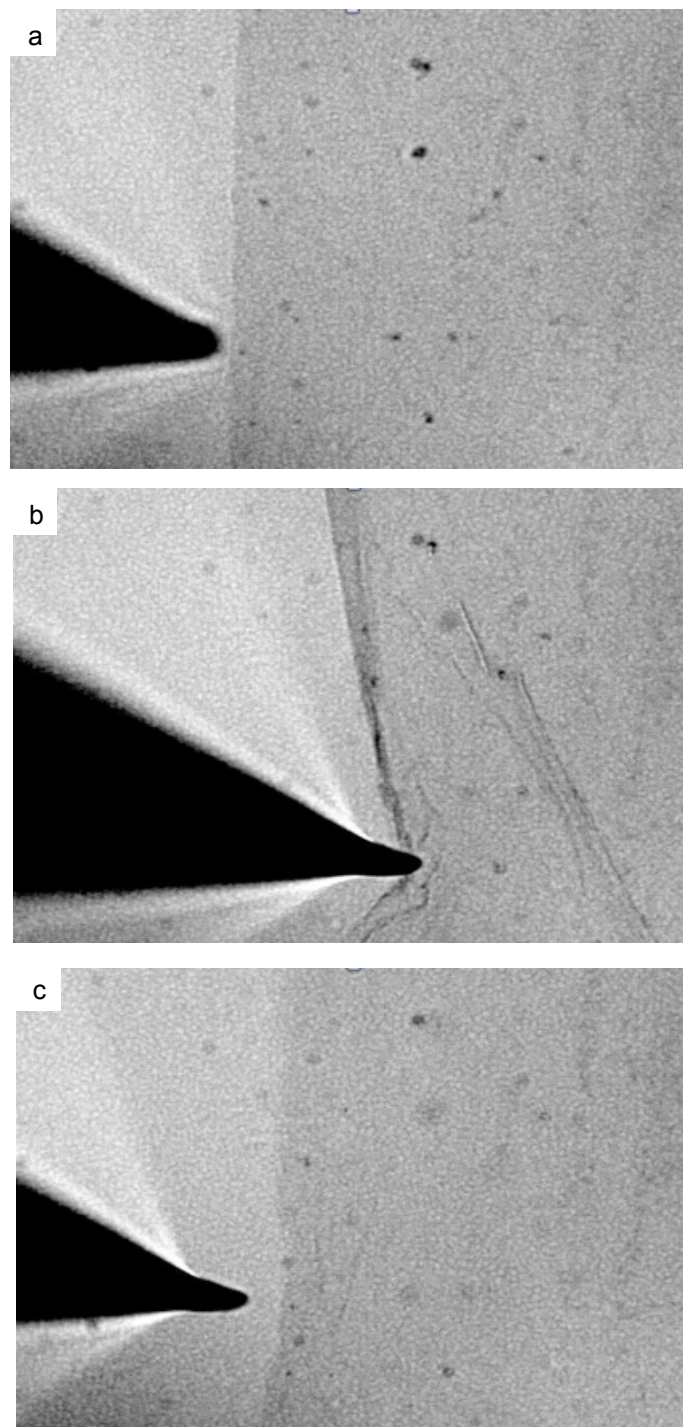


Fig. 3.3: Manipulating large sheets of graphene after the sacrificial layer etch. (a) A chip where the graphene was transferred on top of a layer of aluminum, which was then etched away to release the graphene from the surface. (b) The graphene sheet crumples like a large sheet of paper. (c) When released, it returns almost entirely to its original structure. Scale bar $\sim 10 \mu\text{m}$. Note that videos corresponding to many of the figures in this thesis can be found on the McEuen group website.

3.4 Crumpling graphene with a laser

We now take a brief detour from micromanipulator-based techniques to mention that it is possible to manipulate large sheets of graphene with a laser (Fig. 3.4). This method is much less controlled and not fully understood, but it suggests interesting physics for future study, and may be useful for other experiments.

We used a 1064-nm laser at a power of ~300 mW. As we will see Chapter 6, not all of this light (~20%) reaches the sample, but with the laser turned all the way up we still achieve significant power at the graphene surface. We use the LabVIEW program mentioned earlier to control the location of the laser spot. We can filter the light out of the image and simply “draw” with the cursor to move the laser spot across the field of view.

When we work with large, released graphene membranes and turn the laser up to the limits of its power, striking the graphene sometimes causes it to crumple and stick irreversibly to itself. As we might expect, this happens more easily near bilayer patches and contaminants, where the laser is more strongly absorbed. Once the graphene begins to crumple, the crumpled areas also become darker and the process accelerates.

It is not clear why this heating causes the graphene to crumple, but we can suggest some plausible mechanisms. As we heat the graphene—and by extension, the water—near the surface, we create areas of updraft in the water, or can even nucleate bubbles that tug upwards on the graphene. The laser might also be driving off or

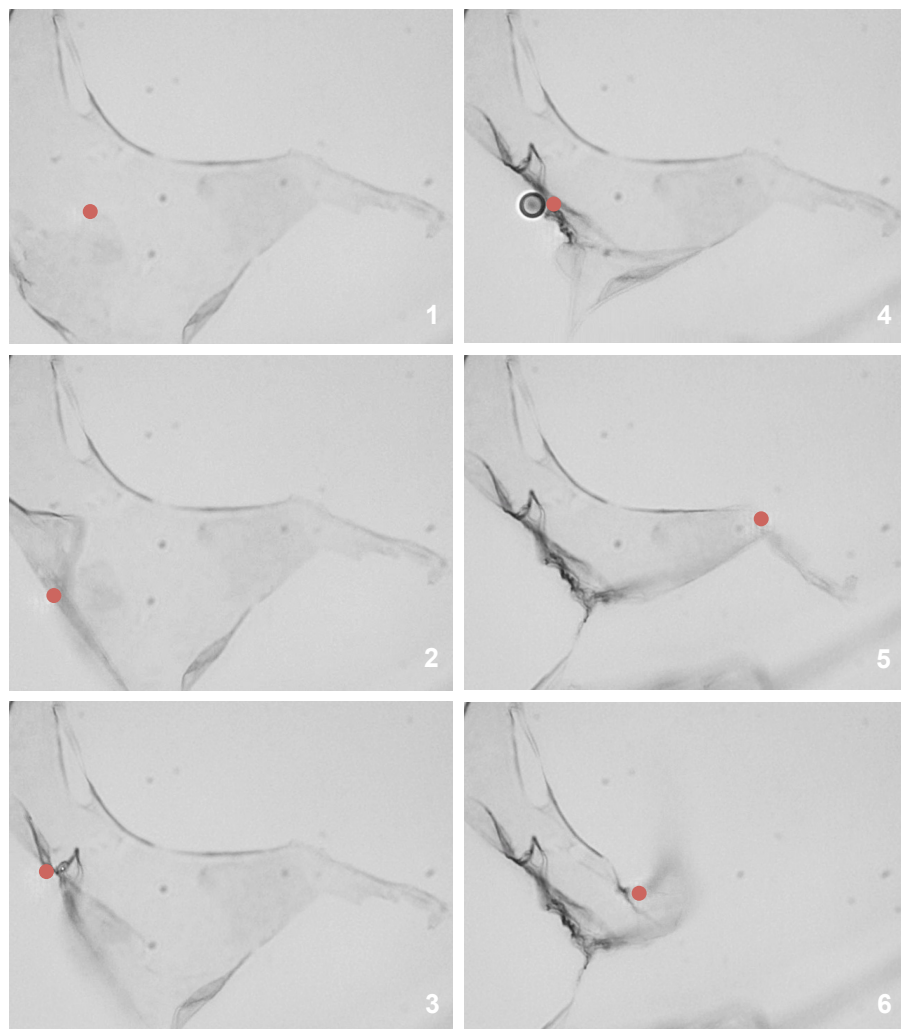


Fig. 3.4: Crumpling a large sheet of graphene with a laser. The red dot shows the location of the laser spot. Note the large bilayer regions on this graphene, and the small bubble that nucleates in frame 4.

burning off the surfactants, so that the graphene is free to stick to itself.

This laser technique provides another way to probe the system, and suggests that interesting surface physics may be happening between the graphene, the water, and the surfactants. By correctly patterning the starting membranes and adding a supporting framework, we may be able to use the laser to build and seal graphene envelopes. Such fluid-filled graphene capsules could be extremely useful for protein crystallography, where the envelope needs to be thin to be transparent to X-rays but still impermeable to water.²⁵

3.5 Moving and picking up graphene cantilevers

Besides pushing on the graphene directly with a probe or remotely with a laser, we can also manipulate it by holding on to attached gold handles. In this section we will pick up graphene cantilevers with gold pads on either end, and in Chapter 5 we will use them to measure the bending stiffness of graphene.

In Fig. 3.5 we drive the probe tip into the gold pad of a rectangular graphene cantilever device, mechanically deforming the gold and sticking the pad to the probe tip. Pushing forward crumples the graphene device; pulling back uncrumples the device and releases the right-hand gold pad from the surface. We can even lift the device entirely up off of the surface and out of focus. We have picked up devices up to $65\ \mu\text{m} \times 65\ \mu\text{m}$ in size using long gold handles, and even larger devices should be possible.

To release the device from the probe, we simply drive it up through the

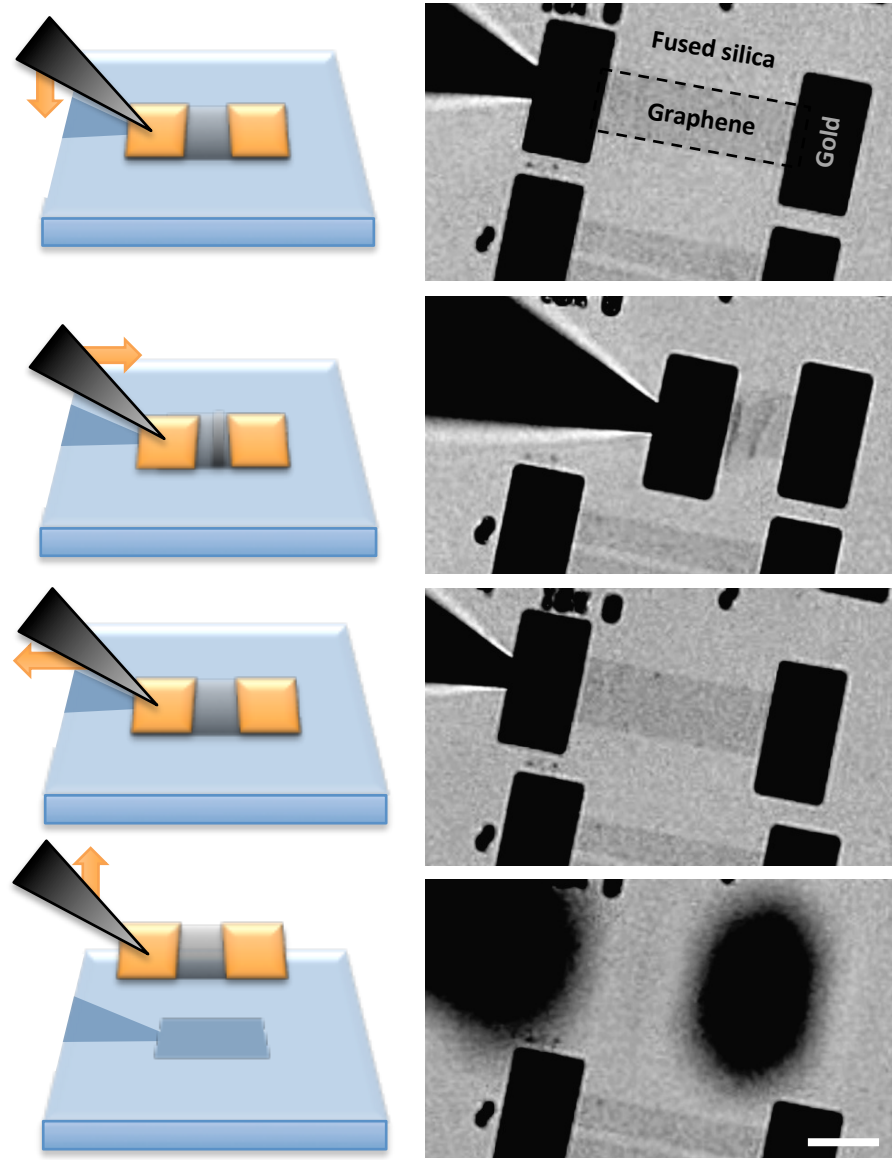


Fig. 3.5: Manipulating devices by using the gold pads as handles. From top: crumpling, uncrumpling, and lifting the device. Scale bar is 10 μm .

water/air interface, where the water meniscus pulls the device off of the probe tip.

We have found that once a device has been released from the surface, it never completely sticks down again. It seems to “float” on a thin layer of water, so that slightly bumping the optical table causes it to slosh back and forth. Adhesion effects are beyond the scope of this thesis, but suggest that interesting interfacial physics may be waiting to be explored in this environment.

3.6 Spirals from graphene

A spiral can be thought of as a very long cantilever patterned to fit into a small area. In Fig. 3.6(b) we show a graphene spiral sitting on the substrate; the ends are capped with small and large gold pads.

By driving the probe tip into the central gold pad, we can peel this long cantilever up off of the surface. Figs. 3.6(b-c) shows stills of the peeling process, where the probe tip and most of the graphene is out of focus and we can watch the surface as the graphene peels up. Note that we are looking *down* the length of the graphene here, a very unusual geometry for graphene in an optical microscope.

If we pull the spiral up until it has almost completely detached from the surface, it creates a helix-like shape limited by the length of the shorter inner edge of the spiral. This shape is reminiscent of jellyfish arms, as in Fig. 3.7(a).

Note that the graphene goes out of focus when we lift it up out of plane. This objective has a short focal depth, and we can use that fact to create an image stack by

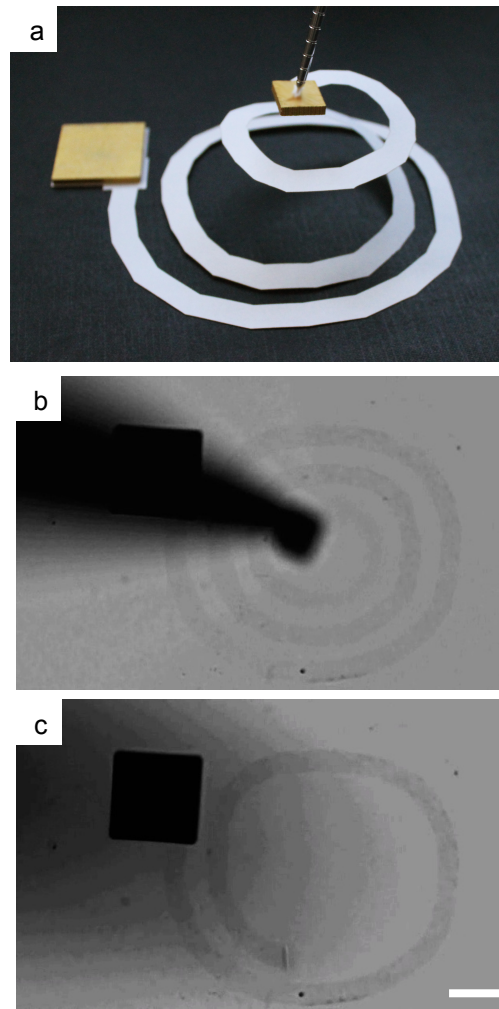


Fig. 3.6: A graphene spiral. (a) A paper model cut from the same CAD file. (b) Picking up the central pad with the probe tip. (c) We pull up to peel up the spiral. It disappears from view as it goes out of focus. Scale bar is $\sim 10 \mu\text{m}$.

scanning through different focus heights with the z -piezo on the objective.⁶⁸

The depth of focus of a microscope depends on the magnification and the numerical aperture (NA), where a higher NA means the light is focused in at a sharper angle. The depth of field is given by:⁶⁹

$$\text{depth of field} \approx \frac{\lambda n}{NA^2}$$

for a wavelength λ and index of refraction n . The objective we use for nearly all of the experiments in this thesis is a 40x air objective with a numerical aperture of 0.9. The index of refraction of water is $n=1.3$, so for visible light we should get a depth of field of between 300 nm and 1 μm . In practice, we find that we can resolve height differences of slightly less than 1 μm by eye.

We can use this shallow depth of field to create an image stack and get an idea of the three-dimensional structure of the spiral. Fig. 3.7(b) shows stills from this scan process, demonstrating how the shallow focal plane gives us three-dimensional information in the z -direction. The eye is remarkably good at translating an image stack into a three-dimensional structure, but as we will see in Chapter 5, there is also valuable quantitative information embedded in these z -scans. We can also add additional visual markers to the surface to improve our resolution — Fig. 3.7(c) shows a large sheet of graphene with SU-8 dots that provide detailed information about the 3D structure.

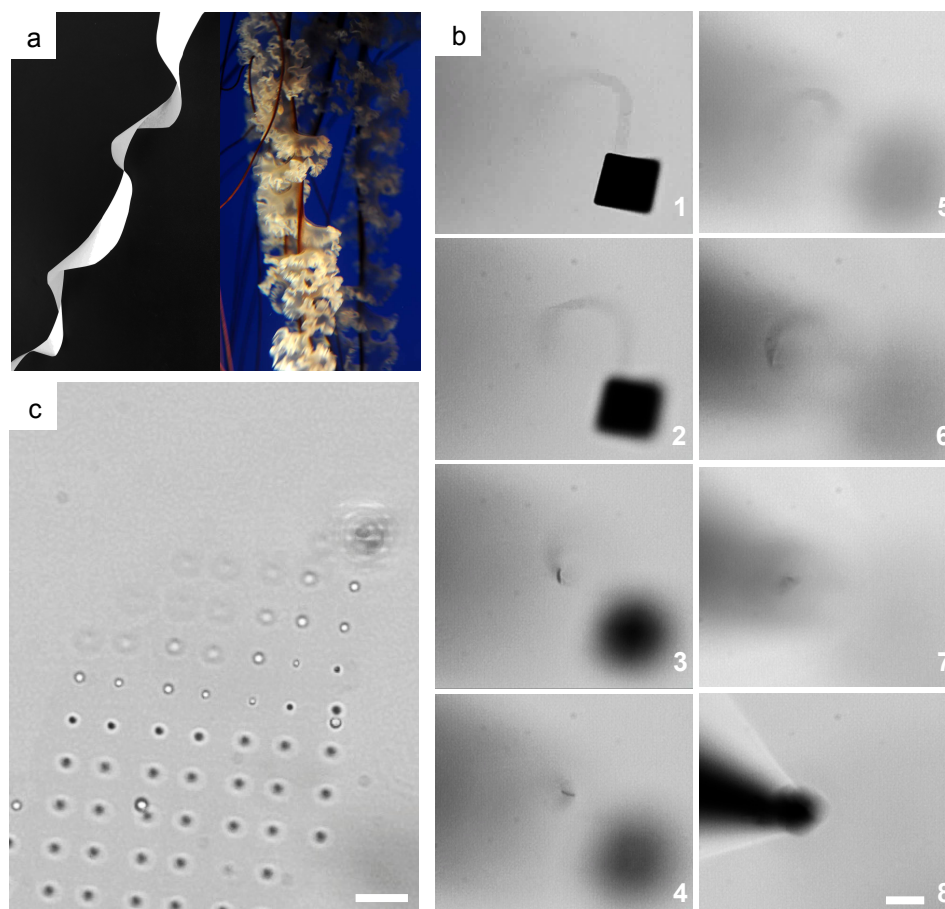


Fig. 3.7: Extended graphene spirals. (a) A paper model of a spiral that is held under tension creates a rippled structure, similar to the arms of some jellyfish (photo from baltimoresun.com). (b) By scanning the focus plane up through the spiral, we can extract information about its three-dimensional shape. (c) Three-dimensional information can be improved by adding visual tracking cues. For this large sheet of graphene, regularly-spaced SU-8 dots provide detailed 3D information about the structure of the sheet. Scale bars are $\sim 10 \mu\text{m}$.

3.7 Hinges from graphene

Once graphene is free from the surface, we can begin to use it to build functional structures. In Figs. 3.8 and 3.9 we show a simple sheet hinge made from a small $1\ \mu\text{m}\times 10\ \mu\text{m}$ piece of graphene. We can open and close the hinge by pushing and pulling on it using another, longer strip of graphene that extends to another gold pad “handle” (a gold pad like those described in Chapter 2). We loop this graphene arm (out of focus in the image) over the hinge and set it down again, so that moving the probe along the surface opens and closes the hinge. Note that this is an example of linked graphene elements moving one another, and that different types of motions, such as the opening and closing motion of the hinge, can be easily created from a flat sheet.

Despite being only one atom thick, this hinge is remarkably resilient. These hinges can survive more than 10,000 open-and-close cycles, at which point the gold pads start to warp (Fig. 3.9 (b-c)) This is a vivid illustration of graphene’s robustness, but it should not be surprising; to the graphene, which is just one atom thick, bending to a radius of $0.5\ \mu\text{m}$ is insignificant. Carbon nanotubes can be thought of as bent graphene sheets, and they have been found with radii down to $2\ \text{\AA}$.⁷⁰ A monolayer graphene hinge is ideal for microscale moving parts: it is extremely robust and could be scaled down to just tens of nanometers in size.

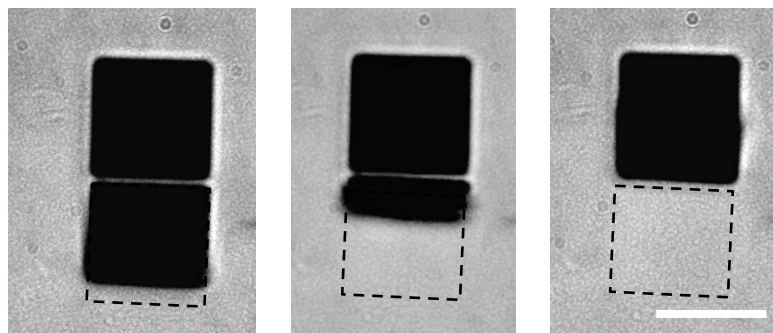
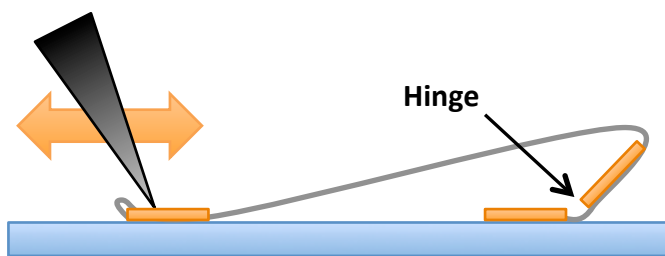


Fig. 3.8: A monolayer graphene hinge actuated with a long graphene arm. The stills, from left to right, show the hinge closing. These stills were taken after opening and closing the hinge 1,000 times. Scale bar is 10 μm .

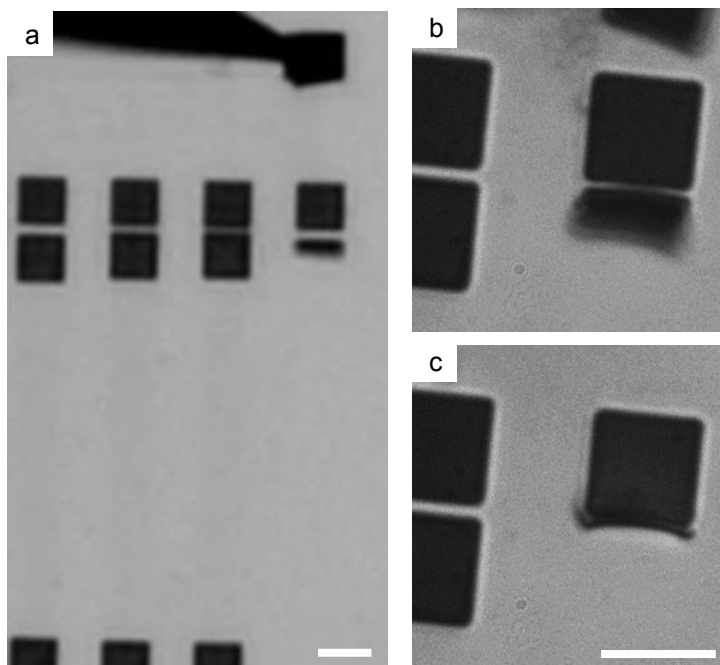


Fig. 3.9: (a) Zoomed-out image of a hinge, showing the probe and gold pad handle. The graphene strip looped over the top is out of focus. (b-c) Closing a hinge after 10,000 cycles. Note the gold pads have begun to warp, and that the long graphene handle is partially crumpled. Scale bars are 10 μm .

3.8 Conclusions

The development of the aluminum release method has allowed us to directly interact with free graphene membranes. We have demonstrated large-sheet crumpling and uncrumpling, and discussed a more controlled manipulation technique where patterned gold pads act as rigid handles. We used these techniques to build a simple three-dimensional spiral structure from this two-dimensional material, and to demonstrate amazingly robust sheet hinges from monolayer graphene. These hinges represent a simple way of turning a two-dimensional material and a linear motion into a different kind of motion—opening and closing—and suggest that creative patterning and design choices might lead to different kinds of moving parts.

These hinges are interesting from an engineering perspective, but they also raise an intriguing question about the fundamental mechanics of the graphene: how much energy does it take to open and close these hinges? Just how stiff is the graphene out of plane? The cantilevers described above conveniently provide an environment for measuring this fundamental mechanical property, one that has never been conclusively measured at the micron scale. This is the question we will set out to answer in the next two chapters.

CHAPTER 4

THE MECHANICS OF TWO-DIMENSIONAL CRYSTALLINE MEMBRANES

4.1 Introduction

We have now developed a technique for manipulating graphene in three dimensions, lifting it free from a surface. One of the advantages of this technique is that it will allow us to measure the out-of-plane bending stiffness of graphene, a fundamental mechanical property that has not been conclusively measured at the micron scale. However, before tackling this experimentally in Chapter 5, we should first understand the mechanics of free two-dimensional crystalline membranes. In this chapter, we will particularly focus on the effects of thermal fluctuations, which are predicted to dramatically affect the mechanical properties of free membranes.

In this chapter we will outline the formal theory of thermally induced fluctuations, discuss modern refinements to the theory, and develop an experimentally practical form. We will attempt to develop a qualitative understanding of the effects of thermal fluctuations, and discuss specific predictions for graphene at the scale of our experimental devices.

4.2 Liquid and crystalline membranes

There are two broad classes of membranes: liquid membranes, where the constituent atoms or molecules are free to move laterally within the membrane, and

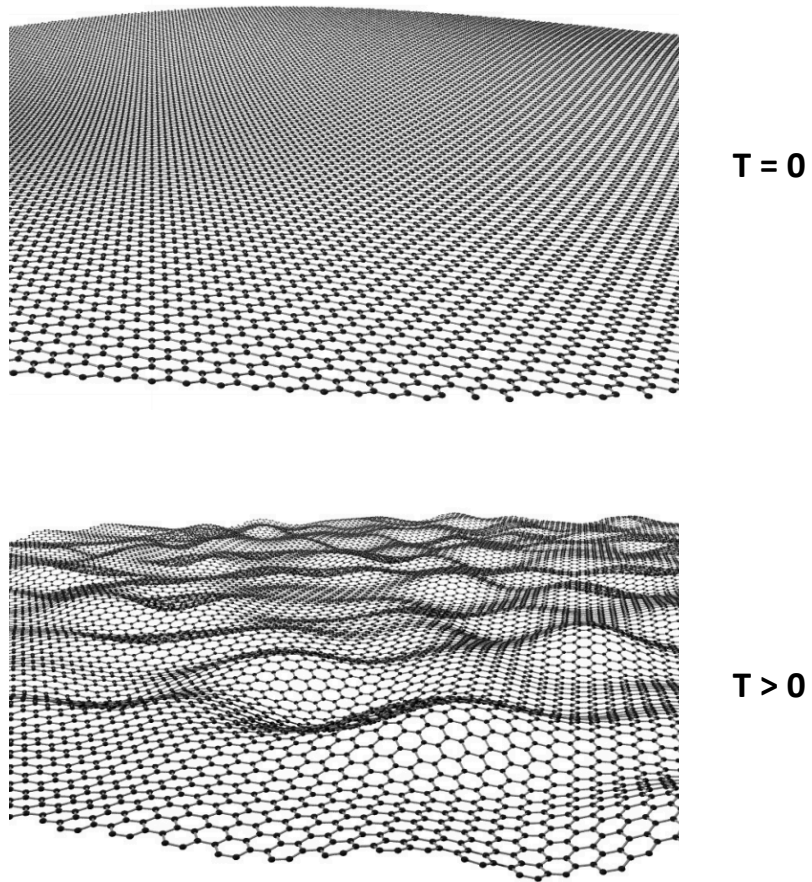


Fig. 4.1: Flat graphene at $T = 0$ and thermal fluctuations at $T > 0$. Figure from Meyer et al.

crystalline membranes such as graphene, where the atoms are held in place relative to their neighbors.

The elastic free energy of a two-dimensional membrane³⁵ is a sum of bending and stretching energies: $F_{tot}=F_b+F_s$:

$$F_{tot} = F_b + F_s \approx \frac{1}{2} \kappa \int d^2x (\nabla^2 f)^2 + \frac{1}{2} \int d^2x (2\mu u_{ij}^2 + \lambda u_{kk}^2)$$

where f is a function that gives the out-of-plane height, $z = f(x_1, x_2)$, and x_1 and x_2 are orthogonal directions on a reference plane (this is called the Monge form). The stretching energy term is a function of the strain matrix, which gives the energy cost of shearing and compressing the membrane in plane.⁷¹ The strain tensor $u_{ij} = \frac{1}{2}(\partial_i u_j + \partial_j u_i + \partial_i f \partial_j f)$, and in the stretching energy expression above, u_{ij} represents uniaxial deformations while u_{kk} represents isotropic deformations.⁷² The corresponding elastic constants are μ (the shear modulus) and λ (the first Lamé coefficient), and together they are called the Lamé coefficients, and are the equivalents of the spring constant in the 1D version of Hooke's law. Note that there is a coupling term hidden in the strain tensor: the last term (in f) couples the bending and stretching energies together in membranes with nonzero shear moduli.⁷³

Macroscale membranes should be flat, but in nanoscale materials we can expect significant effects from thermal fluctuations. At room temperature, thermal fluctuations will cause a nanoscale membrane to fluctuate out of plane, bending and stretching to create three-dimensional structure (Fig. 4.1). The simplest way to model a membrane is using the harmonic approximation, which ignores any coupling between the bending and stretching energies.⁷³

Liquid membranes have no shear modulus, and bending energy is the dominant element. Thermal fluctuations make these membranes fluctuate out of plane dramatically, so at room temperature they have no long-range order.^{74,75}

Crystalline membranes like graphene, however, have both bending and stretching energy. As we will see below, at larger size scales the two energies are coupled, and the harmonic approximation fails. This coupling stabilizes crystalline membranes, increasing their effective bending stiffness and giving them long-range order.³⁵ For the rest of this chapter we will focus on these crystalline membranes.

A simple way to characterize the mechanical behavior of crystalline membranes, and to compare the bending and stretching elements, is using the Foppl-von Karman (νK) number.^{76,77} It is given by the ratio of the two-dimensional Young's modulus Y_{2D} and the out-of-plane bending stiffness κ , scaled by the area of the membrane L^2 :

$$\nu K = \frac{Y_{2D} L^2}{\kappa}$$

A high νK number means the membrane more easily bends and crumples than stretches or shears.

For a three-dimensional material such as paper, the Foppl-von Karman number can be easily rewritten as a function of the aspect ratio of the sheet using $Y_{2D} = Y_{3D} t$ and $\kappa = Y_{3D} t^3 / 12(1 - \sigma^2)$:

$$\nu K = \frac{Y_{3D} t L^2}{Y_{3D} t^3 / 12(1 - \sigma^2)} = \frac{12(1 - \sigma^2) L^2}{t^2}$$

A sheet of typical 8.5×11-inch printer paper, for example, has a Poisson ratio⁷⁸ of 1/3 and a thickness of ~0.1 mm, so its νK number is 10^7 . For paper we can assume the

sheet is flat, but for nanoscale membranes like graphene, we must account for thermal fluctuations. As we will see below, these fluctuations have a significant effect on both the bending stiffness and the Young's modulus, strongly affecting the νK number.

4.3 The formal theory of thermally induced fluctuations in crystalline membranes

The foundational paper on fluctuations in crystalline membranes was written in 1987 by Nelson and Peliti.³⁵ Nelson and Peliti rewrite the free energy expression above to describe the stretching in terms of the out-of-plane height function f rather than the strain tensor elements. So the total free energy looks like:

$$F_b + F_s \approx \frac{1}{2} \kappa \int d^2x (\nabla^2 f)^2 + \frac{1}{2} K_0 \int d^2x \left(\frac{1}{2} P_{ij}^T \partial_i f \partial_j f \right)^2$$

for $P_{ij}^T = \delta_{ij} - \partial_i \partial_j / \nabla^2$, where δ_{ij} is the Kroneker delta. The Lamé coefficient was used here to simplify things by defining $K_0 \equiv \frac{4\mu(\mu+\lambda)}{2\mu+\lambda}$, an effective in-plane spring constant. For simplicity, we will convert it to the familiar 2D Young's modulus using the relationships⁷⁹ between the elastic moduli ($\lambda = \frac{\mu(Y-2\mu)}{(3\mu-Y)}$ and $\mu = \frac{Y}{(2(1-\sigma))}$), so that $K_0 = \frac{Y_{2D}}{1-\sigma^2}$.

Nelson and Peliti studied how thermal fluctuations affect the bending stiffness. They focused on the renormalized, wavenumber-dependent bending stiffness $\kappa_R(\mathbf{q})$, where $\kappa(\mathbf{q}) \equiv k_B T / q^4 \langle |\hat{f}(\mathbf{q})|^2 \rangle$ and $\hat{f}(\mathbf{q})$ is the fourier transform of $f(\mathbf{x})$. The first two terms in the perturbation series in the Young's modulus are:

$$\kappa_R(\mathbf{q}) = \kappa_0 + k_B T \frac{Y_{2D}}{1-\sigma^2} \int \frac{d^2k}{(2\pi)^2} \frac{[\hat{\mathbf{q}}_i P_{ij}(\mathbf{k}) \hat{\mathbf{q}}_j]^2}{\kappa_0 |\mathbf{q} + \mathbf{k}|^4}$$

where $P_{ij}(k) = \delta_{ij} - k_i k_j / k^2$ and $\hat{\mathbf{q}}_i$ is a unit vector. Note that the terms are additive,

so the bending stiffness will always be stiffer than κ_0 . Compare this to the correction for a liquid membrane, where $\kappa_R(\mathbf{q}) = \kappa_0 - \frac{3k_B T}{4\pi} \ln\left(\frac{1}{qa}\right)$ and the membrane correspondingly *softens*.⁷⁴

For long-wavelength fluctuations, and assuming no renormalization of the elastic constants, Nelson and Peliti make an educated guess at the form of the renormalized bending stiffness:

$$\kappa_R(\mathbf{q}) \sim \sqrt{\frac{k_B T Y_{2D}}{1-\sigma^2}} q^{-1}$$

They are clear that they did not renormalize Y_{2D} here—they assumed that none of the in-plane elastic constants change. Later papers in this field set out to avoid this assumption using a variety of computational and mathematical methods, as we now discuss.

Intuitively, we might expect that stretching a rippled membrane will be easier because we can easily pull out the fluctuations. A lowered value of the Young's modulus should partially counteract the stiffening effects of thermally induced fluctuations, lowering Nelson and Peliti's estimate for the effective bending stiffness. Many researchers have tackled this problem since the late 1980s. Aronovitz and Lubensky,⁸⁰ Le Doussal and Radzihovsky,⁸¹ Knownacki and Mouhanna,⁸² and Braghin and Hassleman⁸³ all use different approaches to calculate the effective bending stiffness, $\kappa_R(\mathbf{q})$, without holding Y_{2D} constant. They end up with elastic moduli that depend on the wavenumber of the fluctuation with a scaling favor η on the wavevector dependence:

$$\kappa_R(\mathbf{q}) \propto q^{-\eta}$$

where for Nelson and Peliti, $\eta = 1$. The value of η in the later papers varies depending on their approach, but seems to be narrowing in on about $\eta = 0.85$.^{84,46,83,72}

4.4 Deviations from the harmonic model: the crossover length

Fig. 4.2 shows the correlation function for the out-of-plane displacements of the membrane as a function of the wavenumber, adapted from Roldan et al.⁸⁵ The vertical axis is the correlation function for the out-of-plane displacements, equal to the mean square amplitude of the out-of-plane displacement, $G(\mathbf{q}) \equiv \langle |h(\mathbf{q})|^2 \rangle$; a higher value of $G(\mathbf{q})$ corresponds to larger out-of-plane fluctuations. If the correlation function stays finite, the system has long-range order and it does not crumple up.^{35,80} On the graph, the dashed blue line shows the harmonic approximation (i.e. the stretching and bending energies are uncoupled), where $\langle |h(\mathbf{q})|^2 \rangle = k_B T / \kappa q^4$.

The solid red line shows the complete thermal fluctuation theory described above, where bending and stretching are coupled. At large wavenumbers the two models match, but as we move towards smaller wavenumbers the curves diverge. So at very small scales (large q) the coupling between the bending and stretching energy has an insignificant effect, but at larger scales it significantly stiffens the membrane and reduces the amplitude of the out-of-plane fluctuations.

We can see that there is some critical size scale above which the effects of thermal fluctuations become significant. In the language of wavenumbers this is the Ginzburg criterion, given by⁸⁵

$$q_c = \sqrt{\frac{3k_B T Y_{2D}}{8\pi\kappa_0^2}}$$

which is shown on the plot as a dashed vertical line. Converted to wavelengths, this expression gives a crossover length:

$$l_c = \sqrt{\frac{32\pi^3\kappa_0^2}{3k_B T Y_{2D}}}$$

that depends only on the intrinsic properties of the material. This is the size scale above which the effects of thermal fluctuations begin to dominate.

We can write a simple, experimentally practical form for the fluctuation-dependent renormalized bending stiffness. We can combine Nelson and Peliti's expression for the renormalized bending stiffness with the crossover length to get a prediction for the bending stiffness due to thermal fluctuations. Converting to wavelengths l and bringing in the corrected scaling exponent η , we have:

$$\kappa_{eff} = A \kappa_0 \left(\frac{l}{l_c}\right)^\eta$$

where A is a numerical prefactor. Note that the stiffness is size-dependent—larger membranes can hold longer-wavelength fluctuations, so they will be stiffer. We will focus on the longest-wavelength fluctuations in a finite-sized membrane, since it should create the dominant out-of-plane fluctuations. (In comparing this theory to experimental results in the next chapter, the relevant size will be the width W of the cantilevers, since ripples along W will be what stiffens the cantilevers.)

As mentioned earlier, the in-plane elastic properties also change under the effects of thermal fluctuations, so we must adjust Y_{2D} as well. Aronovitz and Lubensky⁸⁰ first addressed the renormalization of the in-plane elastic constants, finding a scaling factor for the elastic constants in a 2D membrane of $\eta_u = 2 - 2\eta$.

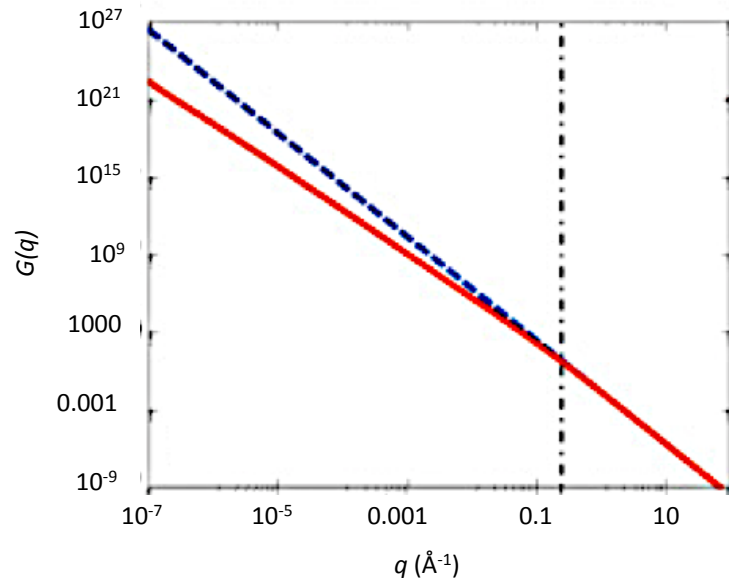


Fig. 4.2: Plot from Roldan et al., Phys. Rev. B (2011), showing the correlation function versus wavenumber for the harmonic approximation (dashed blue curve) and for the thermal fluctuation theory which takes into account the coupling between bending and stretching (solid red curve). The vertical dashed line shows the Ginzberg scale, where the two models begin to diverge.

We can write the renormalized Young’s modulus in the same form as the renormalized bending stiffness, though it should scale inversely with l (larger fluctuations lower the Young’s modulus).⁸⁶ So for another numerical prefactor B , we have:

$$Y_{eff} = BY_0 \left(\frac{l_c}{l} \right)^{\eta_u}$$

4.5 An intuitive understanding of the stiffening effects of thermal fluctuation

We will now take a moment to develop a physical intuition for the effects of fluctuations. We can see the effects of coupling between bending and stretching energies by playing with a sheet of paper. Paper has a high aspect ratio and is much easier to bend than to stretch, so it provides a good macroscale analog to crystalline membranes.

A flat sheet of paper is easy to bend out of plane, but adding crumples or corrugations make it much stiffer (Fig. 4.3). This is the principle behind corrugated cardboard. The simplest way to think of this is as a classical beam, where we have increased the thickness t and thus increased the bending stiffness. On a qualitative level, we can think of thermal fluctuations in a crystalline membrane the same way—they create a thicker “effective membrane.”

More precisely, consider the fact that some distortions of a two-dimensional membrane require you to fold the membrane while others require you to fold *and stretch* it. Fig. 4.4 shows different ways of distorting a membrane. We can characterize different kinds of distortions by their Gaussian curvature. The saddle shape has a

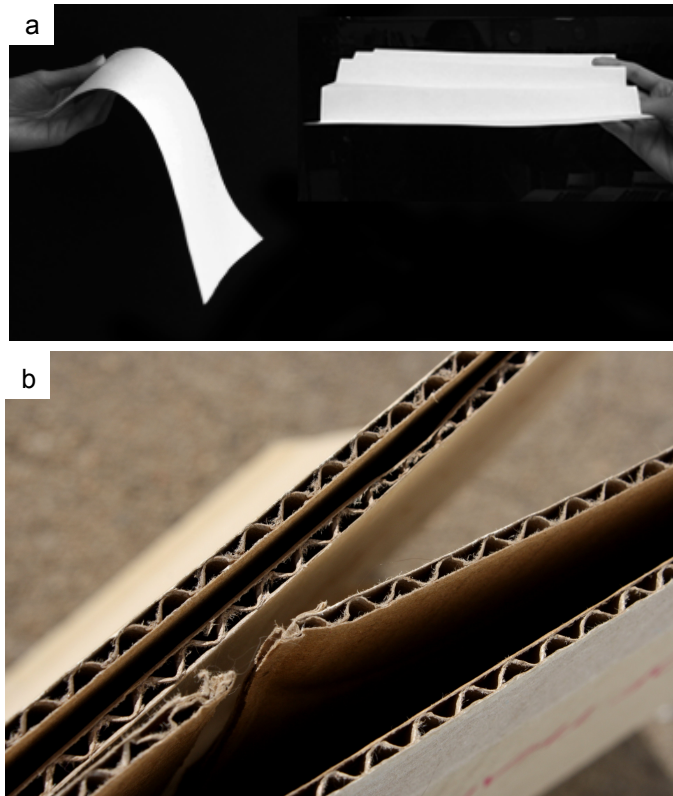


Fig. 4.3: Effective thickening of a membrane. (a) A flat sheet of paper is significantly easier to bend than a sheet with creases. (b) Corrugated cardboard.

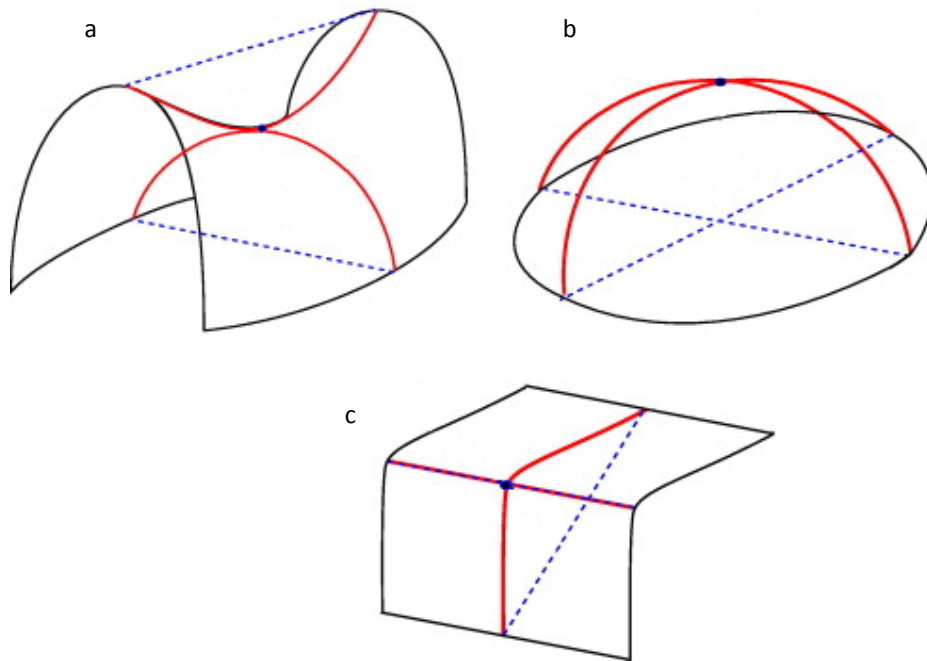


Fig. 4.4: Types of Gaussian curvature. (a) Saddle shape, $S < 0$, (b) bubble shape, $S > 0$, and (c) simple fold, $S = 0$.

Gaussian curvature $S < 0$, the bubble has $S > 0$, and the simple fold has $S = 0$. The first two cases require significant stretching of the membrane, but the simple fold does not. As you can immediately see by playing with a sheet of paper, bending in one direction is easy (it costs bending energy only), but bending in two simultaneous directions cost both bending and stretching energy, and is much more difficult. In both paper and crystalline membranes, stretching energy is orders of magnitude higher than the intrinsic bending energy, so this is a dramatic effect. If we have a membrane with ripples along \mathbf{x}_1 (a zero Gaussian curvature distortion), then bending it along \mathbf{x}_2 requires us to create an energetically expensive saddle or bubble shape (a nonzero Gaussian curvature distortion). The ripples in \mathbf{x}_1 have effectively stiffened the membrane in the \mathbf{x}_2 direction.

Going back to the formal theory, the Gaussian curvature is implicitly included in the free energy expression as:⁷⁵

$$S(\mathbf{x}) = -\nabla^2 \left(\frac{1}{2} P_{ij}^T \partial_i f \partial_j f \right)$$

The areas in the membrane with non-zero Gaussian curvature contribute to the stretching energy.³⁵

4.6 Applications to Graphene

At the atomic scale, graphene has a low atomic-scale bending stiffness, $\kappa_0 = 1.2 \text{ eV}$,^{34,32} and an extraordinarily high Young's modulus of $Y_{2D} = 340 \text{ N/m}$.²⁸ These values give a crossover length of $l_c \approx 3 \text{ nm}$ at room temperature.⁸⁵ At smaller scales than that the intrinsic bending stiffness should be fairly accurate, but at larger

scales the effect of thermally induced fluctuations will dominate. Thermal fluctuations should have a significant effect at all of the size scales we probe in this thesis, and at all size scales where experimentalists typically work. In fact, graphene's combination of low intrinsic stiffness and high in-plane strength makes it an ideal model material for the experimental study of thermal fluctuation theory.

We can see the dramatic effect of the renormalized bending stiffness by how it affects the νK number of graphene. If we naively used graphene's bending stiffness at the atomic scale, $\kappa = 1.2 \text{ eV}$, we might predict a νK number for a $10 \text{ }\mu\text{m} \times 10 \text{ }\mu\text{m}$ sheet of graphene of $\nu K \sim 10^{11}$, *dramatically* softer than a sheet of standard paper. But qualitatively, this is not what we saw when we manipulated large sheets of graphene in Chapter 3. Rather, graphene at the $10\text{-}\mu\text{m}$ scale seems to behave a lot like paper.

We can calculate the corrected νK number using the renormalized stiffness and in-plane elastic constants, so that

$$\nu K_{eff} = \frac{Y_{2D\text{ eff}} L^2}{\kappa_{eff}}$$

We simply write the renormalized νK in terms of the expressions for the renormalized values (dropping the numerical prefactors):

$$\begin{aligned} \nu K_{eff} &= \frac{B Y_0 \left(\frac{l_c}{l}\right)^{\eta_u}}{A \kappa_0 \left(\frac{l}{l_c}\right)^\eta} L^2 \\ &= \left(\frac{Y_0 L^2}{\kappa_0}\right) \left(\frac{l_c}{l}\right)^{\eta+\eta_u} \\ \nu K_{eff} &= \nu K_0 \left(\frac{l_c}{l}\right)^{\eta+\eta_u} \end{aligned}$$

which for a 10- μm \times 10- μm sheet of graphene gives:

$$\nu K_{eff} = (10^{11}) \left(\frac{3 \text{ nm}}{10 \mu\text{m}} \right)^{0.85+0.3} = 10^7$$

matching the νK number of a sheet of paper.

The νK number gives a quantitative comparison between an atomic membrane and a macroscale sheet of paper. It is a useful measure of the size-dependent behavior of a membrane, and it captures the key factor that will affect kirigami.

4.7 Conclusions

Theorists have extensively studied thermal fluctuation theory over the last four decades, but experimental confirmation has mostly been out of reach.⁸⁷ Graphene provides an ideal laboratory for these membrane mechanics studies, because its high stretching energy and low intrinsic bending energy mean that the effects of thermally induced fluctuations are particularly dramatic. In the next chapter, we will perform a direct measurement of the bending stiffness of graphene for the first time, providing the first evidence for the effects of thermal fluctuations on bending stiffness.

CHAPTER 5

MEASURING THE BENDING STIFFNESS OF GRAPHENE

5.1 Introduction

As we described in Chapter 4, the stiffness of unstrained membranes should be dramatically affected by thermal fluctuations. However, attempts to measure this basic mechanical quantity have given widely varying results,^{45,88} and so far it has not been conclusively measured at the micron scale. Due to experimental constraints, most of the experimental work on graphene's mechanical properties in the last decade has focused on suspended graphene under strain.^{89,38,28} As we saw in Chapter 1, researchers have build a variety of fully-clamped and doubly-clamped beams. These suspended devices have allowed researchers to measure the in-plane mechanical properties of graphene, but the effects of the out-of-plane bending stiffness are usually washed out when strain dominates.

The manipulation methods we have developed so far in this thesis allow us to lift graphene cantilevers off of a substrate in a novel *unstrained* geometry. This chapter describes how we use this technique to perform a direct measurement of the spring constants of monolayer graphene cantilevers. We use two methods, one based on the force of gravity and the other on thermal motion. In this chapter we describe these measurement techniques, show representative data, and perform the simple analysis of the spring constant data to extract a value for the bending stiffness of graphene. Finally, we compare the results to the predictions of thermal fluctuation theory from the last chapter.

5.2 Using gravity to measure spring constants

To measure the spring constant of a graphene cantilever, we can simply apply a known force to end and treat it like a simple spring. We use the gold pad on the end of the graphene cantilever from Chapters 3 as weights, and watch the devices bend under the force of gravity. The spring constant is given by $F = k\Delta z$, where the force of gravity F creates a deflection Δz in a device with spring constant k . (Note the notation: k is the spring constant of a device and κ is the bending stiffness of a material.)

We fabricated graphene devices of different sizes using the techniques described in Chapter 2. A finished device, lifted up off the surface and deflected under gravity, is shown in Fig. 5.1(a).

Fig. 5.1(b) shows a cartoon of the graphene cantilever device. We can measure the height difference between the two pads because they sit in different focal planes. We use the z -piezo stage on the microscope objective, as in Chapter 3. We define the height difference between the inner edges of the two pads as Δz , and determine when the inner edges of the pads are in focus by eye. For each device, we take three measurements of the height difference, and average to reduce the error. Representative raw data for the device in Fig. 5.1 are shown in Table 5.1. We read these numbers straight off of the z -piezo controller and wrote them down by hand, and also used LabVIEW to record the z -piezo height along with the video data. Arthur Barnard later applied an edge-finding algorithm to this data and used a planar fit to create a three-

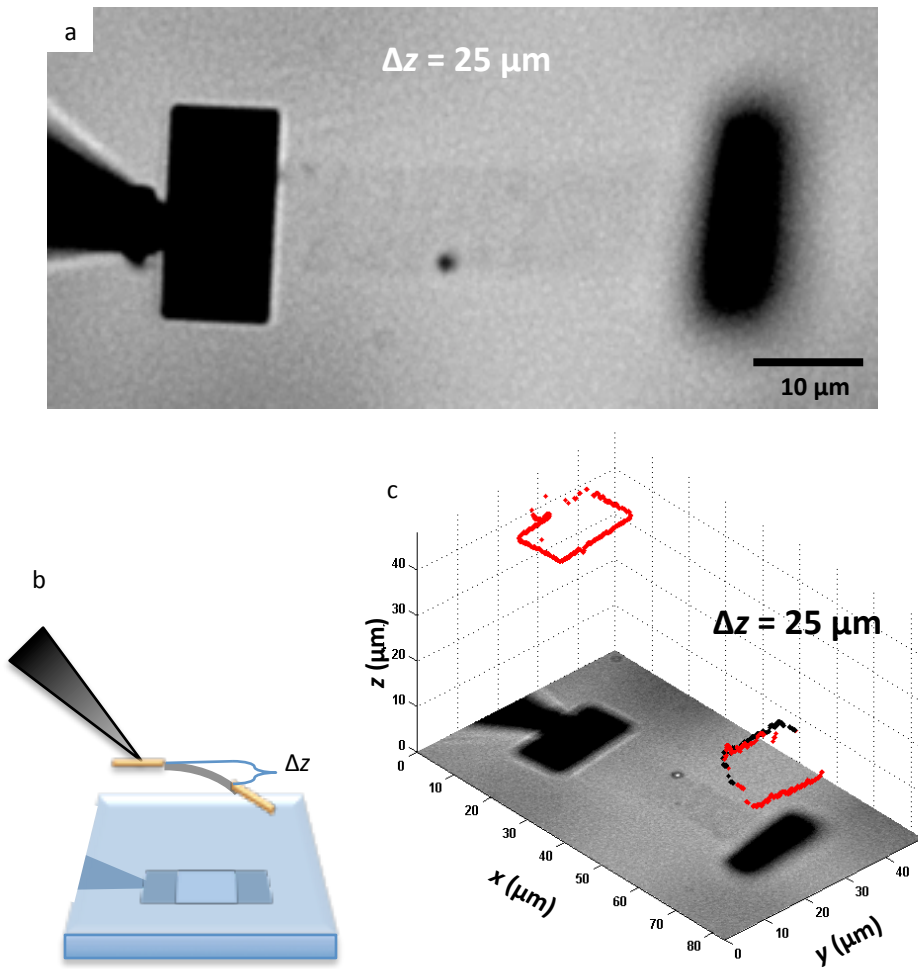


Fig. 5.1: Picking up a 50- μm -long device. (a) Optical image. The pads are in different focal planes. We use the z-piezo on the objective to measure the height difference between the inner edges of the two pads, Δz . (b) A cartoon of the geometry. The image is taken from below. (c) 3D reconstruction of the location of the pads, courtesy of Arthur Barnard.

dimensional reconstruction of the pads (Fig. 5.1(c)). We find that the resulting value of Δz closely matches the data we took by eye. One advantage of this reconstruction is that it lets us check the orientation of the pads. If the probe tip grabs the gold pad at an angle the whole device could be tilted, and it would give us an incorrect value for the height difference. Luckily, the reconstruction shows that the pad stays parallel to the surface in this case, and in cases where the pad was significantly tilted, we found that we could tell by eye.

We took data for devices from a variety of chips and different fabrication runs. We discarded devices that were obviously torn, dirty, or visibly crumpled once we picked them up off the substrate. Any data sets with visibly tilted pads were also discarded. All devices have a width $W=10\ \mu\text{m}$, but the lengths vary from $L=20\ \mu\text{m}$ to $L=75\ \mu\text{m}$.

5.3 Analysis of the gravity data

Our 40x, 0.9 NA microscope objective is designed for working in air. However, the light must travel through air, the fused silica substrate, and into the water, refracting at each boundary and distorting our height measurements. It turns out that the fused silica substrate only causes an overall offset in the absolute measured vertical position of a target object, but that the index of refraction of the water distorts the vertical *height difference* between two points. Since we are looking at a difference in pad heights, we can ignore the overall offset, but we must still account for the size

#	Left pad	Right pad	Difference
1	41.32 μm	59.95 μm	18.63 μm
2	41.32	60.20	18.88
3	40.83	62.16	21.33
Average difference:			19.6 μm
Corrected for n ($ave*1.3$):			25 μm
Spring constant k:			7×10^{-8} N/m

Table 5.1: Rows 1-3: Raw data from the device in Fig.1, size $10 \mu\text{m} \times 50 \mu\text{m}$; the gold pads are $10 \mu\text{m} \times 20 \mu\text{m} \times 50 \text{nm}$. The values come directly from the display on the z -piezo controller. The bottom two rows give the average height difference and the corrected value after adjusting for the index of refraction of water.

distortion. The correction is given by:⁹⁰

$$\frac{n_2}{n_1} \times \text{measured height difference} = \text{actual height difference}$$

for the index of refraction of the device's environment n_2 and index of refraction of the objective's environment n_1 . Water's index of refraction⁹⁰ $n_2=1.3$, and our lens is a standard air objective, so $n_1=1$. So we simply multiply the measured height difference by a factor of 1.3, as shown in the last row of Table 5.1.

To confirm the piezo calibration, we checked it against the focus dial on the microscope. The focus dial was in turn confirmed by measuring the focus difference between the top and bottom of a number of cover slips and checking that the value matched specs when corrected for the index of refraction of fused silica,⁹¹ $n=1.5$.

To extract the spring constant from the height difference, we need to know the force of gravity on the gold pads. This is given by $F_g = m_{gold}g$ for the mass m_{gold} of the pads, and we must also correct for the buoyancy due to the displaced water,

$F_{buoyant} = m_{displaced\ fluid}g$. So:

$$k = \frac{F_g - F_{buoyant}}{x_g} = \frac{m_{gold}g - m_{fluid}g}{x_g} = \frac{(\rho_{gold} - \rho_{fluid})LWtg}{x_g}$$

for gold pads of thickness t and size $L \times W$. The density of gold $\rho_{gold} = 19.3 \text{ g/cm}^3$ and $\rho_{water} = 1.0 \text{ g/cm}^3$. For our sample data in Table 1, we get:

$$\begin{aligned} k &= \frac{(19.3 \frac{\text{g}}{\text{cm}^3} - 1 \frac{\text{g}}{\text{cm}^3})(10\mu\text{m})(20\mu\text{m})(50\text{nm})(9.8 \frac{\text{m}}{\text{s}^2})}{25 \mu\text{m}} \\ &= 7 \times 10^{-8} \text{ N/m} \end{aligned}$$

Data for all gravitational measurements are shown on the plot in Fig. 5.4 as blue dots, where the spring constant k is plotted against the device length L . The spring constants decrease dramatically with increasing length; unsurprisingly, longer cantilevers are softer.

5.4 Thermal measurements of spring constants

A second way to measure the spring constant of a graphene cantilever is to watch the pad's thermal motion. To extract a spring constant from the thermal fluctuation data, we treat the device like an overdamped oscillator exploring a harmonic potential of energy $E = \frac{1}{2}kx^2$. The cantilever moves randomly as the water molecules bump into it; over time, it will random-walk through its harmonic potential. By the equipartition theorem, each degree of freedom of the pad should have an average kinetic energy $\langle E \rangle = \frac{1}{2}k_B T$. For the time-averaged square (the variance) of the fluctuation amplitude $\langle x_{th}^2 \rangle$, the spring constant becomes^{92,93} $k = \frac{k_B T}{\langle x_{th}^2 \rangle}$. This is a common technique for measuring spring constants of AFM tips, and the Brownian motion of microbeads is often used to calibrate optical traps.^{94,95}

We attached a stepper motor to the arm of the micromanipulator to rotate the devices, allowing us to image the pad edge-on and watch its motion in the higher-resolution x - y plane. See Fig. 5.2(a) for a schematic. We note that the rotation can be rough on the devices. The device is dragged through the water during the rotation, and

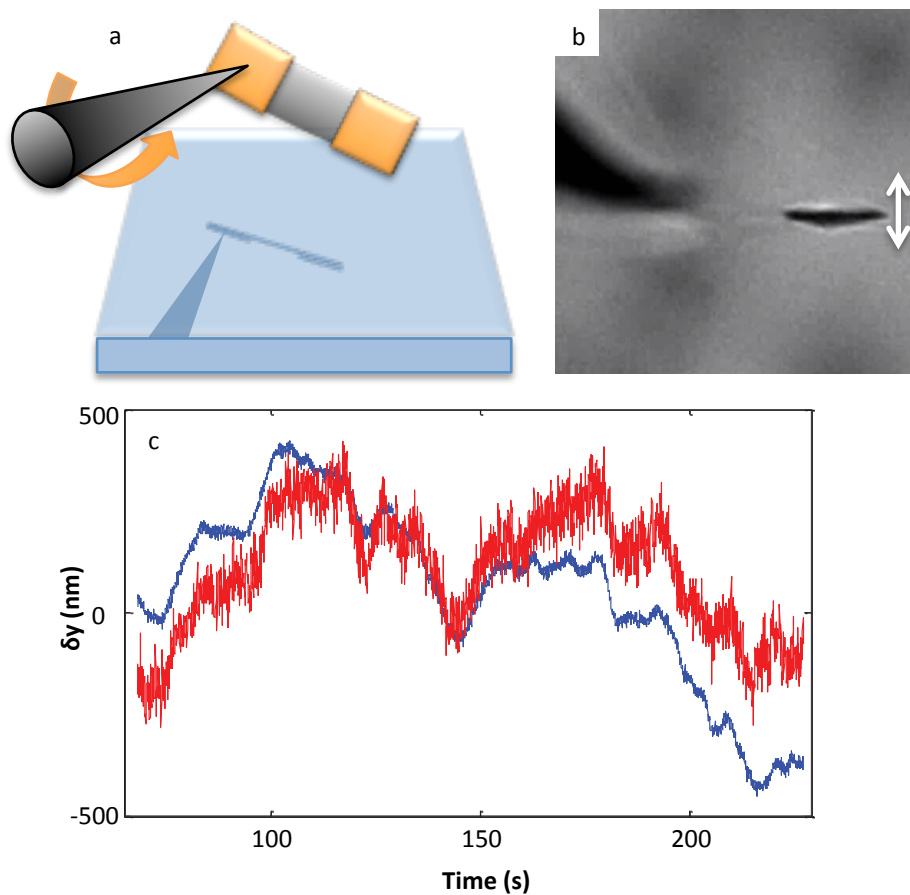


Fig. 5.2: Tracking the thermal motion. (a) A cartoon of the device after rotation. Data is collected by looking up through the substrate. (b) Optical image of the rotated device. (c) Time trace showing the location of the PatchStar probe tip (blue) and the far pad (red). The image has been thresholded to find the center of both objects. The frame rate is 23 fps, size scale is 182 nm/pixel. The long-timescale motion is dominated by the probe drift, but the difference in width of the lines shows the faster thermal motion of the device.

sometimes folds up on itself and has to be discarded. In many cases, the device rotates slightly around the point where it contacts the probe, so that the device is still visible edge-on but the far pad hangs significantly lower.

Once the device is rotated edge-on, we turn off the power to the stepper motor and the PatchStar to prevent motor vibration. We record video for 5-10 minutes for each device, at a frame rate of ~ 23 frames per second.

We repeated these measurements for many devices. All devices have a width $W=10\ \mu\text{m}$, but the lengths vary from $L=8\ \mu\text{m}$ to $L=30\ \mu\text{m}$.

5.5 Thermal data analysis

To extract an accurate value of the variance, $\langle x_{th}^2 \rangle$, Samantha Roberts and Arthur Barnard in our group have developed MATLAB code to accurately analyze the video data, and to deal with the challenges of manipulator drift.^{96,97} They used a centroid-finding algorithm and tracked the motion of the pad over time, as well as the motion of the probe tip (Fig. 5.2(c)). We see identical slow, large-amplitude motion from the PatchStar for both the right-hand pad (red) and the probe tip (blue); this is device moving across the field of view as the PatchStar drifts. However, the right-hand pad also oscillates on a short timescale. This short-timescale oscillation is the thermal motion of the pad.

We can estimate the expected time scale of the thermal motion.⁹⁸ We treat the pad like a sphere in water, and estimate how long it will take to diffuse over 50 nm.

The diffusion constant D of a sphere of radius r moving through a medium with viscosity η is given by

$$D = \frac{k_B T}{6\pi\eta r}$$

However, the gold pad is not a sphere. Instead, we treat the pad like a spherical bead with an effective radius that is calculated by $r_{sphere} = (3/2\rho)^{1/3}r_{disk}$, where r_{disk} is the radius of a flat circular disk and ρ is the aspect ratio of its length and width.⁹⁹ For a square pad with sides of size $L \times L$, the disk with equivalent area has $r_{disk} = L/\sqrt{\pi}$. The resulting r_{sphere} for a $10 \mu\text{m} \times 10 \mu\text{m}$ pad is $\sim 6.5 \mu\text{m}$. For water, $\eta = 10^{-3} \text{ Pa}\cdot\text{s}$, so we get $D = 0.03 \mu\text{m}^2/\text{s}$. For microbeads diffusing through a solution, we would expect $\langle x_{th}^2 \rangle = 2nDt$ for diffusion in n dimensions after a time t .⁹⁸ We are interested only in the one-dimensional (y -direction) motion of these cantilevers, so $t = \langle x_{th}^2 \rangle / 2D$, giving a timescale for the cantilever's motion through a potential well of $\sim 50 \text{ nm}$ on the order of 0.04 s .

Fig. 5.3(a) shows a representative section of the data once the probe tip's motion has been subtracted. Using the full data set, we can extract the position of the pad over time, and create a histogram of the centroid locations. The full width at half max of the histogram is related to the standard deviation as¹⁰⁰ $FWHM = 2\sqrt{2\ln 2}\sigma \approx 2.4\sigma$. From the histogram we get $\sigma = \langle x_{th}^2 \rangle^{1/2} = 46 \text{ nm}$, so $k = 2 \times 10^{-6} \text{ N/m}$.

To get more information about the pad's thermal motion, and to ensure that our data is not being biased by time-averaging or aliasing artifacts,¹⁰¹ we can apply power spectral density (PSD) analysis. The PSD provides key additional information, such as

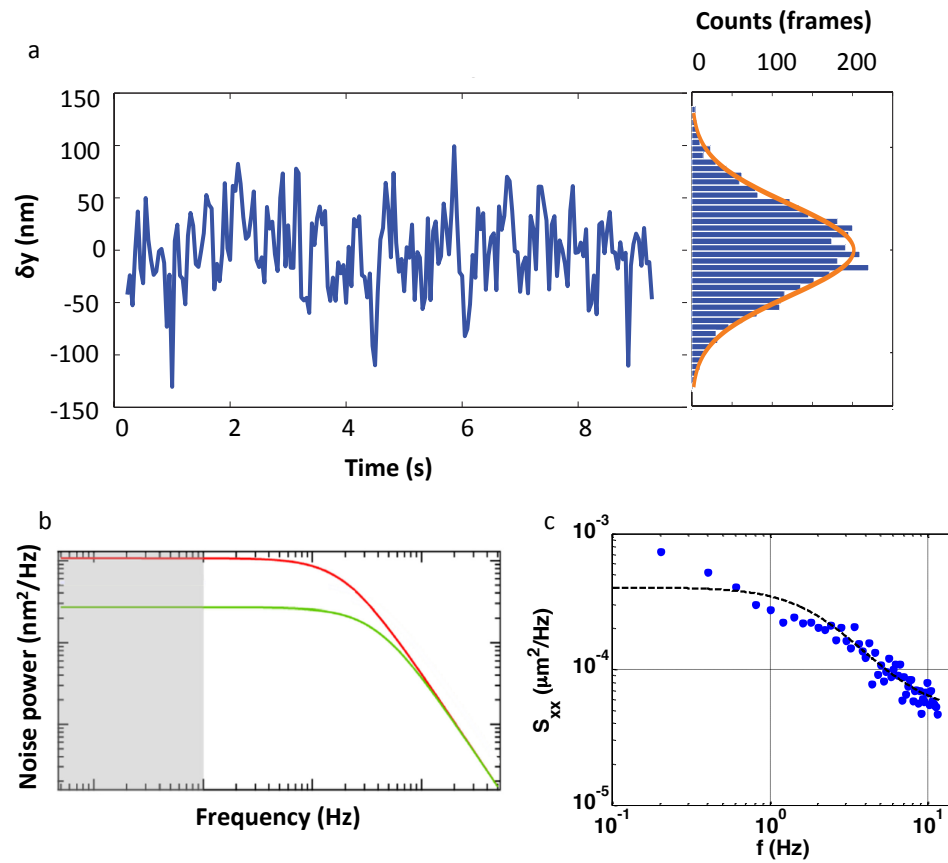


Fig. 5.3: Analyzing the thermal fluctuations. (a) A subset of the same data as in Fig. 5.2 after subtracting the probe tip motion, and a histogram of the size of the pad's fluctuation (extracted from the entire data set). A Gaussian fit to the fluctuation amplitude distribution gives $\langle x_{\text{th}}^2 \rangle^{1/2} = 46$ nm. (b) Theoretical PSD curves. The red line is for a softer spring constant than the green curve; integrating over the area gives a larger variance $\langle x_{\text{th}}^2 \rangle$. (c) A power spectral density plot of the data set. Frame rate is 23 fps. Plots courtesy of Samantha Roberts; (b) is adapted from her thesis.

an experimental value of the diffusion constant, and gives a more accurate value of the variance that filters out low-frequency external noise sources. (See thesis by Samantha P. Roberts, Cornell University (2014) for more details.)

This technique involves analyzing the frequency spectrum of the fluctuations. It tells us how the power (or more generally, the squared value of a signal) is distributed over its component frequencies. To plot the experimental data, we track the position of the pad in time, as in Fig. 5.3(a). The PSD is the normalized square of the fast Fourier transform of the pad's position in time, divided by the frequency and the number of samples n (to normalize it so that the integral gives the variance):

$$PSD_{exp}(x, f) = \frac{2|FFT\{x(t)\}|^2}{fn}$$

for positive frequencies f . The data is shown in Fig. 5.3(c). The vertical axis on the plot is the square of the fluctuation size per unit frequency ($\mu\text{m}^2/\text{Hz}$), and the horizontal axis is the fluctuation frequency.

A key feature is the corner frequency (Fig. 5.3(b)). Below this corner frequency the line is flat, representing the white noise of the cantilever confined to a harmonic potential. At higher frequencies above this corner, the $1/f^2$ dependence of the PSD curve is characteristic of free particles diffusing through the water. Over these short timescales the cantilever does not reach the limits of its harmonic trap.¹⁰²

We can fit this curve using the theoretical expression for the PSD. Written in terms of the diffusion constant D , the one-sided theoretical power spectral density is defined as⁹⁶

$$PSD(x, f) = \frac{D}{\pi^2(f^2 + f_c^2)}$$

for a corner frequency $f_c = kD/2\pi k_B T$, where k is the spring constant of the harmonic potential. The resulting curve provides a fit to the data and lets us directly determine the diffusion constant. In this case, $D = 0.034 \mu\text{m}^2/\text{s}$, very close to the value of $0.03 \mu\text{m}^2/\text{s}$ that we predicted earlier. The data roughly matches the shape of a theoretical PSD curve, confirming that we are correctly sampling the fluctuations. We can also extract the variance directly from the PSD plot using

$$\langle x(t)^2 \rangle = \int_0^{\infty} PSD(x, \omega) d\omega$$

i.e. by integrating to find the area under the PSD curve.

While the device in Fig. 5.3 shows a corner frequency, but some data sets could not provide a clear PSD curve and were discarded. To get a good curve that shows the full form of a PSD, we need to track the pad for long enough to capture the full range of its motion. Good video data will give us the corner frequency, which in turn lets us integrate under the PSD to extract an accurate value of the variance.

For the device in Figs. 5.2 and 5.3, PSD analysis gives $\langle x_{th}^2 \rangle^{1/2} = 38 \text{ nm}$. This is somewhat smaller than the value we read from the histogram above ($\langle x_{th}^2 \rangle^{1/2} = 46 \text{ nm}$), but the PSD analysis is the more accurate measurement because it eliminates some other external sources of noise, particularly very low-frequency noise.

On the plot in Fig. 5.4, we show PSD-extracted data as black dots. For the sample device shown in Figs. 5.2 and 5.3, we get $k = 3 \times 10^{-6} \text{ N/m}$.

5.6 From spring constants to bending stiffness

So far, we have measured the spring constants of monolayer graphene cantilevers. To connect these spring constants k to the bending stiffness, we have to consider the size and shape of the graphene device. Ignoring the graphene's tiny mass, we can treat it as a massless cantilever weighted down at the end by the gold pad. Classical beam mechanics gives the spring constant k of a massless beam of length L , thickness t , moment of inertia I , and Young's modulus Y with its mass fixed at the end:¹⁰³

$$k = \frac{3YI}{L^3}$$

If we substitute the moment of inertia of a rectangular cantilever of width W and thickness t , $I = \frac{1}{12}Wt^3$, we get¹⁰⁴

$$k = \frac{Yt^3W}{4L^3}$$

Finally, we use the expression that relates the bending stiffness of a membrane to its 3D Young's modulus, $\kappa = \frac{Yt^3}{12(1-\sigma^2)}$ (in this case, we'll drop the Poisson ratio in the denominator, since in graphene's Poisson ratio is so small: $\sigma = 0.17$). We now have a simple relationship between the bending stiffness and the spring constant:

$$k = \frac{3\kappa W}{L^3}$$

This means that our measured spring constants give us an experimental value for the bending stiffness of graphene, and we can compare it to theory.

5.7 An experimental value for the bending stiffness of graphene

Figure 5.4 shows the spring constants for all the cantilevers versus their length. There is some scatter in the data, due to variability between devices. Let's begin by comparing the spring constants of our devices to the spring constants predicted by the accepted value of graphene's intrinsic bending stiffness, $\kappa_0=1.2$ eV. This value—which is accurate at the atomic scale—yields expected spring constants given by the dotted orange line in the lower left corner of Fig. 5.4. The experimentally determined spring constants are *orders of magnitude* higher than this prediction.

When we include the effects of thermal fluctuations, however, we see a much better match. In Chapter 4 we showed that the renormalized bending stiffness can be written as $\kappa_{eff} = A\kappa_0(l/l_c)^\eta$. We use $A=1$, $l=W=10$ μm , and the crossover length $l_c=3$ nm that we calculated earlier from the material properties of graphene. We plot the predicted spring constants in Fig. 5.4 using both Nelson and Peliti's original prediction where $\eta=1$ (shown as a dotted gray line) and the more recent predictions where $\eta=0.85$ (dashed gray line). The agreement is very good.

This work represents the first experimental evidence for the effects of thermal fluctuations on the bending stiffness of a membrane. While we cannot rule out the effects of static distortions—permanent crumpling in the graphene, for example—we have shown that the effects of thermal fluctuations are sufficient to explain the dramatically increased bending stiffness of graphene.

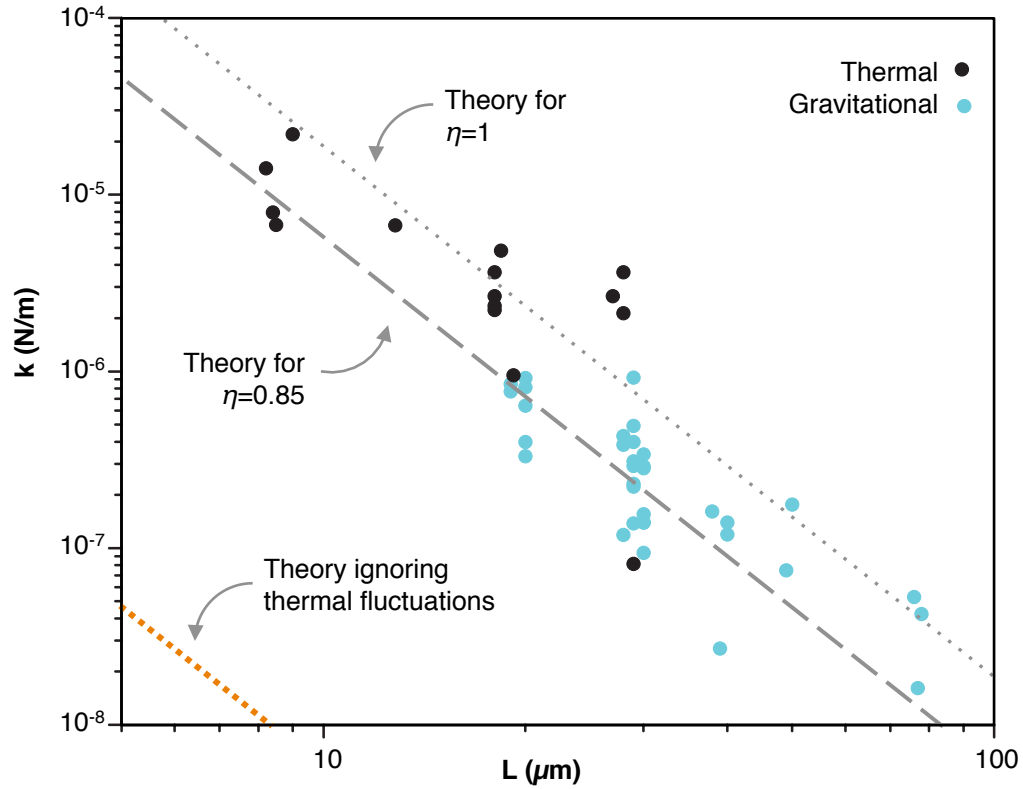


Fig. 5.4: Plot of spring constant versus length for both the thermal fluctuation (black) and gravitational deflection measurements (light blue). The spring constant relates to the bending stiffness as $k=3\kappa W/L^3$. The dotted orange line in the lower left corner is the prediction from the microscopic bending stiffness, 1.2eV. The dotted gray line on the right is the prediction of Nelson and Peliti's original theory ($\eta=1$), while the dashed line is for more recent predictions that give $\eta=0.85$ and $\kappa_{\text{eff}}=1.2$ keV.

5.8 The influence of surfactants and residues on the measured spring constants

Although the effects of thermal fluctuations are enough to explain the dramatic increase in the bending stiffness of graphene, we should take a moment before we leave this subject to double-check that the dramatic increase in bending stiffness could not be caused by other factors: by the inevitable residue on the graphene that we mentioned in Chapter 2, or by the addition of surfactants to the water.

As we saw at the end of Chapter 2, a good fabrication run usually results in ~ 2 nm of additional residue on top of the graphene. We can estimate how much such residue would affect the stiffness using simple classical elastic theory, where $\kappa = Y_{3D}t^3/12(1-\sigma)$. A 2-nm-thick layer of the stiffest PMMA, with a Young's modulus¹⁰⁵ of $Y_{3D} = 3.3$ GPa and a Poisson ratio of $\sigma = 0.4$, would still add only ~ 20 eV to the out-of-plane bending stiffness—far too small an effect to explain the thousandfold increase in stiffness that we measured.

To check the effects of surfactant on the bending stiffness, we performed gravitational measurements on devices that had never been exposed to surfactant. As shown in Fig. 5.5, the presence of surfactant does not measurably affect the bending stiffness.

5.9 Conclusions

We have discussed two separate methods of measuring the out-of-plane bending stiffness of monolayer graphene: using the force of gravity, and using thermal

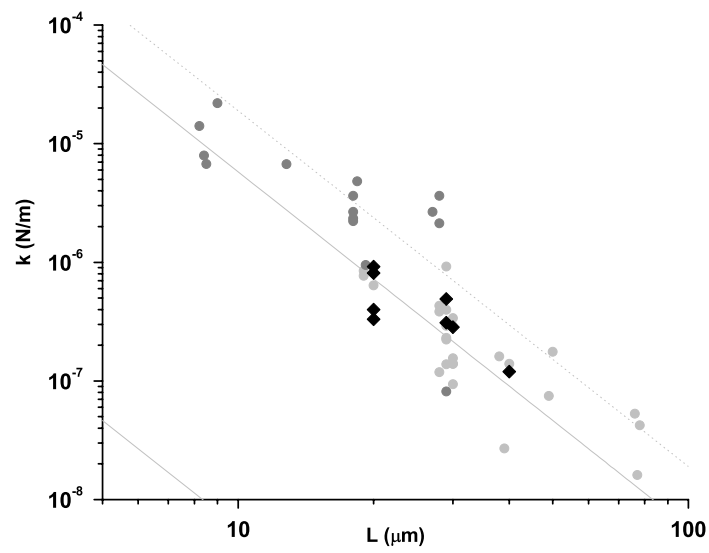


Fig. 5.5: The effect of surfactants. This is the same plot from Fig. 5.4, but the black diamonds are data from gravity measurements on devices that were never exposed to surfactant. The presence of surfactant has no measurable effect on the measured spring constants.

motion. We laid out our measurement methods and showed sample data for both cases. Finally, we used classical elastic theory to extract a bending stiffness from our data. For 10- μm -wide cantilevers, we measured a bending stiffness three orders of magnitude higher than the microscopic value, and showed that this extraordinary stiffness can be explained by the effects of thermal fluctuations in the graphene. This work represents the first experimental evidence for the effects of thermal fluctuations on the bending stiffness of a membrane, and provides a direct measurement of a key mechanical property of graphene.

CHAPTER 6

KIRIGAMI PATTERNS FOR STRETCHABLE GRAPHENE

6.1 Introduction

So far we have mostly focused on developing new manipulation techniques and using them to study the physics of graphene membranes. Here we will begin to use these techniques to build active elements from graphene. We have already discussed the current challenges in building micro- and nanoscale moving parts, and how graphene-based devices might address the need for robust, scalable active elements. In this chapter, we will apply the powerful ideas from the paper art of kirigami to graphene for the first time, and show that it produces resilient moving parts with tunable mechanical properties: a mechanical metamaterial.

In its simplest form, kirigami just requires a material to bend more easily than it stretches, and graphene and paper share this behavior. In fact, we have seen that graphene membranes at the tens-of-microns scale have a νK number comparable to an 8.5"×11" sheet of printer paper. This makes it possible to directly translate designs from the paper arts down to the nanoscale. In Fig. 6.1 we show simple paper kirigami designs based on patterns from a children's craft website, including single- and double-lobed in-plane springs and pyramidal out-of-plane springs.¹⁰⁶ The paper models stretch easily without creasing the paper, and return to their original shape when released.

In this chapter we use the same patterns to build in-plane springs out of

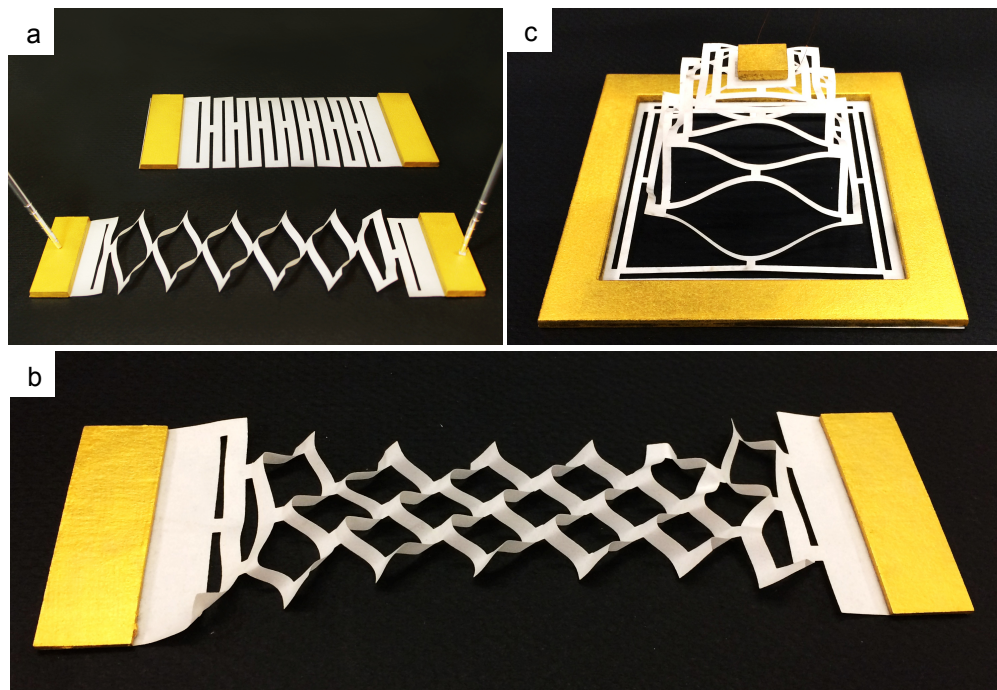


Fig. 6.1: Paper kirigami models. (a) Single-lobed in-plane springs, unstretched and stretched. (b) A similar double-lobed pattern. (c) Out-of-plane pyramidal spring. To create these structures the paper bends, but it does not have to hold a crease.

graphene. We will repeatedly stretch and release them, and image the structure that allows them to stretch. We also pattern pyramidal out-of-plane springs, and actuate them remotely with a laser to measure their force-distance curves. We discuss ways to adjust the patterns to dramatically tune the spring constants. We then move onto the electronic properties of these devices, passing a current through the in-plane springs to turn them into solution-gated stretchable transistors.

6.2 Stretching in-plane graphene kirigami springs

We can directly cut kirigami patterns out of graphene by using the patterning techniques described in Chapter 2. The paper models in Fig. 6.1 were cut using a laser cutter, and the graphene patterning mask was made from the same CAD file (Fig. 6.2(a)). We cut both single- and double-lobed in-plane springs, as well as out-of-plane pyramidal springs. As described in Chapter 2, the last step in the fabrication is to etch away the aluminum sacrificial layer. At this point, the devices look like Fig. 6.2(b), and should be loosely adhered to the surface.

Using a probe tip on a computer-controlled micromanipulator, we can push into the left-hand gold pad and “grab” the end of a single-lobed in-plane spring, just as we did with the cantilevers in Chapter 3. If we pull back on the pad, we begin to peel the graphene off the surface and extend the spring (Fig. 6.3). It releases from the surface one link at a time, until the spring is fully extended and only the right-hand pad is stuck down.

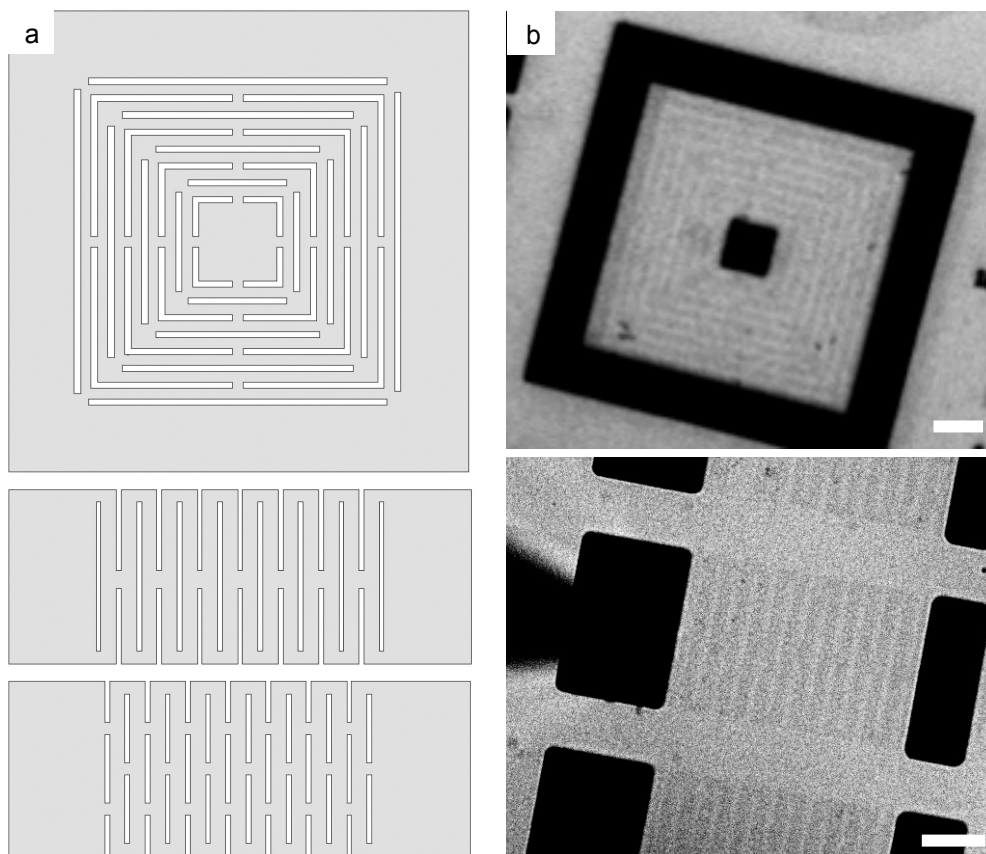


Fig. 6.2: (a) Patterns used for both the paper and graphene kirigami springs. The graphene devices are $80\ \mu\text{m}$ wide with $1\text{-}\mu\text{m}$ -wide cut-outs. (b) Photos of completed devices before they have been peeled up. Scale bars are $10\ \mu\text{m}$.

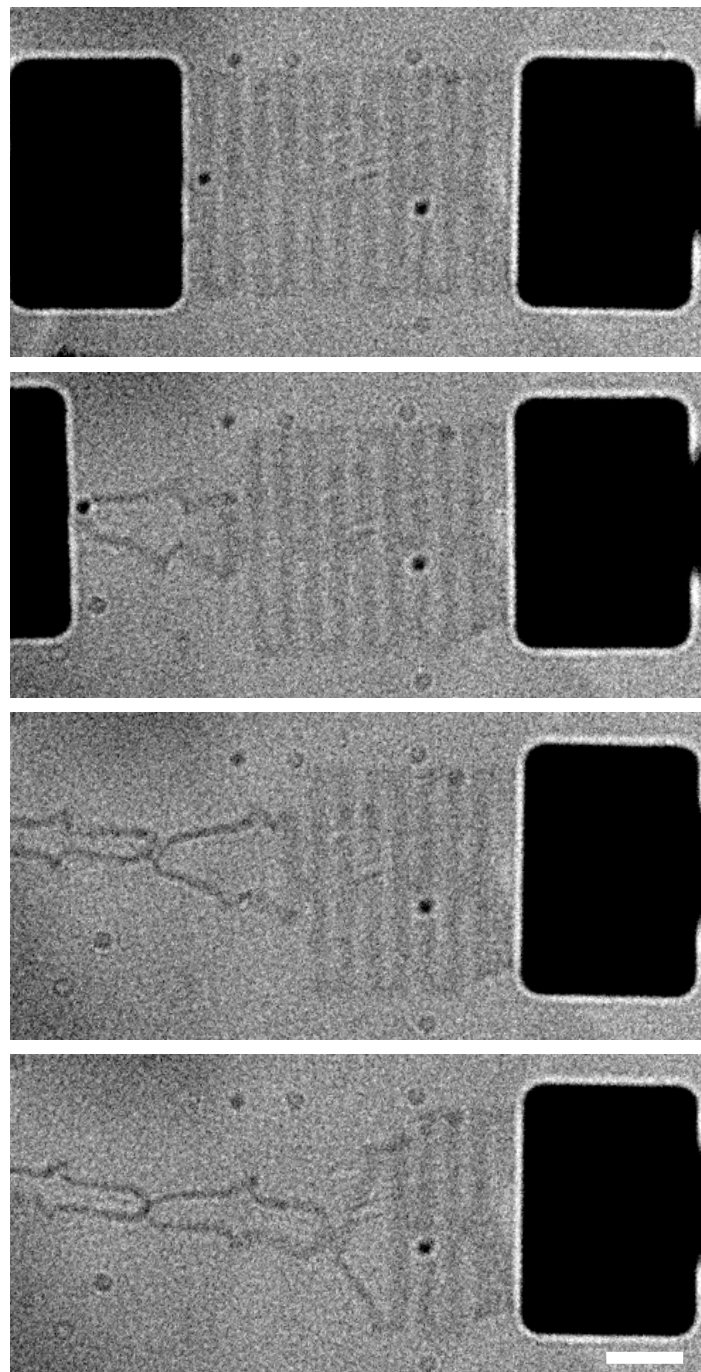


Fig. 6.3: Top to bottom: single-lobed graphene kirigami in-plane spring in the as-fabricated state, and slowly peeling the spring off of the surface one link at a time. Scale bar is 10 μm .

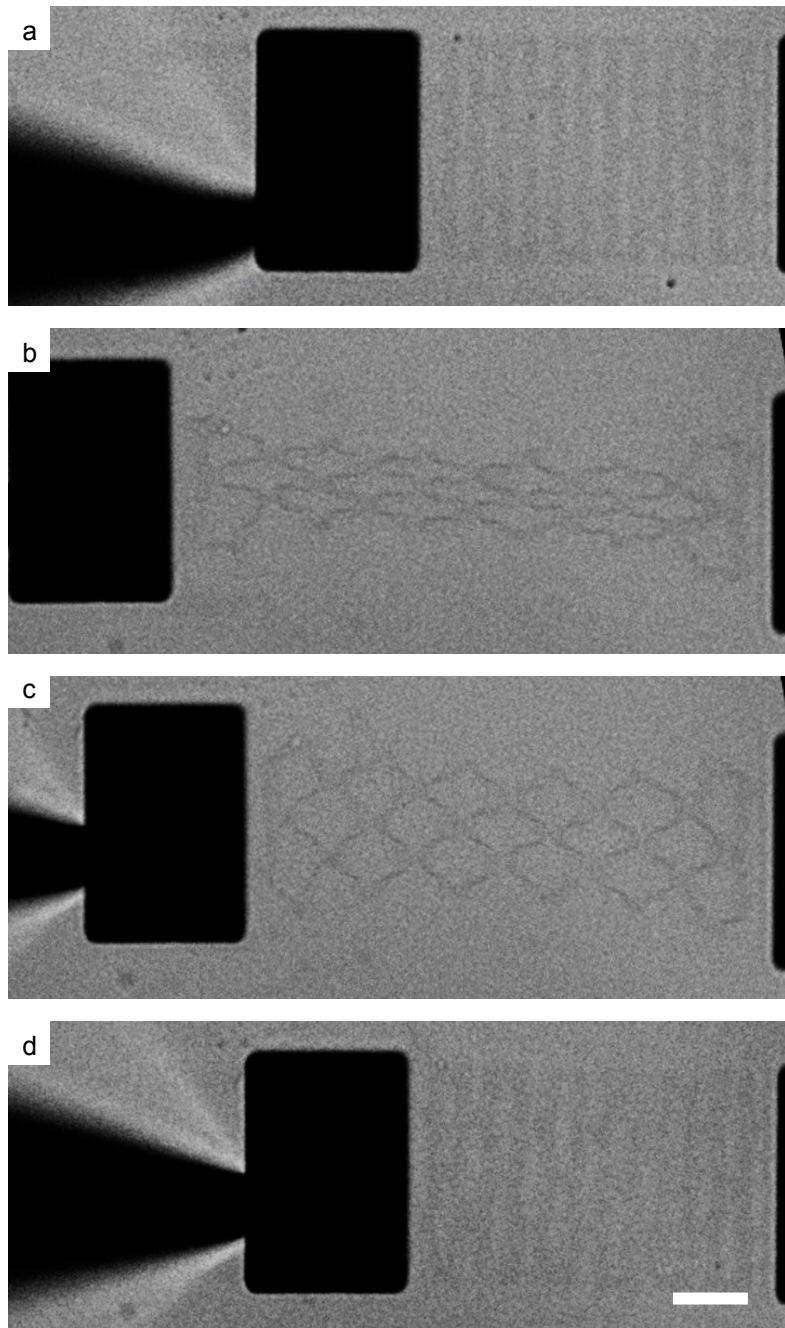


Fig. 6.4: (a) A double-lobed spring before it has been stretched. (b) The same spring fully extended. (c) A partially stretched state from a later cycle. Note that the once the spring has been released from the surface, all of the links stretch and relax together. (c) Bringing the left-hand gold pad back to its original location. Even after many stretching cycles, the spring can return almost entirely to its original state. Scale bar is 10 μm .

The single-lobed spring in Fig. 6.3 can be stretched by over 240%—an even more remarkable mechanical deformation when we consider that graphene normally tears at 6-12%.²⁹ By imposing the kirigami cuts, we have altered the mechanical properties of the graphene device, turning a rigid material into a stretchable one. Once these devices have been peeled up once, they never fully stick down again, and the whole spring is free to stretch in unison. We show a device in Fig. 6.4 that has been released from the surface, and we can see that the entire spring stretches and relaxes as we actuate it. Graphene devices covered with significant residue can be plastically deformed by the stretching process, but good, clean graphene springs should return to their original state, as in Fig. 6.4.

If we pull beyond a kirigami spring's maximum extension point, either the right-hand gold pad can release from the surface (the spring jumps to the left to relax), or the spring can tear. However, as long as we stay within their extension range, these kirigami springs are remarkably robust, and we have stretched and relaxed similar springs hundreds of times. In the next section we will study the mechanism that allows these graphene kirigami springs to stretch so dramatically.

6.3 How the springs stretch / 3D reconstructions

We can study the macroscale paper springs to learn how kirigami springs stretch. We will examine the structure of the simple single-lobed spring in Fig. 6.1(a).

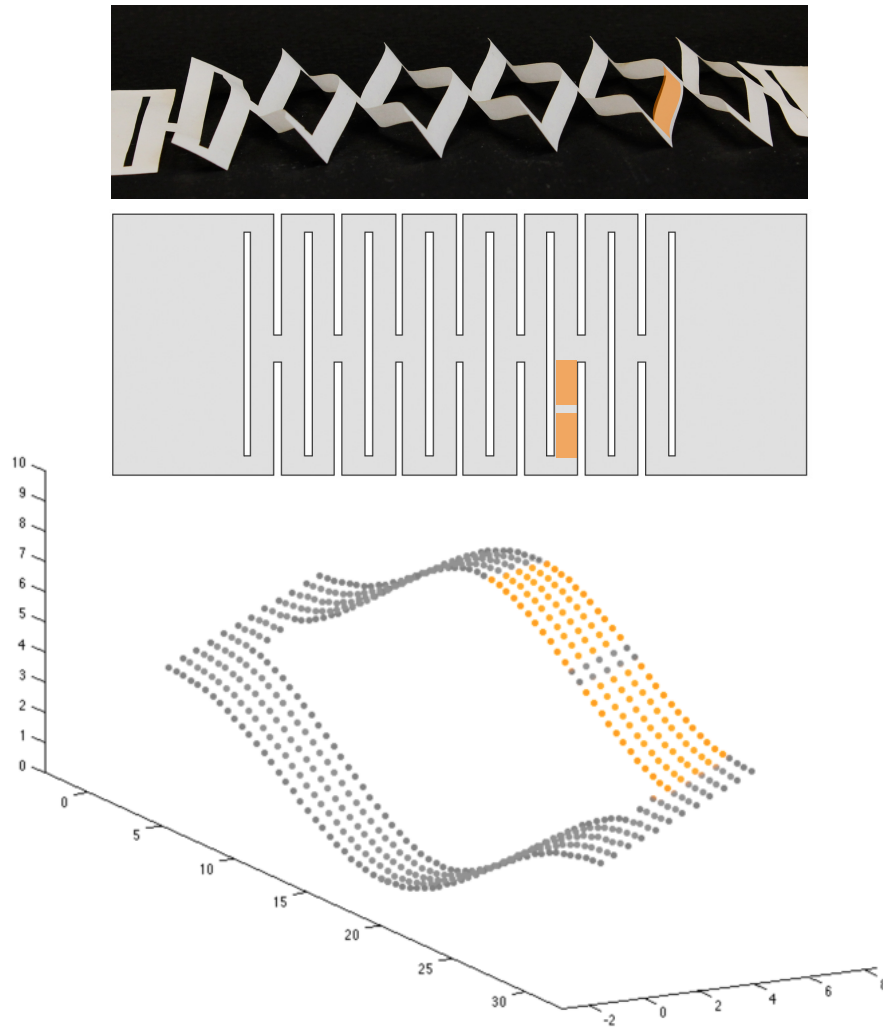


Fig. 6.5: (a) A paper kirigami spring from the side. The links rotate out of plane, and are then free to bend like cantilevers. (b) Each small strip of graphene in this pattern can be thought of as two cantilevers in series (labeled orange), which together form an *s* shape. (c) A finite difference method model of a single spring cell, with two cantilevers labeled in orange. Image courtesy of Bryce Cobrin.

This spring is made up of identical “links” connected at the middle of the device.

As we begin to stretch the spring, the spring bends up at its ends so that the individual links can rotate up out of plane (Fig. 6.4(a)). Once the links have rotated, they are free to act as rectangular cantilevers in series and parallel (labeled orange in Fig. 6.4(b)). As these cantilevers bend, the spring extends. Because the paper bends out of plane, the spring constants of the kirigami spring will depend on the bending stiffness of the paper, not its Young’s modulus.

A graphene spring should stretch by the same mechanism. To confirm that the 3D structure is in fact the same, our collaborators in the Muller group reconstructed the three-dimensional shape from a focal series of a partially released spring (Fig. 6.6(a)). We scanned 100 μm in z at a constant rate using the z -piezo on the microscope objective, creating an image stack in 10-nm steps (which, we should note, is significantly oversampled, since the depth of focus is $\sim 0.5 \mu\text{m}$).

For each x - y pixel, our collaborators used a Gaussian fit to determine the z plane with the highest contrast (i.e. the most focused plane) using a refined minimum intensity algorithm. Simply selecting a maximum-intensity height at each pixel already gives information about the 3D structure, but the fit can be improved by adding in a number of refinements. Background subtraction eliminates constant features, such as particles on the lens and the camera. They treated the graphene as a point object in z . They masked the z -data to the projection of the object, and adjusted the fit near the pads, since opaque objects cast a shadow as they go out of focus. And finally, they

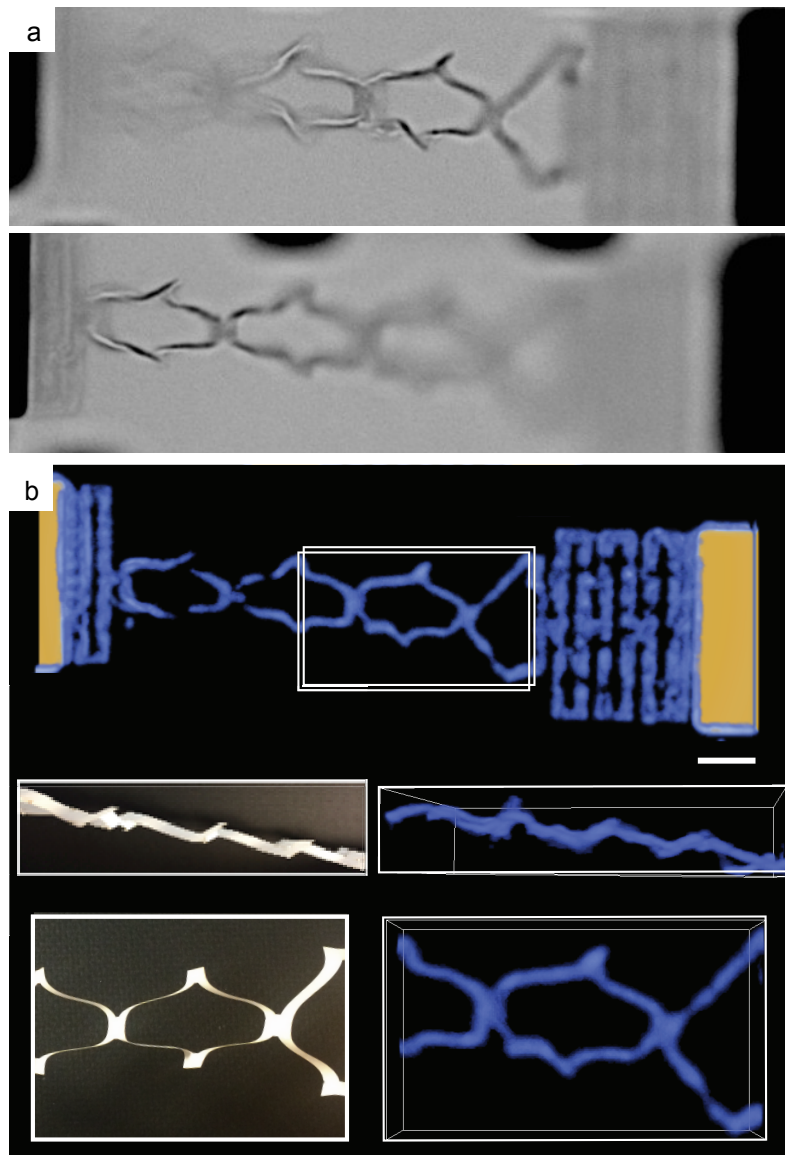


Fig. 6.6: (a) Two stills from the background-subtracted z-scan. (b) The 3D reconstruction using TomVis, and matching paper models. The color map is based on the intensity of the original video. The image of the upper lefthand paper model has been compressed vertically.

Gaussian-blurred in three dimensions by 400 nm to reduce noise.

To render the 3D model, they used an open-source program by Paraview called TomVis, which is designed for tomography.¹⁰⁷ The result is shown in Fig. 6.6(b), where we compare the reconstruction to paper models. The only significant difference is that the upper photo of the paper model has been vertically compressed; the reconstruction's compression in z is a function of the fact that we treat the graphene like a point object in z .

Recently, researchers have modeled this structure using molecular dynamics simulations.¹⁰⁸ The 3D structure of their nanometer-sized graphene kirigami springs agrees with this reconstruction, in spite of the fact that they were modeling patterns at much smaller scales. In fact, this simple kirigami design should work at any size scale as long as the material prefers to bend rather than stretch.

6.4 Tuning the spring constant by changing cut patterns: a mechanical metamaterial

We have described the kirigami springs as collections of small cantilevers in series and parallel. In this section we will show that this simple model does a good job of predicting the measured spring constants. We then use this model to predict the range of spring constants that we should be able to achieve by changing the kirigami pattern.

Fig. 6.7(a) shows the graphene pyramidal spring, which stretches like in-plane

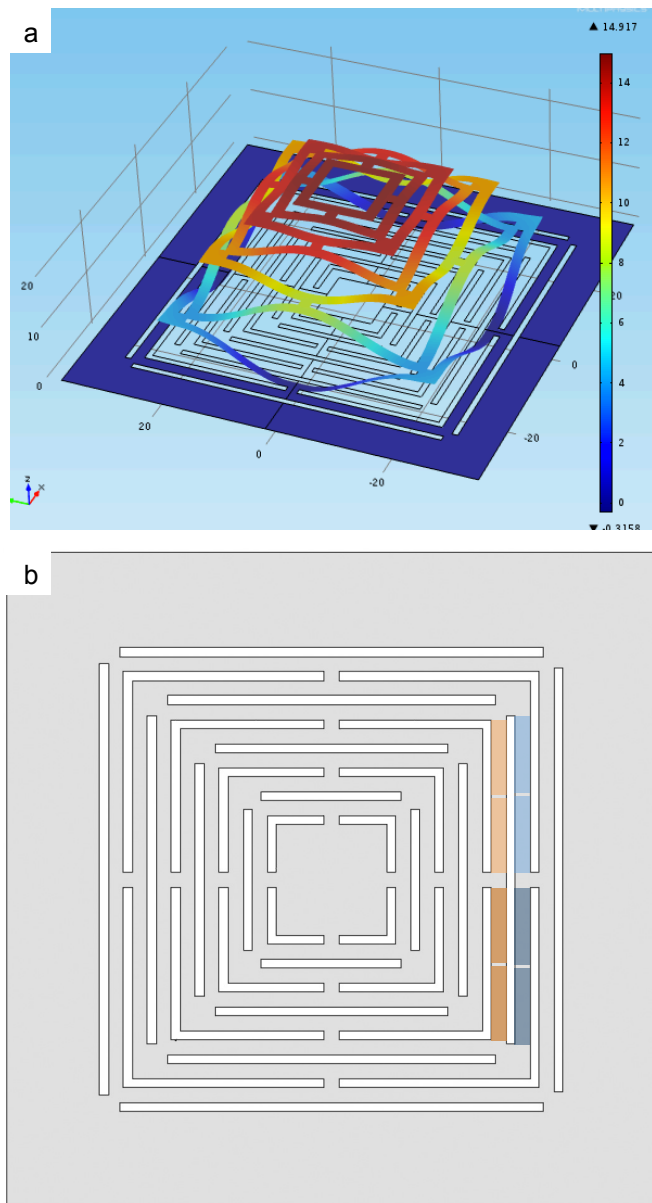


Fig. 6.7: (a) A COMSOL finite-element-analysis model of an out-of-plane pyramidal kirigami spring showing the three-dimensional structure. The color scale represents height. Courtesy of Bryce Kobrin. (b) A simple model of the out-of-plane spring treats it like cantilevers in series and parallel. Each blue and red cantilever: $2 \mu\text{m} \times 9.75 \mu\text{m}$. Each orange cantilever: $2 \mu\text{m} \times 9.5 \mu\text{m}$.

spring but without the initial step of rotating the links. A schematic of the spring is shown in Fig. 6.7(b). We will build up the simplest possible model here, focusing on one quadrant of the spring and treating the four quadrants like independent springs in parallel.

By playing with paper models we know that the outermost strip of graphene (A) is tensioned by the gold at its ends, so it cannot significantly bend out of plane (see Fig. 6.1(c)). We will begin by counting at the second strips of graphene, labeled blue. We begin by focusing on the light blue strips.

This long, narrow piece of graphene will bend out of plane in an S shape, as we saw earlier, so we again treat it like two simple cantilevers in series. These cantilevers are $2\ \mu\text{m} \times 10\ \mu\text{m}$, and their bending stiffness and spring constants will depend on their size as in Chapter 4 and 5. The bending stiffness should be $\kappa_{eff} = A \kappa_0 (l/l_c)^\eta$, which gives $\kappa_{eff} = 300\ \text{eV}$ for $l = W = 2\ \mu\text{m}$. So each of these little cantilevers will have a spring constant of $k_C = 3\kappa_{eff}W/L^3 = 3 \times 10^{-7}\ \text{N/m}$.

Spring constants add as follows:

$$\textbf{In series:} \quad \frac{1}{k_{tot}} = \frac{1}{k_1} + \frac{1}{k_2}$$

$$\textbf{In parallel:} \quad k_{tot} = k_1 + k_2$$

So we add up the spring constants of the two light-blue cantilevers in series; add the spring constants of the *dark* blue cantilevers in series; and add the two totals in parallel. Continuing on, we add the total for the orange cantilevers in series with the blue ones. We continue this process until we reach the gold pad at the center. Finally,

we add the four quadrants in parallel. This gives a total spring constant for the complete pyramid of $k_{theory}=5\times 10^{-7}$ N/m.

If we ask what range of spring constants are possible, we find that the upper and lower limits are hard to define—we can always make the component cantilevers longer and thinner or add more in series to soften the spring, or we can make them shorter and wider and add more in parallel to stiffen the spring. To make a rough estimate, however, we can place some very conservative limits on our patterns. We will use the minimum feature size of our current optical lithography system ($\sim 0.5\ \mu\text{m}$) and a maximum device size of the largest devices we have picked up ($\sim 100\ \mu\text{m}\times 100\ \mu\text{m}$). We stress that these are not hard limits, and smaller feature sizes or larger graphene devices could easily be made. Within these limits we find that we can already achieve spring constants from 1 N/m to 10^{-9} N/m—a striking nine orders of magnitude that cover the force range from AFM tips to optical traps.

These kirigami springs are mechanical metamaterials: their properties depend on their *pattern*, not on the intrinsic properties of the material. We could tune their spring constants to match the needs of a particular experiment or application, where these springs could be used as in-plane or out-of-plane force measurement devices. They are easy to fabricate, biocompatible, and allow us to *visually* read out forces down to the femtonewton scale (assuming $\Delta F = k\Delta x$ for $k=10^{-9}$ N/m and a very reasonable $\Delta x=1\ \mu\text{m}$).

6.5 Laser actuation and a force-distance curve

As we study these springs, it seems obvious to ask for their spring constant—or better yet, for a force-distance curve. The pyramidal geometry allows us to actuate this spring with a laser to get a full force-distance curve.

If we pick an entire pyramid up off of the substrate by the gold frame, the central pad hangs down under the force of gravity. Using the laser, we can push the pad upwards, and even extract a force-distance curve. We push on the central gold pad with an infrared laser ($\lambda=1064$ nm). The experimental setup is built on an inverted microscope, so the laser passes through the objective and pushes up, against the force of gravity (Fig. 6.8).

Using an acousto-optic modulator, we were able to controllably adjust the laser power. The force due to photon pressure is:

$$F = \beta \frac{Pn}{c}$$

where P is the power of the incident light, n is the index of refraction, and c is the speed of light, and β is a numerical prefactor that depends on how much of the light is lost along the optical path. We can directly calibrate this force against the force of gravity using simple graphene cantilevers by measuring the position of the pad (a known weight) at different values of the laser power. To check that this calibration was not being influenced by possible static deflections of the cantilever, we performed this measurement using a 2- μm -wide cantilever, where the cantilever stiffness is negligible and the graphene simply acts as a tether for the gold pad.

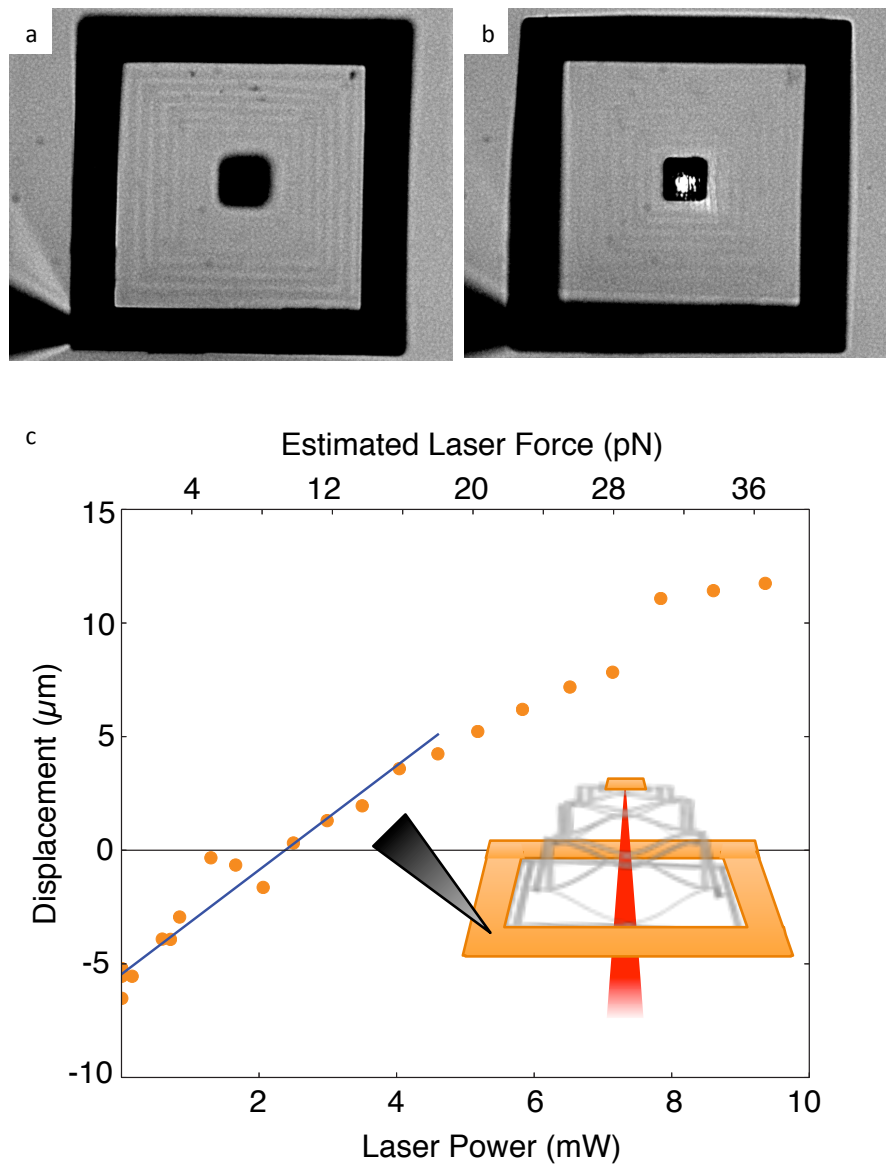


Fig. 6.8: Actuating pyramidal springs with a laser. (a) Out-of-plane spring with the laser off and (b) striking the central pad. (c) Force-distance curve for a pyramid (inset: cartoon of experimental geometry).

This lets us calibrate the force axis in Fig. 6.8(c). Tracking the z -position of the central pad of the pyramid as we vary the laser power, we can extract the full force-vs.-distance curve. A fit to the linear section of the pyramidal spring gives a spring constant of $k=2\times 10^{-6}$ N/m — reasonably close to what the simple model above predicts.

As we would expect for an ideal spring, there is a fairly linear region in the middle, with a roll-off as the spring reaches its maximum extension. The linear region also confirms that the force is in fact due to photon pressure, rather than to heating the fluid or other nonlinear effects.

The force-distance curve gives us quantitative information about how graphene kirigami springs stretch, and the measurement of the spring constant suggests that the simple cantilever model will be useful for designing springs with custom spring constants. So far we have focused on the mechanical properties of graphene kirigami springs, but these remarkable mechanical metamaterials can also act as stretchable transistors. We will explore their electrical properties in the next section.

6.6 Electrical properties of graphene kirigami springs

There has been great interest over the years in using graphene for transparent or flexible electrodes, and researchers have worked on stretching graphene up to or past its normal $\sim 12\%$ limit.^{29,109,59,110,111} These projects usually aim for maximum strains of 5-30%.^{110,43} Other kinds of stretchable electrodes such as gold nanomeshes can survive strains of over 100%, but that is usually at the cost of a significant change in the electrical properties when the electrodes are stretched.¹¹² Ideal stretchable

electronics should be resilient enough to survive many stretching cycles without deteriorating, and their electrical properties should not change significantly when the device is stretched. The graphene kirigami springs we have shown so far in this chapter are certainly mechanically resilient, and their maximum extensions are set only by the choice of patterns. In this section we will study their electrical stability.

Electrolyte gating is a well-established technique.^{113,114,115,116} A transistor with source and drain hookups is immersed in an ionic solution, and the voltage of the solution is set by a third wire, the electrolyte gate wire. Ions build up on the gate wire and on the device, creating a liquid top gate for the transistor (Fig. 6.9(a)). To a first approximation, a conductor/electrolyte interface can be thought of as a layer of ions at the conductor's surface that forms a capacitor, as shown in Fig. 6.9(b). By changing the voltage of the gate wire, we can pull charge onto and off of the graphene from the contacts, just as in traditional back-gated transistors. (For more details, see Lisa Larrimore's thesis, Cornell University (2008).)

To measure the electronic properties of the kirigami springs, we will gate them using an electrolyte solution of ~10 mM KCl, plus a few drops of the standard surfactant solution (with water added periodically to keep the concentration stable). We added a gold gate wire to the solution to set its potential, and use a current preamplifier (Ithaco 1211) to measure the current through the device in response to an applied source-drain voltage.

We use the usual tungsten tip to contact the source electrode (the left-hand gold pad), but contact the drain electrode (the right-hand gold pad) with a parylene-C-

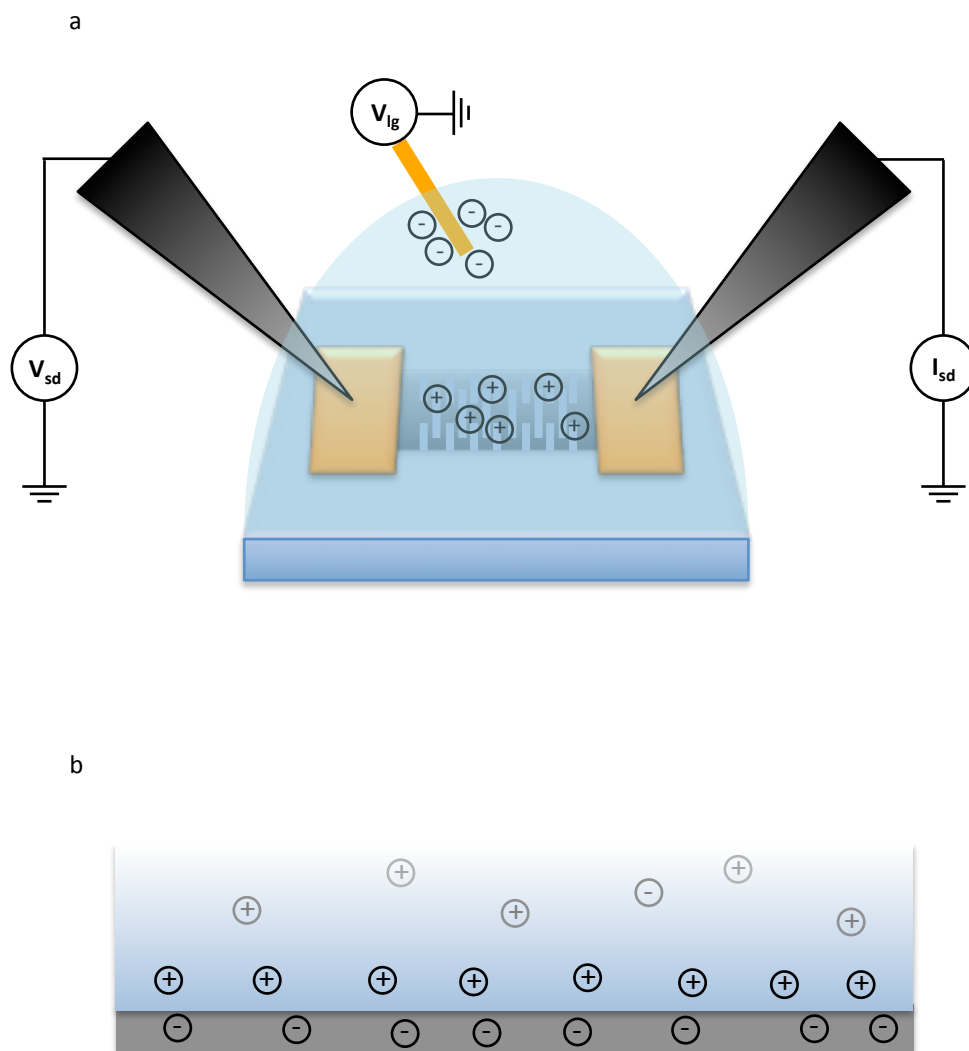


Fig. 6.9: Cartoons of electrolyte gating. (a) The experimental setup, showing a gate wire that attracts charge and sets the potential of the solution, thereby gating the graphene. (b) Positive ions in the solution draw electrons onto the graphene device.

coated tungsten probe to minimize leakage current between the gate and drain through the solution. With these probes, the system had a negligible gate-drain leakage current of ~ 10 nA.

We begin by measuring the electrical response of a kirigami spring before we have first released from the surface. We hold the device at a 100 mV source-drain bias and sweep the electrolyte gate from positive to negative voltages. The blue curve in Fig. 6.10 shows the resulting plot of conductance vs. gate voltage. We see the characteristic Dirac point structure of a graphene transistor, as in Chapter 1. This single-lobed spring geometry is equivalent to ~ 40 squares in series, so we can calculate the resistance per square from the total measured resistance. The device in Fig. 6.8 gives $R=12$ k Ω /square at the Dirac point. We also extract the transconductance, which is a common metric for the effectiveness of the gating in field-effect transistors. It tells us how much the output current changes for a given change in the gate voltage, and can be extracted from the slope of the line on the two sides of the Dirac point in Fig. 6.10. For this device, the normalized transconductance per square gives 0.7 mS/V, comparable to the values reported in the literature for electrolyte-gated graphene transistors. As we might expect, the device behaves like a standard electrolyte-gated graphene transistor.

Next, we peel the spring off of the surface and stretch it to its full extension, a strain of over 240%. We again sweep the electrolyte gate, which is shown as an orange curve in Fig. 6.10. Remarkably, the transistor curve does not change significantly when the device is stretched.

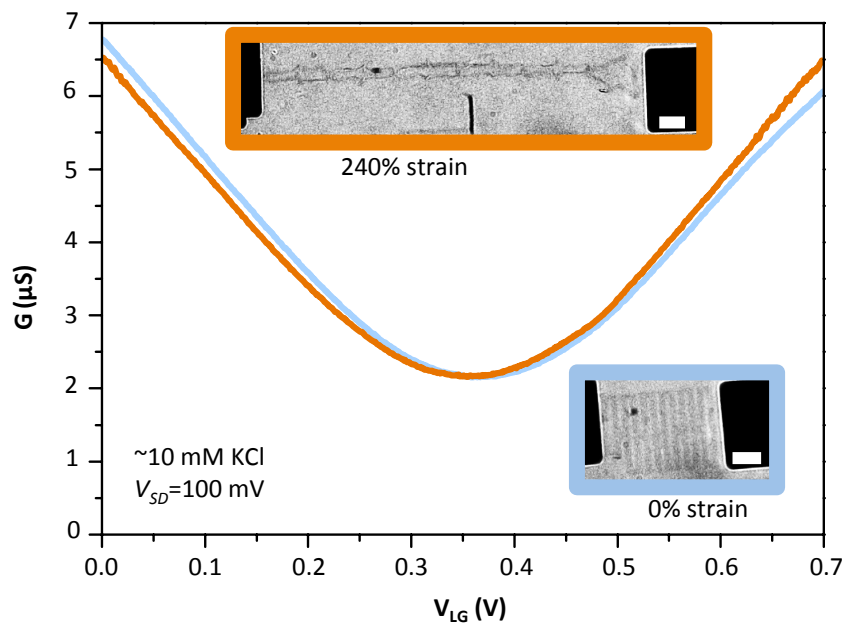


Fig. 6.10: Graph of gate voltage versus conductance for a spring before it has been stretched (blue) and when it is stretched by 240% (orange). Scale bars are $10 \mu\text{m}$.

This unusual electrical stability is due to the fact that we are not significantly straining the graphene lattice, only the kirigami superstructure. As we discussed earlier, the graphene is simply bending out of plane at a large radius, and we would expect such gentle out-of-plane deformations to have no significant effects on the electrical properties of the graphene. In fact, we stretched a similar spring over 1,000 times without significantly degrading its electrical properties.

6.7 Conclusions

We have shown that applying simple kirigami patterns to graphene results in extraordinarily robust springs. We built in-plane and out-of-plane springs, studied their stretching mechanism, and extracted a force-distance curve. We predicted the range of possible spring constants for graphene kirigami devices, and found that these springs are mechanical metamaterials, with remarkably tunable spring constants across a wide and experimentally valuable range. Finally, we studied the electrical properties of graphene kirigami springs, which proved to be excellent stretchable transistors.

In the next chapter, we will continue to explore possible applications for kirigami, and suggest future experiments that will take advantage of the remarkable mechanical and electrical properties of kirigami devices.

CHAPTER 7

APPLICATIONS OF GRAPHENE KIRIGAMI AND FUTURE DIRECTIONS

7.1 Introduction

In this thesis, we have controllably peeled graphene free from a surface in solution and manipulated it in real time like a sheet of paper. We measured the bending stiffness of graphene, and showed that the stiffness in 10- μm -wide cantilevers is three orders of magnitude higher than the atomic-scale value, a dramatic effect that can be explained by thermal fluctuation theory. Finally, we drew on known techniques in the paper arts to create moving parts that can be repeatedly actuated. We built robust hinges, three-dimensional structures, and springs that can act as force sensors or stretchable transistors. We hope that this work will open up a world of new applications for graphene, and provide a new framework for thinking about nanoscale actuation.

At just one atom thick, graphene represents the ultimate two-dimensional membrane. Although we have focused entirely on graphene in this thesis, many of the principles and techniques we have discussed could be applied to the expanding world of two-dimensional materials (Fig. 7.1). From transition-metal dicalcogenides¹¹⁷ to boron nitride¹¹⁸ to 2D glass,¹¹⁹ there has been a wave of research on 2D materials in the last few years. These materials add a wide variety of electronic, structural, mechanical, and optical properties to the world of two-dimensional membranes,¹²⁰ and may create new possibilities when we lift them off of a substrate and begin to cut, bend, and stretch them. As we have shown, kirigami patterns do not undergo significant strains when they stretch, so these techniques should work even for 2D materials that do not share graphene's extraordinary strength.

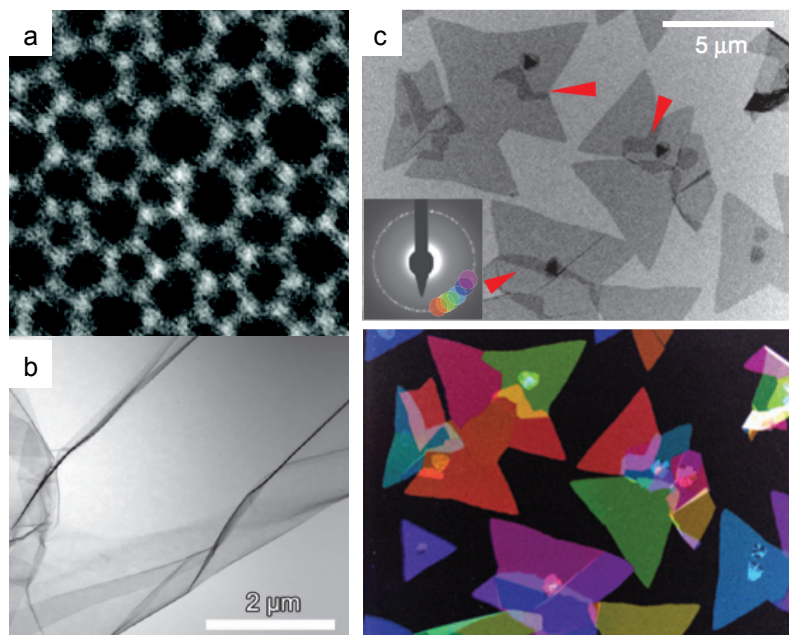


Fig. 7.1: Other two-dimensional materials that might be used for kirigami applications. (a) An atomic-resolution image of silicon oxide glass on a graphene support. (b) Crumpled molybdenum disulfide (MoS₂) sheets look qualitatively similar to crumpled graphene. (c) Bright- and dark-field TEM images of CVD-grown MoS₂ crystals.

In this final chapter, we will focus on future experiments and applications for graphene kirigami, including building electrostatics and adhesion sensors and creating graphene cantilevers and springs in vacuum. We will discuss the magnetic control of graphene devices, and discuss possible applications to optics. Finally, we will discuss possibilities for the controlled creasing of graphene, with an eye to true origami.

7.2 Studying adhesion and electrostatics in solution with graphene kirigami sensors

We have shown that graphene kirigami devices are mechanically and electrically stable, and may serve as moveable, flexible electrical and force sensors. A simple first step towards using the existing graphene kirigami devices as sensors would be to apply a gate voltage to a large gold pad (Fig. 7.2(a)). As we move the electrically contacted graphene device close to the large gold pad, we should see a change in its resistance as it enters the electrical field. This effect should be strongly distance-dependent, as we should only begin to see an increased gating effect once the graphene is within the solution's Debye screening length of the large gold pad. For a 1:1 ionic solution such as KCl, the Debye length at room temperature should be $\sim 0.304/\sqrt{I}$, where I is the molar ionic concentration.¹²¹ For the 10 mM solution we used in Chapter 6, this gives ~ 3 nm. This can be a short-range effect, but can be tuned by changing the ionic concentration. We may be able to use this sensitivity to extract interesting information about what exactly is happening at the interface between the graphene, the water, and the gold.

In Chapter 6, we mentioned using the kirigami springs as sensitive force sensors, and these devices would be ideal for studying interfacial effects (Fig. 7.2(b)). The pyramidal out-of-plane springs can be picked up by the frame, as we showed in

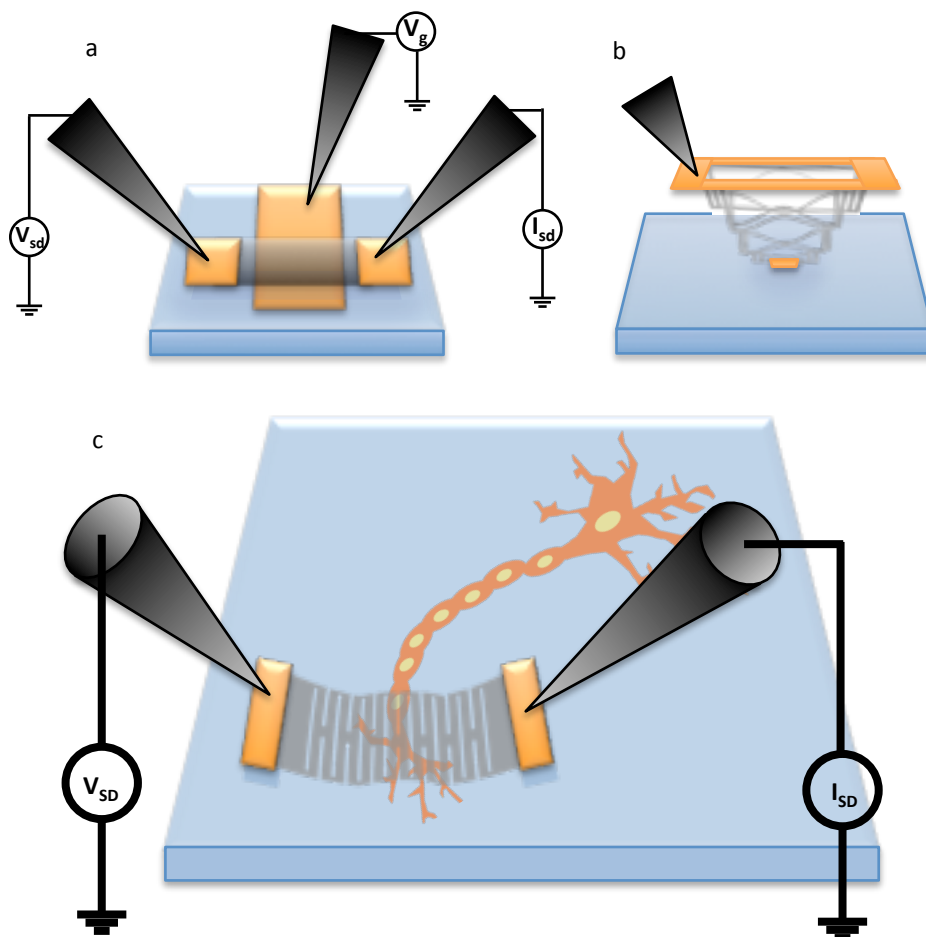


Fig. 7.2: Electrostatic and adhesion experiments. (a) Electrical sensors, (b) force sensors for electrostatics or substrate adhesion studies, and (c) mobile and stretchable electrical sensors for making intimate contact to neurons.

Chapter 6. When the spring is first peeled up off of the surface, the central pad (gold with graphene underneath) sticks down until the spring is relatively extended, and then pops up off of the surface. The extension of the spring (and the known spring constant) gives you a direct measurement of the adhesion force. We can also set the central pad back down and pick it up again, to see whether the device ever sticks back down to the surface at all (re-adheres), or if it floats on a layer of water. As we mentioned in Chapter 3, there seem to be interesting questions of adhesion at the graphene/water/substrate interface, and such effects could be probed using these devices. We could also use this geometry to study the kind of solution electrostatics described above.

We can imagine using these electrically contacted kirigami springs as electrical sensors in a variety of applications, including in cellular studies. For example, they could be easily integrated with biological studies of neural networks (Fig. 7.2(c)) by simply moving the spring to wherever a neuron sits. When we press the spring up against the neuron, it should make intimate contact, stretching to conform to the Gaussian curvature of the surface. By patterning soft kirigami springs, we can also ensure that they will not damage the cells. Our group is already making early attempts at moving electrically contacted graphene devices to live neurons to act as sensors.

7.3 Cantilevers and kirigami in vacuum

While the aqueous environment has many significant advantages, there may be cases where we prefer to work in vacuum or air. With cantilevers in vacuum, we could sweep the temperature over the wide range needed to explore the temperature

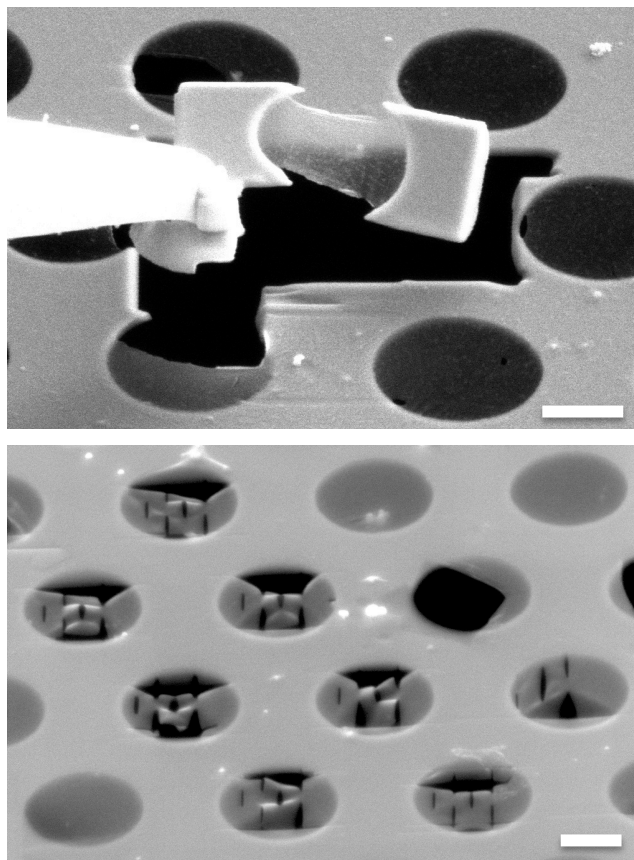


Fig. 7.3: Patterning suspended graphene in vacuum using a focused ion beam. (a) A graphene cantilever with silicon nitride pads. These devices can be welded to a micromanipulator probe tip and removed from the vacuum chamber entirely. (b) Graphene kirigami springs cut out of suspended graphene membranes. Scale bars are 1 μm .

dependence of the bending stiffness. Furthermore, not all experiments are liquid-friendly, and devices in vacuum might be more easily integrated with other research projects.

We can cut simple cantilevers and kirigami springs in vacuum by suspending graphene under tension, as described in Chapter 1, and using a dual-beam focused ion beam (FIB) to cut through the graphene and the nitride TEM grid (Fig. 7.3).⁸⁸ We have cut cantilevers with silicon nitride pads that are robust enough to be removed from the vacuum chamber. This approach may lead to devices that can be integrated into existing experimental setups in vacuum or air that would open up new possibilities for probing the physics of kirigami devices.

7.4 Magnetic tweezer control of graphene devices

We have already demonstrated both direct actuation techniques using micromanipulators and remote actuation using lasers. As we begin to think about building more complex structures or parallel arrays of moving parts, magnetic fields become a promising remote actuation mechanism (Fig. 7.4). Instead of using gold pads to directly control the graphene device, we can use iron pads and pull on them with a magnetic field.

Magnetic tweezers can be based on permanent magnets or electromagnets, and are already a well-established tool for single-molecule studies.^{122,123} A ferromagnetic pad has a permanent magnetic moment μ that will try to align with the field. It will experience a force based on the gradient of the field,¹²⁴ as $F = \mu \cdot \nabla B$. Magnetic tweezers can exert strong forces of up to tens of nanonewtons.

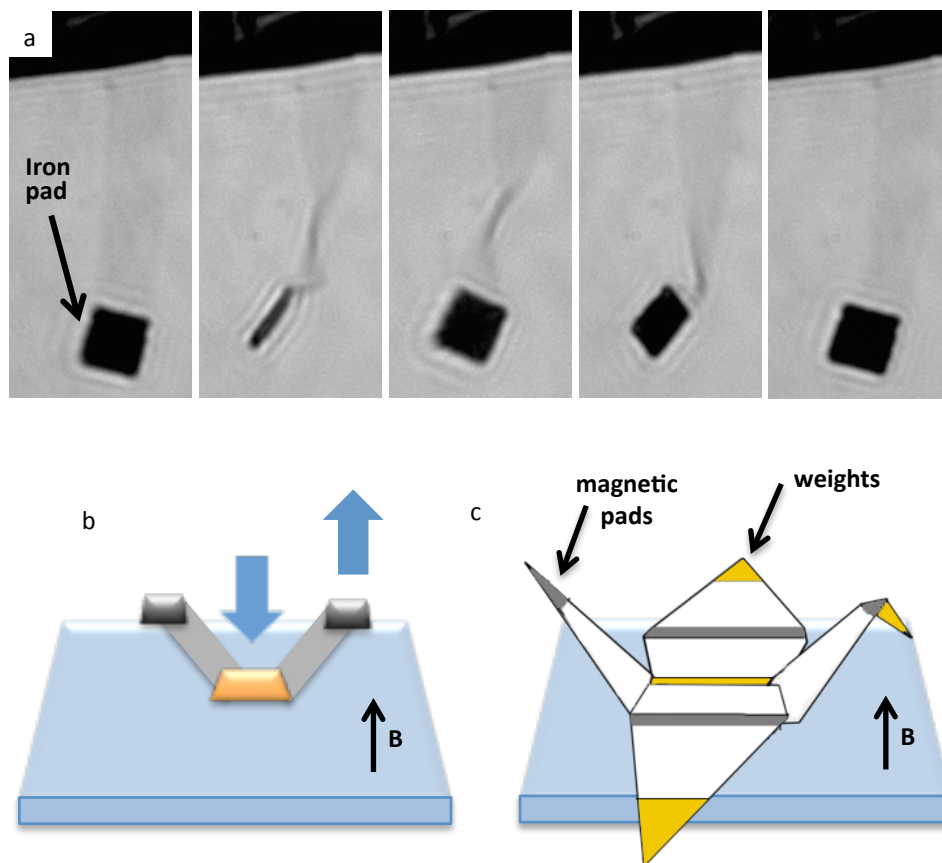


Fig. 7.4: Magnetic control of graphene devices. (a) Twisting a long graphene cantilever with a rotating magnetic field. The gold pad has been replaced by a ferromagnetic iron pad. (b) A simple model structure that will pop up when a magnetic field is applied. (c) A more complex model.

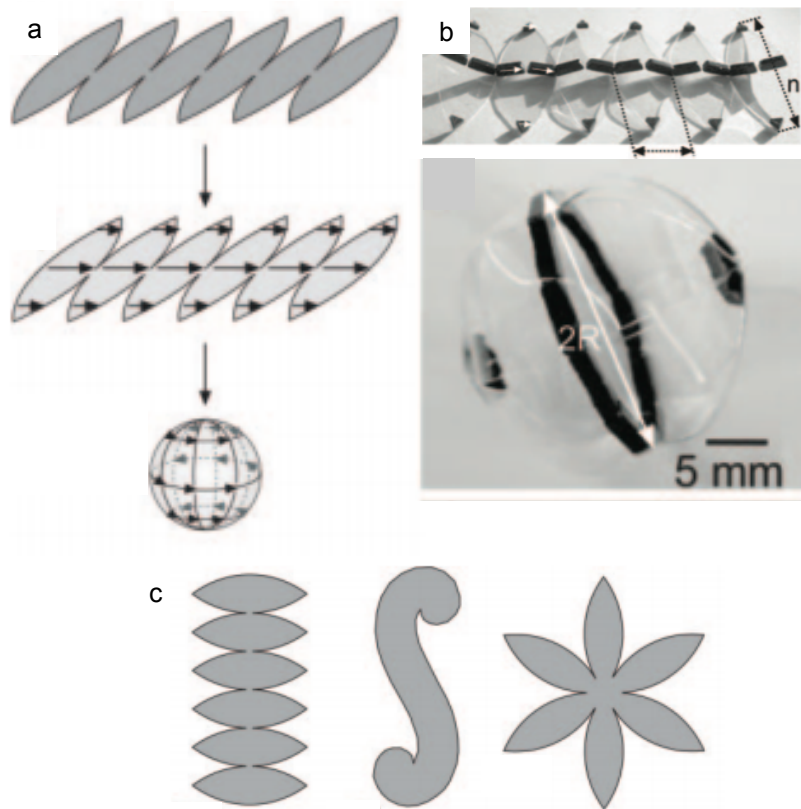


Fig. 7.5: Magnet orientations and starting patterns for building spheres from planar sheets. (a) A flat pattern with small ferromagnets pops into a sphere. (b) Macroscale models. (c) Other possible starting geometries. All figures from *Magnetic self-assembly of three-dimensional surfaces from planar sheets*, Boncheva et al. (2005)

For her PhD work in our group, Samantha Roberts developed novel techniques for manipulating carbon nanotubes with magnetic fields,⁹⁶ and has also begun to apply these techniques to simple graphene devices. She opened and closed arrays of graphene hinges with an electromagnet, and twisted and untwisted a long cantilever using a rotating magnetic field that exerts a torque¹²⁴ $\tau = \mu \times B$ (Fig. 7.4(a)). We can imagine using this technique to apply local upwards forces while using surface tethering or weights to keep the device in place. It would also allow us to build temporary three-dimensional structures (Fig. 7.4 (b-c)).

We can imagine using this method to build permanent 3D structures such as a spherical envelope (Fig. 7.5). The problem of how to pattern a flat sheet with small local magnets so that it can pop into a sphere has been solved at the macroscale,¹²⁵ and could be directly applied to graphene by patterning in the correct magnetic pads.

In addition to using magnetic fields to build and actuate graphene devices, we should also be able to use graphene devices to *measure* magnetic fields. The maximum force resolution of this system can be found by setting its energy equal to the thermal energy: $E = \mu \cdot B_{min} = k_B T$. A $10 \mu\text{m} \times 10 \mu\text{m} \times 150 \text{nm}$ iron pad should have a magnetic moment of $\sim 2\mu_B(\rho V)/m_{iron\ atom} = 10^{-11} \text{ J/T}$,¹²⁶ so we have an approximate B_{min} of 10^{-10} T . For comparison, the Earth's field is of order 10^{-4} T , so this is a remarkably sensitive magnetic field sensor.

7.5 Superparamagnetic control of graphene devices

If we make pads out of a superparamagnetic material instead of iron, we should be able to perform more complex actuation, and build structures such as envelopes that we can open and close. Superparamagnetic microbeads made from

ferromagnetic nanoparticles embedded in latex are commonly used in magnetic tweezer applications.¹²⁷ Superparamagnetic materials have no net magnetization of their own, but when exposed to an external magnetic field they become magnetized and are attracted in the direction of highest field gradient.¹²⁸ They are made up of collections of ferromagnetic nanoparticles, which are small enough that they consist of a single magnetic domain that flips orientation under thermal fluctuations. The total collection of nanoparticles thus has a random orientation in zero field, and the superparamagnet has a net zero magnetic moment; but when exposed to an external field, these tiny magnets align and create a non-zero net magnetization (Fig. 7.6(a)). The practical result is that we can effectively turn the magnetic moment of the pads on and off by applying an external magnetic field.

Paramagnetic and superparamagnetic colloidal particles are known to aggregate into long chains in a magnetic field, and disperse again when the field is turned off.¹²⁷ A simple geometry based on this idea is shown in Fig. 7.6(b). When the field is off, two paramagnetic pads sit some distance apart, connected by graphene; and when we turn on the external magnetic field the two pads become magnetized and snap together. Turning off the field again, they return to their original orientation. The simple geometry shown in Fig. 7.6(b) provides a new kind of remote actuation, where we can create temporary attractive forces between different points on the graphene device. We can imagine using it to build and manipulate increasingly complex graphene devices, including envelopes and grippers that we can open and close by turning the magnetic field on and off (Fig. 7.6(c)).

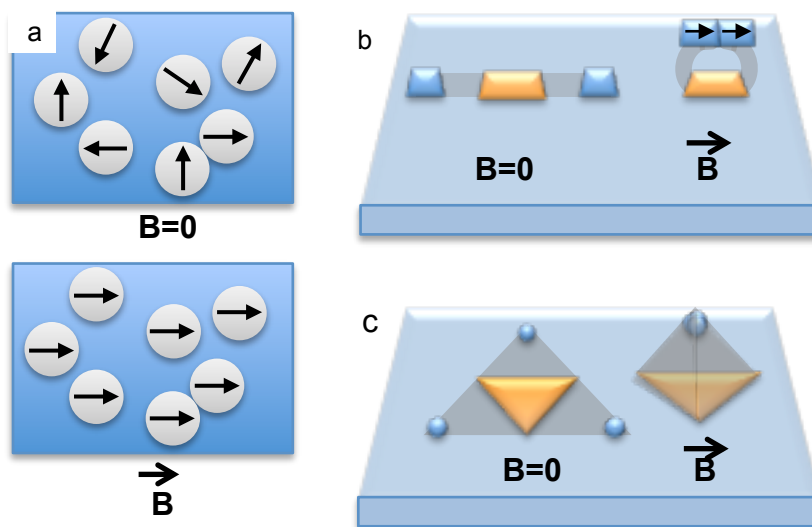


Fig. 7.6: Actuating graphene with superparamagnetic pads. (a) Superparamagnetic materials are made from a nonmagnetic matrix with imbedded ferromagnetic nanoparticles. At zero field the magnetic moments of these nanoparticles are randomly aligned, but when we apply an external magnetic field the magnetic moments align, giving the pad a net magnetization. (b) A simple pinned shape lies flat in zero magnetic field, but its two superparamagnetic pads (blue) become magnetized and snap together in an external magnetic field. (c) The same idea in three dimensions forms a temporary envelope structure that can be opened and closed.

7.6 Applications of graphene kirigami to optics

We have already demonstrated that we can actuate graphene kirigami devices using light. We showed laser-induced crumpling of large sheets of graphene in Chapter 3, and used photon pressure forces to actuate out-of-plane springs and cantilevers in Chapter 6. In this section we will discuss the possibility of going in the other direction: using graphene kirigami devices to control light.

Fig. 7.7(a) shows a building in Switzerland by the architecture firm Herzog & De Meuron.¹²⁹ The kirigami-style cuts in the aluminum façade are designed to let variable amounts of light into different parts of the building. Areas that are locally more stretched out let more light through, while relaxed areas are mostly opaque.

Graphene is mostly transparent, of course, so only 2.3% of light will be absorbed even when the spring is fully relaxed. However, we can imagine adding gold pads to part of each cantilever in the spring, as in Fig. 7.7(b). The spring constant of the device will be higher, since its component cantilevers are effectively shorter, but it should still be able to stretch. In that case, the most light will be blocked when the spring is relaxed, but as we stretch the spring, these pads pull apart and rotate out of plane, allowing significantly more of the light through. They could be used as robust, adjustable light filters at the microscale.

Also consider the light *reflected* from the gold pads. As the spring stretches and the links rotate, light will reflect off of the pads at a different angle (Fig. 7.7(c)). We could bounce a laser off of these pads to determine their angle to high precision, just as an AFM determines nanometer-scale deflections of its cantilever by tracking reflected laser light on an array of photodiodes. This technique should let us measure even smaller changes in the spring's extension than direct optical tracking can offer.

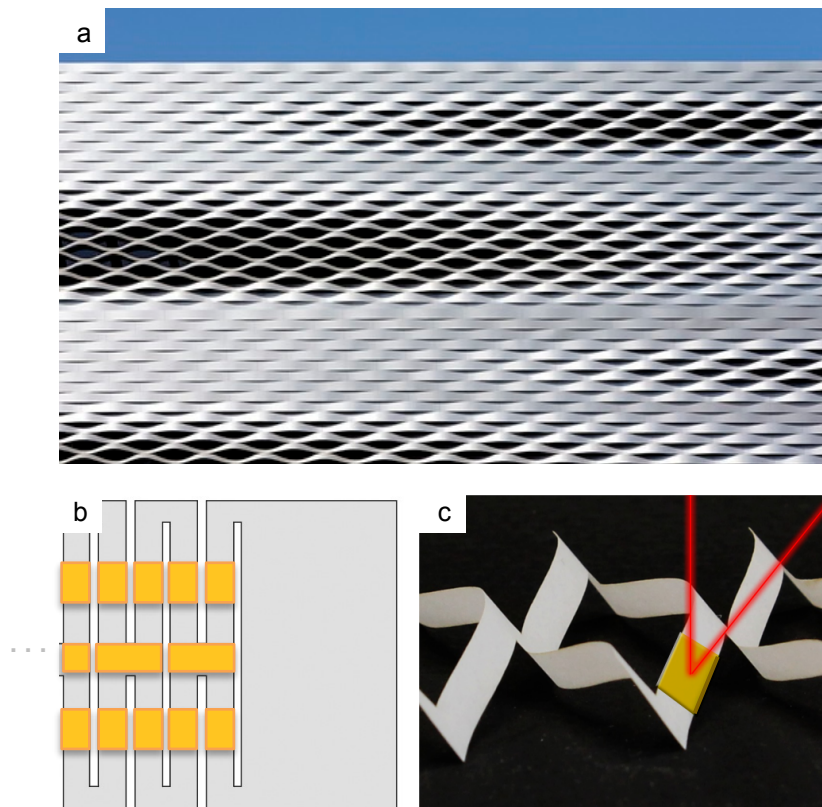


Fig. 7.7: Optics applications. (a) A building in Basel, Switzerland by Herzog & De Meuron. The kirigami pattern is cut out of aluminum, and locally stretched to allow more or less light into different areas of the building. Photo by Hufton+Crow. (b) Gold pads on the springs make the spring partially opaque. (c) Individual gold pads could also be used to reflect a laser, with the reflection angle giving sensitive information about how much the spring is stretched.

7.7 *Bimorphs and graphene origami*

This thesis has focused on graphene kirigami, where graphene does not need to hold a crease. However, we can also consider using some of these fabrication and manipulation techniques to move towards graphene *origami*.

As we have seen throughout this thesis, graphene can easily be deformed, but unless we somehow pin it in place it will return to its flat state. One simple way of creating permanent or semi-permanent folds in graphene is to add a second layer to the top of the membrane. We have already unintentionally created permanently folding devices—a failed fabrication led to a thick layer of polymer residue with built-in strain on top of the graphene. When we released these devices from the surface, they began to curl up (Fig. 7.8(a)).

A bimorph is a structure that consists of two layers of material that expand or contract at different rates in response to changes in temperature, ionic concentration, or other environmental cues (Fig. 7.8(b)). Graphene bimorphs have been created before by putting graphene on a thicker supporting material,^{130,131} and integrating this idea with the cantilevers in Chapter 5 should be straightforward.

We can imagine adding a layer of polymer to the top of the existing graphene cantilevers during the fabrication process, and actuating them by changing their environment. These devices could act as sensors, or we could use them as joints to create more complex three-dimensional devices that fold and unfold. These bimorph regions could be actuated collectively by changing the environment or individually by laser heating. They would add another type of actuation to our growing toolbox of nanoscale moving parts, and might someday lead to true graphene origami.

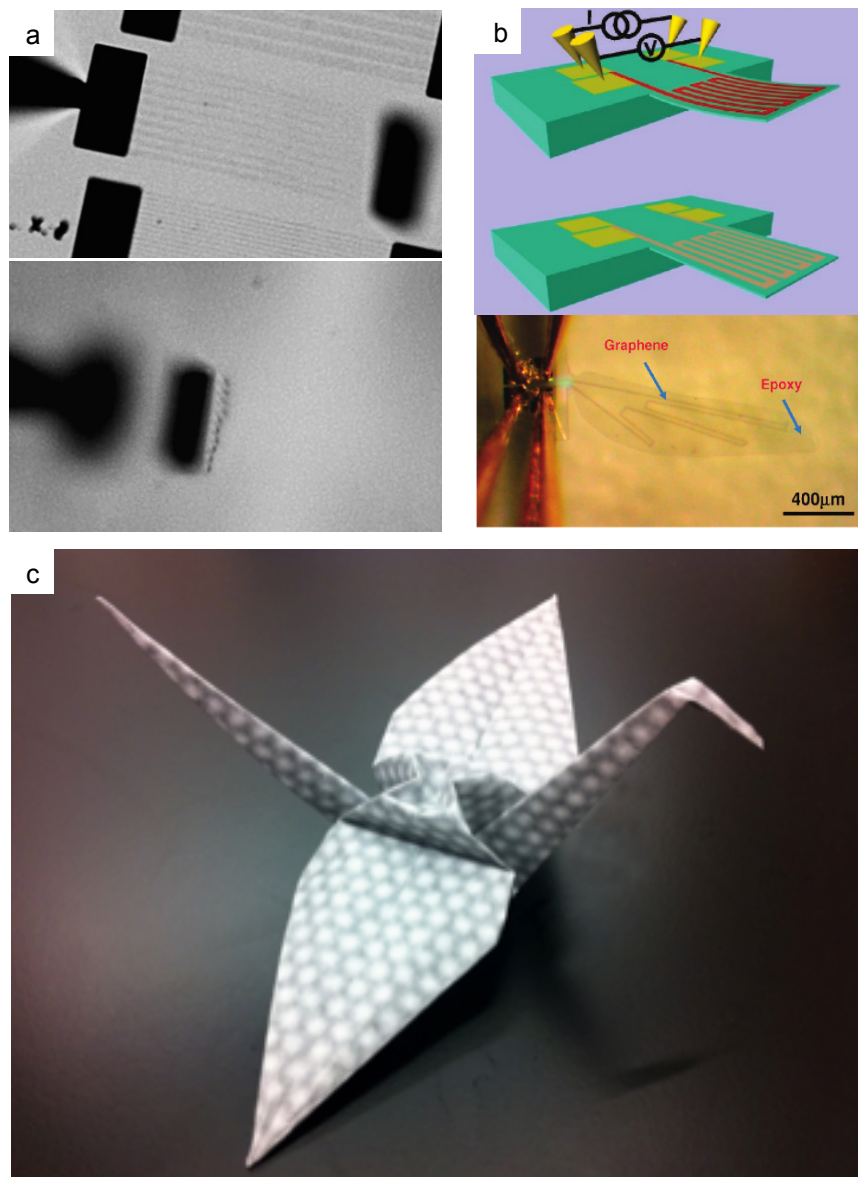


Fig. 7.8: Bimorphs and graphene origami. (a) Unintentional folding of graphene: a fabrication resulted in a thick layer of polymer with built-in strain on the surface of the graphene. When released from the surface, these devices curled up dramatically. (b) Example of bimorph actuated using heat from a resistive circuit. Graphene provides the conductive path. Figure from S-E. Zhu et al., *Nano Letters* (2011). (c) A long-term goal: true origami from graphene.

7.8 Conclusions

As we look at the possible future applications for graphene kirigami, we see two paths emerging: one where graphene is itself a nanoscale active element, and another where graphene kirigami serves as a robust, flexible, stretchable substrate for other elements. We believe that these techniques will prove to be widely applicable, and that many of the design and fabrication principles will directly translate to other two-dimensional materials.

Graphene kirigami opens a door to self-actuated 2D functional devices that respond to light or magnetic fields, changes in temperature, or even chemical signals. The future promises a diverse toolbox of atomic membrane devices for sensing, manipulation, complex origami, and even nanoscale robotics.

CHAPTER 8

ADDENDUM

After this thesis was written, we received referee comments on the related paper. The referees asked us to explain the offset between the average values of the gravity and thermal data in Chapter 5. They also asked us to address the issue of static structure in the graphene, which we had considered but had not found a way to measure at the time. In the months since, graduate students in the group have taken additional bending stiffness data and have found a way to measure the static shape of the graphene. In this addendum we will very briefly discuss these new results so that the reader is made aware of them; for details, we direct you to the paper.

Peter Rose and Kathryn McGill continued taking bending stiffness data, improving on the thermal data by using much longer video files and better eliminating the probe drift. They also used laser pressure to push on the cantilevers, as described in Chapter 6; this gives a third, independent means of measuring the spring constant of cantilevers. The resulting data is a good match to the thermal results, suggesting that the gravity technique was giving an artificially low value of the bending stiffness. They tried rotating a number of long cantilevers and found that the devices sometimes had a static deflection. In every case of offset it gave a downward deflection, perhaps due to crumpling induced during the lifting process. The gravity technique therefore gives an artificially *low* value of the spring constant, as the data from the other

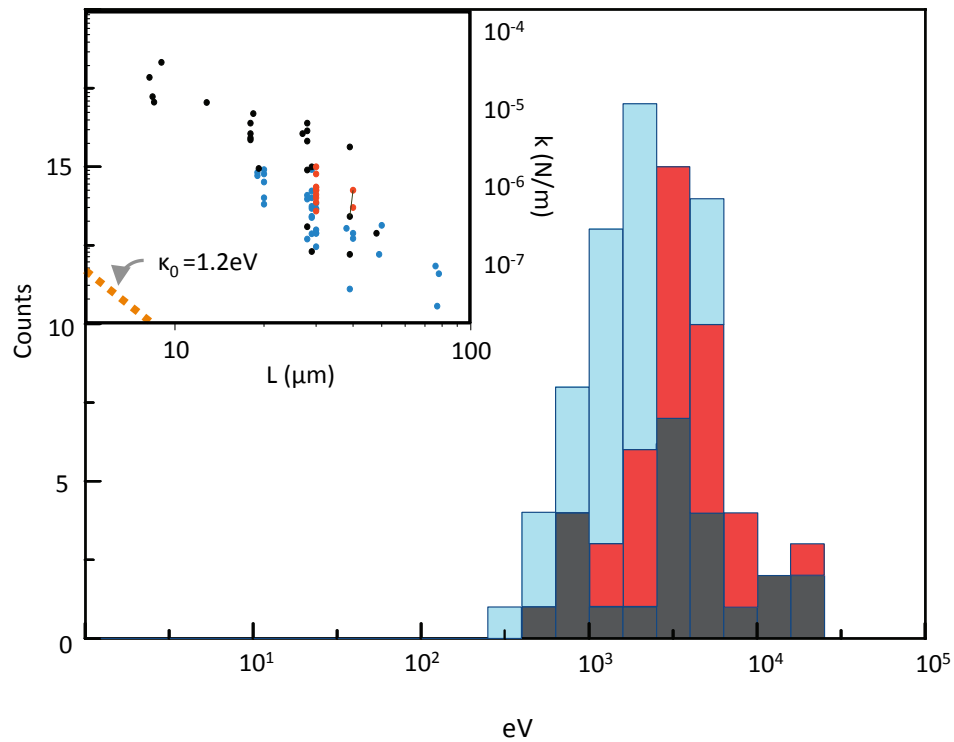


Fig. 8.1: Histogram of all data, including additional thermal measurements and laser force measurements. Note that the gravitational data is biased towards softer values, while the laser and thermal data agree on a somewhat higher value. Inset: Length-v.-spring-constants plot showing all data.

measurement techniques would suggest. The gravitational data is shifted down, though it is still within the spread of the data. A histogram showing data from all devices is given in Fig. 8.1, along with a length-dependence plot showing all of the data collected to date. These additional measurements finally explain the different values of the spring constants obtained by the two methods in Chapter 5, and they also provide a third, independent way of measuring the bending stiffness of graphene.

In order to address the question of static structure, Arthur Barnard added an interference microscopy technique¹³² using a mercury arc lamp and 10-nm-FWHM bandpass filter. He saw static ripples on the order of ~ 80 nm, as shown in Fig. 8.2. The bands represent constant elevation, as on a contour map, with the spacing between black and white bands corresponding to changes in z of $\lambda/4 = 80$ nm when corrected for the index of refraction of water. AFM does not show this structure when the graphene is adhered to the substrate, but after the etch it persists, even when the device is picked up off of the surface and settles down again. These ripples may be due to residue on the surface that causes local strains, or to grain boundaries. In any case, the amplitude is likely to be sample-specific.

This rough measure of the height of the static ripples allows us to compare to the theory of static structure for the first time. A recent paper¹³³ predicted the stiffening effect of static ripples of an effective squared amplitude $\langle z_{eff}^2 \rangle$ as:

$$\kappa_{eff} \sim \sqrt{Y_0 \kappa_0 \langle z_{eff}^2 \rangle}$$

which for 80-nm-high ripples gives 4 keV—also a good match to the experimentally measured stiffness.

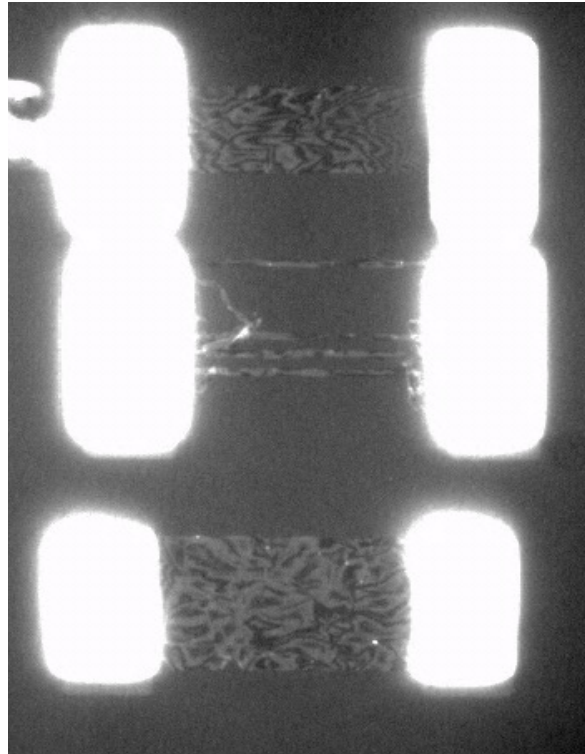


Fig. 8.2: Interference microscopy image of graphene cantilevers showing static structure. The light and dark bands can be roughly read as a contour map. The structure does not disappear when the devices are lifted off of the surface and settle down again.

The predicted stiffening effect of static structure is not width-dependent, so we should also consider how it will change the predictions for the simple model of the pyramid's spring constant in Chapter 6 (stiffening it to 6×10^{-6} N/m) and the Fopl-von-Karman number in Chapter 4 (lowering it to $\sim 10^5$), though the measurements are not precise enough to let us distinguish between the static and thermal theory. In fact, the similar predictions of the two theories underline the fact that the three-dimensional structure of the graphene membrane dominates its out-of-plane mechanical properties, regardless of whether that structure is thermally induced, static, or a combination of the two effects. Theorists have begun to make predictions about the combined effects of static and thermal ripples,¹³⁴ and further experimental work that allows us to tune the static structure or temperature of the devices should let us start to piece apart these two contributions.

REFERENCES

1. Feynman, R. There's Plenty of Room at the Bottom. *Caltech Engineering and Science* **23**, (1960).
2. McEuen, P. L. Small Machines. *Daedalus* **141**, 35–44 (2012).
3. Li, M., Tang, H. X. & Roukes, M. L. Ultra-sensitive NEMS-based cantilevers for sensing, scanned probe and very high-frequency applications. *Nat. Nanotechnol.* **2**, 114–120 (2007).
4. MEMS at Sandia National Lab. *Sandia MEMs Home Page* at <<http://mems.sandia.gov/>>
5. Kladitis, P. E., Linderman, R. J. & Bright, V. M. Solder self-assembled micro axial flow fan driven by a scratch drive actuator rotary motor. in *The 14th IEEE International Conference on Micro Electro Mechanical Systems, 2001. MEMS 2001* 598–601 (2001). doi:10.1109/MEMSYS.2001.906612
6. Kladitis, P. E. & Bright, V. M. Prototype microrobots for micro-positioning and micro-unmanned vehicles. *Sens. Actuators Phys.* **80**, 132–137 (2000).
7. Chronis, N. & Lee, L. P. Electrothermally Activated SU-8 Microgripper for Single Cell Manipulation in Solution. *J. Microelectromechanical Syst.* **14**, 857–863 (2005).
8. Tierno, P., Golestanian, R., Pagonabarraga, I. & Sagués, F. Magnetically Actuated Colloidal Microswimmers. *J. Phys. Chem. B* **112**, 16525–16528 (2008).
9. Gray, B. L. A Review of Magnetic Composite Polymers Applied to Microfluidic Devices. *J. Electrochem. Soc.* **161**, B3173–B3183 (2014).
10. Kuribayashi-Shigetomi, K., Onoe, H. & Takeuchi, S. Cell Origami: Self-Folding of Three-Dimensional Cell-Laden Microstructures Driven by Cell Traction Force. *PLoS ONE* **7**, e51085 (2012).
11. Caron, N. S., Desmond, C. R., Xia, J. & Truant, R. Polyglutamine domain flexibility mediates the proximity between flanking sequences in huntingtin. *Proc. Natl. Acad. Sci.* **110**, 14610–14615 (2013).
12. Vale, R. D. & Milligan, R. A. The Way Things Move: Looking Under the Hood of Molecular Motor Proteins. *Science* **288**, 88–95 (2000).
13. Bowman, G. R., Voelz, V. A. & Pande, V. S. Atomistic Folding Simulations of the Five-Helix Bundle Protein λ 6–85. *J. Am. Chem. Soc.* **133**, 664–667 (2011).
14. Haas, F. & Wootton, R. J. Two Basic Mechanisms in Insect Wing Folding. *Proc. R. Soc. Lond. B Biol. Sci.* **263**, 1651–1658 (1996).
15. Sareh, S. & Rossiter, J. Kirigami artificial muscles with complex biologically inspired morphologies. *Smart Mater. Struct.* **22**, 014004 (2013).
16. Wang-Iverson, P., Lang, R. J. & YIM, M. *Origami 5: Fifth International Meeting of Origami Science, Mathematics, and Education*. (CRC Press, 2011).
17. Rothmund, P. W. K. Folding DNA to create nanoscale shapes and patterns. *Nature* **440**, 297–302 (2006).
18. Han, D., Pal, S., Liu, Y. & Yan, H. Folding and cutting DNA into reconfigurable topological nanostructures. *Nat. Nanotechnol.* **5**, 712–717 (2010).
19. Douglas, S. M., Bachelet, I. & Church, G. M. A Logic-Gated Nanorobot for Targeted Transport of Molecular Payloads. *Science* **335**, 831–834 (2012).

20. Know How to Fold 'Em: How Origami Changed Science, From Heart Stents to Airbags. *LA Weekly* at <<http://www.laweekly.com/publicspectacle/2012/04/26/know-how-to-fold-em-how-origami-changed-science-from-heart-stents-to-airbags>>
21. Origami expert advises engineers how to build shrinking Nasa solar array (Wired UK). *Wired UK* at <<http://www.wired.co.uk/news/archive/2013-12/16/origami-solar-array>>
22. Novoselov, K. S. *et al.* Electric Field Effect in Atomically Thin Carbon Films. *Science* **306**, 666–669 (2004).
23. Li, X. *et al.* Large-Area Synthesis of High-Quality and Uniform Graphene Films on Copper Foils. *Science* **324**, 1312–1314 (2009).
24. Li, X. *et al.* Transfer of Large-Area Graphene Films for High-Performance Transparent Conductive Electrodes. *Nano Lett.* **9**, 4359–4363 (2009).
25. Wierman, J. L., Alden, J. S., Kim, C. U., McEuen, P. L. & Gruner, S. M. Graphene as a protein crystal mounting material to reduce background scatter. *J. Appl. Crystallogr.* **46**, 1501–1507 (2013).
26. Yuk, J. M. *et al.* Graphene Veils and Sandwiches. *Nano Lett.* **11**, 3290–3294 (2011).
27. Nair, R. R. *et al.* Fine Structure Constant Defines Visual Transparency of Graphene. *Science* **320**, 1308–1308 (2008).
28. Lee, C., Wei, X., Kysar, J. W. & Hone, J. Measurement of the Elastic Properties and Intrinsic Strength of Monolayer Graphene. *Science* **321**, 385–388 (2008).
29. Kim, K. S. *et al.* Large-scale pattern growth of graphene films for stretchable transparent electrodes. *Nature* **457**, 706–710 (2009).
30. Ruiz-Vargas, C. S. *et al.* Softened Elastic Response and Unzipping in Chemical Vapor Deposition Graphene Membranes. *Nano Lett.* **11**, 2259–2263 (2011).
31. Huang, Y., Wu, J. & Hwang, K. C. Thickness of graphene and single-wall carbon nanotubes. *Phys. Rev. B* **74**, 245413 (2006).
32. Wei, Y., Wang, B., Wu, J., Yang, R. & Dunn, M. L. Bending Rigidity and Gaussian Bending Stiffness of Single-Layered Graphene. *Nano Lett.* **13**, 26–30 (2013).
33. Nicklow, R., Wakabayashi, N. & Smith, H. G. Lattice Dynamics of Pyrolytic Graphite. *Phys. Rev. B* **5**, 4951–4962 (1972).
34. Blakslee, O. L. Elastic Constants of Compression-Annealed Pyrolytic Graphite. *J. Appl. Phys.* **41**, 3373 (1970).
35. Nelson, D. R. & Peliti, L. Fluctuations in membranes with crystalline and hexatic order. *J. Phys.* **48**, 1085–1092 (1987).
36. Gao, W. & Huang, R. Effect of surface roughness on adhesion of graphene membranes. *J. Phys. Appl. Phys.* **44**, 452001 (2011).
37. Klimov, N. N. *et al.* Electromechanical Properties of Graphene Drumheads. *Science* **336**, 1557–1561 (2012).
38. Bunch, J. S. *et al.* Electromechanical Resonators from Graphene Sheets. *Science* **315**, 490–493 (2007).
39. Zande, A. M. van der *et al.* Large-Scale Arrays of Single-Layer Graphene Resonators. *Nano Lett.* **10**, 4869–4873 (2010).

40. Bunch, J. S. *et al.* Impermeable Atomic Membranes from Graphene Sheets. *Nano Lett.* **8**, 2458–2462 (2008).
41. Huang, P. Y., Meyer, J. C. & Muller, D. A. From atoms to grains: Transmission electron microscopy of graphene. *MRS Bull.* **37**, 1214–1221 (2012).
42. Koenig, S. P., Boddeti, N. G., Dunn, M. L. & Bunch, J. S. Ultrastrong adhesion of graphene membranes. *Nat. Nanotechnol.* **6**, 543–546 (2011).
43. Wang, Y. *et al.* Super-Elastic Graphene Ripples for Flexible Strain Sensors. *ACS Nano* **5**, 3645–3650 (2011).
44. Bao, W. *et al.* Controlled ripple texturing of suspended graphene and ultrathin graphite membranes. *Nat. Nanotechnol.* **4**, 562–566 (2009).
45. Lindahl, N. *et al.* Determination of the Bending Rigidity of Graphene via Electrostatic Actuation of Buckled Membranes. *Nano Lett.* **12**, 3526–3531 (2012).
46. Booth, T. J. *et al.* Macroscopic Graphene Membranes and Their Extraordinary Stiffness. *Nano Lett.* **8**, 2442–2446 (2008).
47. Pu, N.-W. *et al.* Dispersion of graphene in aqueous solutions with different types of surfactants and the production of graphene films by spray or drop coating. *J. Taiwan Inst. Chem. Eng.* **43**, 140–146 (2012).
48. Zu, S.-Z. & Han, B.-H. Aqueous Dispersion of Graphene Sheets Stabilized by Pluronic Copolymers: Formation of Supramolecular Hydrogel. *J. Phys. Chem. C* **113**, 13651–13657 (2009).
49. Luo, J., Kim, J. & Huang, J. Material Processing of Chemically Modified Graphene: Some Challenges and Solutions. *Acc. Chem. Res.* **46**, 2225–2234 (2013).
50. Kim, K. *et al.* Multiply folded graphene. *Phys. Rev. B* **83**, 245433 (2011).
51. Qi, J. S., Huang, J. Y., Feng, J., Shi, D. N. & Li, J. The Possibility of Chemically Inert, Graphene-Based All-Carbon Electronic Devices with 0.8 eV Gap. *ACS Nano* **5**, 3475–3482 (2011).
52. Zhang, J. *et al.* Free Folding of Suspended Graphene Sheets by Random Mechanical Stimulation. *Phys. Rev. Lett.* **104**, 166805 (2010).
53. Liu, F., Song, S., Xue, D. & Zhang, H. Folded Structured Graphene Paper for High Performance Electrode Materials. *Adv. Mater.* **24**, 1089–1094 (2012).
54. Cheng, W., Campolongo, M. J., Tan, S. J. & Luo, D. Freestanding ultrathin nanomembranes via self-assembly. *Nano Today* **4**, 482–493 (2009).
55. Ebbesen, T. W. & Hiura, H. Graphene in 3-dimensions: Towards graphite origami. *Adv. Mater.* **7**, 582–586 (1995).
56. Patra, N., Wang, B. & Král, P. Nanodroplet Activated and Guided Folding of Graphene Nanostructures. *Nano Lett.* **9**, 3766–3771 (2009).
57. Zhu, S. & Li, T. Hydrogenation-Assisted Graphene Origami and Its Application in Programmable Molecular Mass Uptake, Storage, and Release. *ACS Nano* **8**, 2864–2872 (2014).
58. Feng, J. *et al.* Patterning of graphene. *Nanoscale* **4**, 4883–4899 (2012).
59. Zhu, S., Huang, Y. & Li, T. Extremely compliant and highly stretchable patterned graphene. *Appl. Phys. Lett.* **104**, 173103 (2014).

60. Liang, X. *et al.* Toward Clean and Crackless Transfer of Graphene. *ACS Nano* **5**, 9144–9153 (2011).
61. Bae, S. *et al.* Roll-to-roll production of 30-inch graphene films for transparent electrodes. *Nat. Nanotechnol.* **5**, 574–578 (2010).
62. Huang, P. Y. *et al.* Grains and grain boundaries in single-layer graphene atomic patchwork quilts. *Nature* **469**, 389–392 (2011).
63. Ferrari, A. C. *et al.* Raman Spectrum of Graphene and Graphene Layers. *Phys. Rev. Lett.* **97**, 187401 (2006).
64. Song, J. *et al.* A general method for transferring graphene onto soft surfaces. *Nat. Nanotechnol.* **8**, 356–362 (2013).
65. Nemes-Incze, P., Osváth, Z., Kamarás, K. & Biró, L. P. Anomalies in thickness measurements of graphene and few layer graphite crystals by tapping mode atomic force microscopy. *Carbon* **46**, 1435–1442 (2008).
66. Lin, Y.-C. *et al.* Graphene Annealing: How Clean Can It Be? *Nano Lett.* **12**, 414–419 (2012).
67. Suttipong, M., Tummala, N. R., Kitiyanan, B. & Striolo, A. Role of Surfactant Molecular Structure on Self-Assembly: Aqueous SDBS on Carbon Nanotubes. *J. Phys. Chem. C* **115**, 17286–17296 (2011).
68. Forster, B., Van De Ville, D., Berent, J., Sage, D. & Unser, M. Complex wavelets for extended depth-of-field: A new method for the fusion of multichannel microscopy images. *Microsc. Res. Tech.* **65**, 33–42 (2004).
69. Murphy, D. B. & Davidson, M. W. *Fundamentals of Light Microscopy and Electronic Imaging*. (John Wiley & Sons, 2012).
70. Qin, L.-C. *et al.* Materials science: The smallest carbon nanotube. *Nature* **408**, 50–50 (2000).
71. Landau, L. D. & Lifshitz, E. M. *Theory of Elasticity*. (Butterworth-Heinemann, 2008).
72. Zakharchenko, K. V., Katsnelson, M. I. & Fasolino, A. Finite Temperature Lattice Properties of Graphene beyond the Quasiharmonic Approximation. *Phys. Rev. Lett.* **102**, 046808 (2009).
73. Los, J. H., Katsnelson, M. I., Yazyev, O. V., Zakharchenko, K. V. & Fasolino, A. Scaling properties of flexible membranes from atomistic simulations: Application to graphene. *Phys. Rev. B* **80**, 121405 (2009).
74. Peliti, L. & Leibler, S. Effects of Thermal Fluctuations on Systems with Small Surface Tension. *Phys. Rev. Lett.* **54**, 1690–1693 (1985).
75. *Statistical mechanics of membranes and surfaces: Jerusalem Winter School for Theoretical Physics, Jerusalem, 28 Dec. 87-6 Jan. 88*. (World Scientific, 1989).
76. Von Kármán, T. Festigkeitsproblem im Maschinenbau. *Encyk Math Wiss* **IV**, (1910).
77. Föppl, A. *Vorlesungen über technische Mechanik*. (B. G. Teubner, 1905).
78. Schulgasser, K. The in-plane poisson ratio of paper. *Fibre Sci. Technol.* **19**, 297–309 (1983).
79. The Rock Physics Handbook Tools for Seismic Analysis of Porous Media | Solid earth geophysics | Cambridge University Press. at <<http://www.cambridge.org/us/academic/subjects/earth-and-environmental->

science/solid-earth-geophysics/rock-physics-handbook-tools-seismic-analysis-porous-media-2nd-edition>

80. Aronovitz, J. A. & Lubensky, T. C. Fluctuations of Solid Membranes. *Phys. Rev. Lett.* **60**, 2634–2637 (1988).
81. Le Doussal, P. & Radzihovsky, L. Self-consistent theory of polymerized membranes. *Phys. Rev. Lett.* **69**, 1209–1212 (1992).
82. Kownacki, J.-P. & Mouhanna, D. Crumpling transition and flat phase of polymerized phantom membranes. *Phys. Rev. E* **79**, 040101 (2009).
83. Braghin, F. L. & Hasselmann, N. Thermal fluctuations of free-standing graphene. *Phys. Rev. B* **82**, 035407 (2010).
84. Bowick, M. J., Catterall, S. M., Falcioni, M., Thorleifsson, G. & Anagnostopoulos, K. N. The Flat Phase of Crystalline Membranes. *J. Phys. I* **6**, 1321–1345 (1996).
85. Roldán, R., Fasolino, A., Zakharchenko, K. V. & Katsnelson, M. I. Suppression of anharmonicities in crystalline membranes by external strain. *Phys. Rev. B* **83**, 174104 (2011).
86. Nelson, D. R. Private communications.
87. Schmidt, C. F. *et al.* Existence of a flat phase in red cell membrane skeletons. *Science* **259**, 952–955 (1993).
88. Matsui, K. *et al.* Mechanical properties of few layer graphene cantilever. in *2014 IEEE 27th International Conference on Micro Electro Mechanical Systems (MEMS)* 1087–1090 (2014). doi:10.1109/MEMSYS.2014.6765834
89. Meyer, J. C. *et al.* The structure of suspended graphene sheets. *Nature* **446**, 60–63 (2007).
90. Galbraith, W. The optical measurement of depth. *Q. J. Microsc. Sci.* **3**, 285–288 (1955).
91. Hecht, E. *Optics (4th Edition)*. (Addison-Wesley, 2001).
92. Rice, A. & Fischer, R. Calibration of Optical Tweezers. at <<http://128.223.20.10/experiments/Optical-Tweezers/Calibration%20of%20Optical%20Tweezers.pdf>>
93. Velasco, S. On the Brownian motion of a harmonically bound particle and the theory of a Wiener process. *Eur. J. Phys.* **6**, 259–265 (1985).
94. De Groot, B. G. A simple model for Brownian motion leading to the Langevin equation. *Am. J. Phys.* **67**, 1248 (1999).
95. Deng, Y., Bechhoefer, J. & Forde, N. R. Brownian motion in a modulated optical trap. *J. Opt. Pure Appl. Opt.* **9**, S256 (2007).
96. Roberts, S. Carbon Nanotube NEMs—Towards biological applications. (Cornell University, 2014).
97. Roberts, S. P. *et al.* Single-Molecule Studies of Magnetically Tagged Single-Wall Carbon Nanotubes. *Prep.*
98. Rieger, B., Dietrich, H. r. c., Doel, L. R. V. D. & Vliet, L. J. V. Diffusion of microspheres in sealed and open microarrays. *Microsc. Res. Tech.* **65**, 218–225 (2004).
99. Jennings, B. R. & Parslow, K. Particle Size Measurement: The Equivalent Spherical Diameter. *Proc. R. Soc. Lond. Math. Phys. Sci.* **419**, 137–149 (1988).

100. Weisstein, E. W. Gaussian Function -- from Wolfram MathWorld. at <<http://mathworld.wolfram.com/GaussianFunction.html>>
101. Te Velthuis, A. J. W., Kerssemakers, J. W. J., Lipfert, J. & Dekker, N. H. Quantitative Guidelines for Force Calibration through Spectral Analysis of Magnetic Tweezers Data. *Biophys. J.* **99**, 1292–1302 (2010).
102. Gittes, F. & Schmidt, C. F. Thermal noise limitations on micromechanical experiments. *Eur. Biophys. J.* **27**, 75–81 (1998).
103. *Harris' shock and vibration handbook*. (McGraw-Hill, 2010). at <http://encompass.library.cornell.edu/cgi-bin/checkIP.cgi?access=gateway_standard%26url=http://accessengineeringlibrary.com/browse/harris-shock-and-vibration-handbook-sixth-edition>
104. Cleveland, J. P., Manne, S., Bocek, D. & Hansma, P. K. A nondestructive method for determining the spring constant of cantilevers for scanning force microscopy. *Rev. Sci. Instrum.* **64**, 403–405 (1993).
105. PMMA material properties. *MIT Material Property Database* at <<http://www.mit.edu/~6.777/matprops/pmma.htm>>
106. Kirigami for Kids: at <<http://www.origami-resource-center.com/kirigami-for-kids.html>>
107. tomviz for tomographic visualization of 3D materials at atomic resolution. at <<http://www.tomviz.org/>>
108. Qi, Z., Park, H. S. & Campbell, D. K. Highly Deformable Graphene Kirigami. *ArXiv14078113 Cond-Mat Physicsphysics* (2014). at <<http://arxiv.org/abs/1407.8113>>
109. Rogers, J. A., Someya, T. & Huang, Y. Materials and Mechanics for Stretchable Electronics. *Science* **327**, 1603–1607 (2010).
110. Lee, S.-K. *et al.* Stretchable Graphene Transistors with Printed Dielectrics and Gate Electrodes. *Nano Lett.* **11**, 4642–4646 (2011).
111. Kim, B. J. *et al.* High-Performance Flexible Graphene Field Effect Transistors with Ion Gel Gate Dielectrics. *Nano Lett.* **10**, 3464–3466 (2010).
112. Guo, C. F., Sun, T., Liu, Q., Suo, Z. & Ren, Z. Highly stretchable and transparent nanomesh electrodes made by grain boundary lithography. *Nat. Commun.* **5**, (2014).
113. Ohno, Y., Maehashi, K., Yamashiro, Y. & Matsumoto, K. Electrolyte-Gated Graphene Field-Effect Transistors for Detecting pH and Protein Adsorption. *Nano Lett.* **9**, 3318–3322 (2009).
114. Heller, I. *et al.* Influence of Electrolyte Composition on Liquid-Gated Carbon Nanotube and Graphene Transistors. *J. Am. Chem. Soc.* **132**, 17149–17156 (2010).
115. Chen, F., Qing, Q., Xia, J., Li, J. & Tao, N. Electrochemical Gate-Controlled Charge Transport in Graphene in Ionic Liquid and Aqueous Solution. *J. Am. Chem. Soc.* **131**, 9908–9909 (2009).
116. Oullette, L. L. Chemical and biological sensing with carbon nanotubes in solution. (Cornell University, 2008).

117. Zhan, Y., Liu, Z., Najmaei, S., Ajayan, P. M. & Lou, J. Large-Area Vapor-Phase Growth and Characterization of MoS₂ Atomic Layers on a SiO₂ Substrate. *Small* **8**, 966–971 (2012).
118. Song, L. *et al.* Large Scale Growth and Characterization of Atomic Hexagonal Boron Nitride Layers. *Nano Lett.* **10**, 3209–3215 (2010).
119. Huang, P. Y. *et al.* Direct Imaging of a Two-Dimensional Silica Glass on Graphene. *Nano Lett.* **12**, 1081–1086 (2012).
120. Lee, G.-H. *et al.* Flexible and Transparent MoS₂ Field-Effect Transistors on Hexagonal Boron Nitride-Graphene Heterostructures. *ACS Nano* **7**, 7931–7936 (2013).
121. Weisenhorn, A. L., Maivald, P., Butt, H.-J. & Hansma, P. K. Measuring adhesion, attraction, and repulsion between surfaces in liquids with an atomic-force microscope. *Phys. Rev. B* **45**, 11226–11232 (1992).
122. Gosse, C. & Croquette, V. Magnetic Tweezers: Micromanipulation and Force Measurement at the Molecular Level. *Biophys. J.* **82**, 3314–3329 (2002).
123. *Handbook of Single-Molecule Biophysics.* at <<http://www.alibris.com/search/books/isbn/9780387764962>>
124. Tanase, M., Biais, N. & Sheetz, M. in *Methods in Cell Biology* (ed. Yu-Li Wang and Dennis E. Discher) **Volume 83**, 473–493 (Academic Press, 2007).
125. Boncheva, M. *et al.* Magnetic self-assembly of three-dimensional surfaces from planar sheets. *Proc. Natl. Acad. Sci. U. S. A.* **102**, 3924–3929 (2005).
126. Billas, I. M. L., Becker, J. A., Châtelain, A. & de Heer, W. A. Magnetic moments of iron clusters with 25 to 700 atoms and their dependence on temperature. *Phys. Rev. Lett.* **71**, 4067–4070 (1993).
127. Joanne H. E. Promislow, Gast, A. P. & Fermigier, M. Aggregation kinetics of paramagnetic colloidal particles. *J. Chem. Phys.* **102**, 5492–5498 (1995).
128. Spaldin, N. A. *Magnetic materials: fundamentals and device applications.* (Cambridge University Press, 2003).
129. Messe Basel New Hall by Herzog & de Meuron. *Dezeen* at <<http://www.dezeen.com/2013/05/27/messe-basel-new-hall-by-herzog-de-meuron-new-photographs/>>
130. Conley, H., Lavrik, N. V., Prasai, D. & Bolotin, K. I. Graphene Bimetallic-like Cantilevers: Probing Graphene/Substrate Interactions. *Nano Lett.* **11**, 4748–4752 (2011).
131. Zhu, S.-E. *et al.* Graphene-Based Bimorph Microactuators. *Nano Lett.* **11**, 977–981 (2011).
132. Georgiou, T. *et al.* Graphene bubbles with controllable curvature. *Appl. Phys. Lett.* **99**, 093103 (2011).
133. Košmrlj, A. & Nelson, D. R. Mechanical properties of warped membranes. *Phys. Rev. E* **88**, 012136 (2013).
134. Košmrlj, A. & Nelson, D. R. Thermal excitations of warped membranes. *Phys. Rev. E* **89**, 022126 (2014).

